

1 **Redox-sensitive partitioning of vanadium and other heterovalent elements between apatite and**
2 **biotite in high silica magmas**

3 Peteris Rozenbaks and James M. Brenan

4 *Department of Earth and Environmental Sciences, Dalhousie University, Halifax, Canada*

5
6 **Abstract**

7 Apatite and biotite, ubiquitous minerals in a multitude of natural rocks, host a variety of
8 trace elements, including those whose valence state, and hence ionic radius and charge, can vary
9 over the oxygen fugacity (fO_2) of natural magmatic systems. In this study, we determine partition
10 coefficients (D values) between apatite (ap), biotite (bt), and glass (gl) in five suites of natural,
11 mostly silicic, metaluminous to peraluminous rocks of reduced to oxidized conditions (FMQ-2.8 to
12 +4.3; FMQ = fayalite-magnetite-quartz buffer). Elements considered include alkalis, alkaline earths,
13 rare earth elements, transition metals, metalloids, and high field strength elements, of which V, As,
14 Eu, Mo, Sn, and W are expected to be heterovalent over the fO_2 range considered.

15 Results reveal changes in partitioning of the heterovalent elements over the fO_2 range. With
16 increasing fO_2 from FMQ-2.8 to FMQ+2.8, values of $D^{bt/gl}$ for V decrease from ~580 to ~50 whereas
17 $D^{ap/gl}$ increases from ~0.6 to ~5. Arsenic becomes more compatible in apatite with $D^{ap/gl}$ increasing
18 from ~0.04 to ~1.6. Europium $D^{ap/gl}$ values increase from ~20 to ~90. Molybdenum $D^{bt/gl}$ decreases
19 from ~2 to ~0.1. Tin becomes more compatible with both minerals as fO_2 increases, with $D^{bt/gl}$
20 increasing from ~0.1 to ~1.0 and $D^{ap/gl}$ from ~0.05 to ~0.3. Although the uncertainty on $D^{ap/gl}$ for W
21 is too large to derive a meaningful fO_2 relation, values for $D^{bt/gl}$ decrease from ~0.13 to ~0.02 with
22 increasing fO_2 . As vanadium shows counter variation in individual mineral/glass partitioning, the
23 apatite/biotite partitioning ($D^{ap/bt}$) sympathetically increases from ~0.003 to ~0.5 with increase in
24 fO_2 .

25 In addition to shifts in the relative proportions of oxidized and reduced species with fO_2 , the
26 observed partitioning relations for heterovalent elements could be caused by differences in other
27 parameters that affect the activity of single species, species proportions, temperature, etc. These
28 confounding aspects are assessed by comparison of the homovalent element partitioning data,
29 which are relatively constant for the samples investigated, and with a suggestion that larger D-

30 values involving one suite (Mascota, Mexico) are likely due to the stabilization of higher valence V
31 species in a more alkaline melt composition. Results therefore indicate that the observed variation
32 in heterovalent element partitioning is predominantly the result of fO_2 control on element species
33 and corresponding ionic radius. With this interpretation, we present a preliminary vanadium
34 partitioning model that considers changes in the proportion of vanadium species with fO_2 and
35 estimated values $D^{ap/bt}$ for vanadium species. Model results are used to estimate the fO_2 of the
36 peraluminous South Mountain Batholith (Nova Scotia, Canada) and Palabora carbonatite (South
37 Africa) for which oxybarometry has not been straightforward. Estimated oxygen fugacities are
38 consistent with other redox indications, however, other factors, including melt and biotite
39 composition, need to be considered to enable general application of the model. The partitioning of
40 vanadium between apatite and ferromagnesian minerals has the potential of a novel oxybarometer,
41 applicable to a broad range of igneous rocks, including Fe-Ti poor plutonic systems.

42 Keywords: apatite, biotite, vanadium, partitioning, trace element

43

44 **1. Introduction**

45 Oxygen fugacity (fO_2) is one of the fundamental thermodynamic variables in geological
46 systems as it drives redox reactions and controls phase stability (Frost, 1991). This in turn impacts
47 such aspects as the mineral paragenesis, rock solidus, magma and ore genesis, composition of fluids
48 and the mass transfer between solar system reservoirs (Gaillard et al., 2015; Moretti & Neuville, 2021;
49 Mungall, 2002; Taylor & Green, 1988). For heterovalent elements, oxygen fugacity is also linked to the
50 identity and relative proportions of chemical species through redox reactions (Carmichael & Ghiorso,
51 1990). As each element species has a specific charge and radius, a unique partitioning behavior
52 between coexisting phases could result. Thus, with proper calibration, heterovalent element
53 partitioning can be used as a proxy for igneous fO_2 (Arató & Audétat, 2017c; Ballhaus et al., 1991;
54 Burnham et al., 2015; Mallmann & O'Neill, 2013; Smythe & Brenan, 2015).

55 Among the suite of trace elements in natural igneous systems, vanadium (V) is somewhat
56 unique as it can exist in four valence states - V^{2+} , V^{3+} , V^{4+} , V^{5+} (Sutton et al., 2005). At the most
57 common geological redox conditions of ± 2 log units relative to the fayalite-magnetite-quartz (FMQ)
58 redox buffer (Cottrell et al., 2021), most of the vanadium is speciated as V^{3+} and V^{4+} (Canil, 1999).

59 These two species are expected to have similar partitioning behavior to Fe^{3+} and Ti^{4+} due to the
60 same valence and similar ionic radii (IR): 0.064 nm^1 (V^{3+}), similar to 0.0645 nm (Fe^{3+}) and 0.058 nm
61 (V^{4+}), similar to 0.0605 nm (Ti^{4+}). Thus, V^{3+} is most compatible with Fe^{3+} -bearing phases
62 (clinopyroxene, magnetite) and V^{4+} preferentially enters the titaniferous oxide minerals (Arató &
63 Audétat, 2017b; Mallmann & O'Neill, 2009). Similarly, V^{2+} mimics Fe^{2+} due to the same charge and near-
64 identical radii (0.079 and 0.078 nm , respectively) resulting in high compatibility in ferromagnesian
65 minerals, although this V species is sparse in terrestrial magmas (Sutton et al., 2005). Pentavalent
66 vanadium, similar to other highly charged ions (Nb^{5+} , Ta^{5+}), is expected to accumulate in the melt
67 phase as its size and charge make it generally incompatible with igneous rock forming mineral
68 structures (summarized in Ballouard et al., 2020). This rich variety of V species and partitioning
69 behaviors has enabled several experimentally calibrated vanadium oxybarometers for mineral-melt
70 systems that link V partitioning to magmatic redox state (Arató & Audétat, 2017c; Holycross & Cottrell,
71 2020, 2022; Mallmann & O'Neill, 2013; Sossi et al., 2018).

72 The application of mineral-melt oxybarometers, however, is often precluded by poorly
73 constrained or absent melt composition estimates (e.g., in hypabyssal and plutonic systems).
74 Therefore, oxybarometers involving intermineral partitioning are of use in systems for which the
75 melt phase cannot be characterized. In moderately oxidized, iron-bearing igneous rocks, oxygen
76 barometry involving coexisting cubic and rhombohedral oxides has been widely employed (Ghiorso &
77 Evans, 2008; Ghiorso & Sack, 1991). Unfortunately, this method can be infeasible for many systems
78 (e.g. chemically evolved granites, carbonatites) which are too iron-poor or have otherwise formed
79 outside the stability field of coexisting oxides. Therefore, the development of oxybarometers
80 involving heterovalent element partitioning between other rock-forming minerals is desirable. As a
81 recent example, Holycross and Cottrell (2022) demonstrated systematic changes in
82 rutile/clinopyroxene and rutile/garnet partitioning of vanadium over a large $f\text{O}_2$ range, and
83 therefore the potential for oxybarometry in appropriate bulk compositions (i.e., eclogites). The
84 changes in intermineral partitioning documented by Holycross and Cottrell (2022) are due to the
85 unique behavior of rutile, and its preferential acceptance of the V^{5+} species, which is otherwise

¹ Unless otherwise specified, ionic radii (IR) are from Shannon (1976)

86 incompatible in ferromagnesian minerals. From the consideration of cation radius and charge of
87 vanadium species, as described below, we expect that apatite may behave in a similar way to rutile,
88 with a preference for pentavalent vanadium. Owing to its ubiquity in intermediate to felsic igneous
89 rocks, and its common coexistence with apatite (Clarke et al., 2021), we have focused in this case on
90 biotite to complete the intermineral partitioning pair.

91 Apatite, with the formula ${}^{\text{IX}}\text{Ca}_4{}^{\text{VII}}\text{Ca}_6(\text{IVPO}_4)_6(\text{F,OH,Cl})_2$, comprises a group of phosphate
92 minerals, with three available cation sites (IV-, VII- and IX-fold), and most igneous endmembers
93 distinguished by the occupant of the anion site (OH, Cl, F). In the VII- and IX-fold cation sites, Ca^{2+} is
94 commonly substituted by Sr^{2+} , Pb^{2+} , Na^+ , REE^{3+} , and other similarly-sized cations (Pan and Fleet,
95 2002), which are significantly larger (> 0.1 nm) than any of the vanadium species. However, V^{5+} may
96 be compatible in the apatite structure as the oxyanion $(\text{VO}_4)^{-3}$ substituted for $(\text{PO}_4)^{-3}$, as evidenced
97 by the complete solid solution series between $\text{Ca}_{10}(\text{PO}_4)_6\text{F}_2$ and $\text{Ca}_{10}(\text{VO}_4)_6\text{F}_2$ confirmed by Kreidler &
98 Hummel (1970). Biotite, with the general formula ${}^{\text{XII}}\text{K}^{\text{VI}}(\text{Mg}_{0.6-1.8}, \text{Fe}_{2.4-1.2})^{\text{IV}}(\text{AlSi}_3)\text{O}_{10}(\text{OH,F,Cl})_2$, is a
99 trioctahedral mica, represented by solid solution between the ferruginous annite and magnesian
100 phlogopite endmembers. In its octahedral site, common replacements include Al^{3+} (eastonite-
101 siderophyllite substitution), Fe^{3+} and Ti^{4+} (Dymek, 1983), suggesting that V^{2+} , V^{3+} , and V^{4+} could
102 likewise be compatible. As demonstrated by Gao et al. (2023), although the pentavalent cations
103 Nb^{5+} and Ta^{5+} exhibit some level of compatibility in biotite ($D(\text{Nb,Ta})^{\text{bt/gl}}$ of ~ 0.05 to 3), values of
104 $D(\text{Ti}^{4+})^{\text{bt/gl}}$ are at least 10x larger, therefore V^{5+} is expected to be the least compatible vanadium
105 species.

106 In terms of the anticipated change in apatite/biotite partitioning with $f\text{O}_2$, V^{5+} is expected to
107 have the highest D value for distribution between apatite and biotite, owing to its stability in the
108 apatite structure as the $(\text{VO}_4)^{3-}$ oxyanion. With decreasing charge and increasing ionic radius, other V
109 species are generally expected to become progressively less compatible in the apatite structure and
110 more compatible in biotite, thus resulting in decreasing D values. The bulk distribution of all V species,
111 $D(\Sigma\text{V})^{\text{ap/bt}}$ is therefore dependent on the igneous speciation of V, which is controlled by the magmatic
112 $f\text{O}_2$ (Sutton et al., 2005). As oxidizing conditions will increase the relative abundance of high-valence
113 V species, enhanced partitioning of V into apatite over biotite is expected, thus linking $D(\Sigma\text{V})^{\text{ap/bt}}$ to
114 the igneous $f\text{O}_2$ in a positive correlation. We test this hypothesis by measuring the partitioning of

115 vanadium and other trace elements, including those with several valence states, between apatite,
116 biotite, and glass in five natural igneous systems formed over a wide range of oxygen fugacity.

117 **3. Materials and methods**

118 **3.1 Sample suites**

119 Samples of five, previously well-described volcanic and plutonic rock suites were analyzed in
120 this study:

- 121 1) Revancha dyke and Cerro Esquinani stock from the Picotani intrusive suite, related to the
122 Macusani volcanics, southeastern Peru (Sandeman et al., 1997),
- 123 2) Tuk-Tuk dome, related to the Youngest Toba tuff member, Sumatra, Indonesia (Chesner
124 et al., 2020),
- 125 3) Fish Canyon tuff, Colorado, USA (Whitney & Stormer, 1985),
- 126 4) Mascota minette, Jalisco, Mexico (Carmichael et al., 1996), and
- 127 5) Umiakovik pluton of the Nain intrusive suite, Labrador, Canada (Emslie & Stirling, 1993).

128 The global distribution of the sample suites is shown in Figure 1, and relevant characteristics
129 are provided in Table 1. The suites were selected based on the criteria that they contain unaltered
130 biotite and apatite in a textural association suggesting phase equilibrium (i.e., planar contacts, lack
131 of reaction textures). Except for the samples from Umiakovik and Mascota, all others contain a
132 vitreous matrix, which enables determination of mineral-melt partitioning. Also considered is that
133 other intensive parameters, including crystallization temperature (T) and oxygen fugacity are
134 reasonably well known and span a sufficiently large range that meaningful relations between fO_2
135 and partitioning of redox-sensitive elements could be obtained. Independent estimates of fO_2 have
136 been published for all the suites except the Macusani subvolcanics, in which the fO_2 was determined
137 in this study using the Ce-in-zircon oxybarometer (Smythe & Brenan, 2016). Estimated oxygen
138 fugacities range from \sim FMQ-2.8 (Macusani subvolcanics) to FMQ+4.3 (Mascota minette) and
139 temperatures of 700-800°C (Table 1). Compositionally, samples range in whole-rock silica content
140 from 48.7 to 73.2, and are metaluminous to strongly peraluminous with A/CNK (molar ratio
141 $Al_2O_3/[CaO+Na_2O+K_2O]$) values of 0.5-1.2 (note that the glass analyses, reported below somewhat
142 differ from these whole-rock values due to the presence of phenocrysts).

143 Samples were received from several collections. A Fish Canyon tuff hand sample from the
144 classic sampling locality in a road cut on Colorado (USA) Highway 160 (Gleadow et al., 2015) was
145 provided by Dr. Ray Donelick (Apatite.com Partners LLC). Three samples of Macusani subvolcanics
146 were sourced from several collections – MAC137 (Revancha dyke) and MAC160 (Cerro Esquinani
147 stock) hand samples were received from Dr. John Hanchar (Memorial University of Newfoundland)
148 and MAC2 thin sections (Revancha dyke) from Dr. Hamish Sandeman (Geological Survey of
149 Newfoundland and Labrador). A Mascota minette sample was selected from the collection of the
150 Smithsonian Institution (catalog number NMNH 117626-21). Two samples of Tuk-Tuk tuff (TT and
151 TT7), related to the Younger Toba tuff, were provided by Dr. Craig Chesner (Eastern Illinois
152 University). Material from the Umiakovik Pluton were received as mineral separates from the
153 Geochronology Laboratory Archive of the Geological Survey of Canada (sample EC-87-119, database
154 number Z1280).

155 As-received rock hand samples were split into cm-sized fragments, and both rock fragments
156 and mineral separates were mounted in 1" epoxy pucks, which were then prepared by grinding with
157 progressively finer SiC grit, followed by 1 micron, then 0.3 micron alumina powder. Polished thin
158 sections of the Mascota minette were prepared in the Petrography Laboratory at Saint Mary's
159 University (Halifax, Canada). Sample billets for polished thin sections were lapped flat and mounted
160 to frosted glass slides using epoxy. Sections were cut and lapped to ~100 microns thick, then
161 polished using monocrystalline diamond suspensions down to 3 microns. Final polishing was
162 performed using 0.06 micron amorphous colloidal silica suspension.

163 **3.2. Analytical methods**

164 Reflected light image sample maps at a magnification of 2x were acquired by digital image
165 acquisition of the entire mounts. Areas of particular interest were then investigated by imaging at
166 higher magnifications. High spatial resolution textural observations and some semi-quantitative
167 chemical data on apatite, biotite and glass were obtained using a TESCAN MIRA 3 LMU Variable
168 Pressure Schottky Field Emission Scanning Electron Microscope (SEM) at Saint Mary's University
169 (Halifax, Canada). A beam voltage of 20 kV, beam current of 0.2 nA and an approximate working
170 distance of 17 mm were used for all EDS spot analyses and imaging. The reflected light and
171 backscattered electron images were used to identify mineral textures and morphology to select

172 areas for further chemical analysis. Individual mineral grains were selected based on lack of zoning
173 or an outer uniform zone being at least 25 μm thick. Similarly, for matrix glass analysis, areas larger
174 than 25 μm and devoid of microcrysts were selected.

175 The major element composition of the mineral and glass phases was determined using the
176 JEOL JXA-8230 Electron Probe Micro-Analyzer (EPMA) at the University of Toronto. Analytes and the
177 phase-specific routine analytical conditions are summarized in Table 2. The spectral interference
178 from the Fe $\text{L}\alpha_{1,2}$ emission line (705 eV) on the F $\text{K}\alpha$ line (676.8 eV) was determined by measuring
179 the F $\text{K}\alpha$ intensity in Fe-metal, which was then used to calculate an appropriate correction factor.
180 Analysis of Fe metal yielded F concentrations below detection limit (≤ 0.02 wt%), confirming the
181 efficacy of this correction method. Analytical accuracy was checked by analysis of fused beads of
182 basalt reference materials BIR-1, BHVO-1 and a fragment of rhyolite glass CAM66. For BIR-1 and
183 BHVO-1 the relative difference between the reported and measured values did not exceed 5% for
184 oxides of >1 wt.% abundance. For CAM66, the relative difference was $<1\%$ for SiO_2 , Al_2O_3 , K_2O
185 (above 4 wt.%) and $<15\%$ for FeO, CaO, Na_2O (above 1 wt.%). Although not certified standards, we
186 also analyzed fragments of San Carlos biotite (Righter and Carmichael, 1996) and Durango apatite as
187 checks on accuracy and reproducibility between analytical sessions. For San Carlos biotite, the
188 relative difference between the reported (Righter & Carmichael, 1996) and measured values was
189 $<3.6\%$ for oxides above 0.2 wt.%. For Durango apatite, the relative difference between the reported
190 (Young et al., 1969) and measured values was $<0.05\%$ for CaO and P_2O_5 , 5.2% for F, $<3.5\%$ for SiO_2
191 and Cl. Detailed precision and accuracy estimates are summarized in the Table ST1.

192 Trace element concentrations of apatite, biotite, and glass were determined using the laser
193 ablation ICP-MS facility located in the Health and Environments Research Centre (HERC) Laboratory
194 at Dalhousie University. The system employs a frequency quintupled Nd:YAG laser operating at 213
195 nm, coupled to a Thermo Scientific iCAP Q quadrupole mass spectrometer with He flushing the
196 ablation cell to enhance sensitivity (Eggins et al., 1998). Zircon from the Macusani suite of samples
197 was analyzed at the Micro-Analysis of Natural Trace-element and Isotope Systematics (MANTIS)
198 laboratory at University of New Brunswick. The system employs an ArF laser operating at 193 nm,
199 coupled to Agilent 7700x quadrupole mass-spectrometer using a mixture of He, Ar, and N as the
200 carrier gas as described by McFarlane & Luo (2012). The details of all the trace element analyses are

201 provided in Table 2. Each analytical session involved initial tuning using the NIST 610 glass reference
202 material, using ^{115}In to maximize sensitivity, $^{248}\text{ThO}/^{232}\text{Th}$ of <0.005 to minimize oxide production
203 and $^{238}\text{U}/^{232}\text{Th}$ of ~ 1 to monitor mass fractionation. Where possible, the analyses were carried out
204 in traverse track configuration to improve the signal stability. Factory supplied time resolved
205 software was utilized for the acquisition of individual analyses. A typical analysis involved 20
206 seconds of background acquisition with the ablation cell being flushed with the carrier gas, followed
207 by laser ablation for 60 seconds, then 40-60 seconds of cell washout. Analyses were collected in a
208 sequence in which two analyses were done on the NIST 610 standard reference material at the start
209 of the acquisition cycle, then after every 20 analyses on the unknowns including secondary
210 standards.

211 All LA-ICP-MS data reduction was done off-line using the Lolite version 4.0 software package
212 (Paton et al., 2011). Time-resolved signals were individually examined based on the major elements
213 in each phase and marker elements of potential contaminants – Na and K for glass and alkali
214 feldspars, Ca for apatite, hornblende, and plagioclase, Ti for ilmenite, Zr for zircon, REE for monazite.
215 Narrow spikes and otherwise anomalous spectra of the potential contaminant elements were used
216 as indicators of signal impurity from inclusions or adjacent phases. Spikes near the margins of
217 spectra were excluded by narrowing the signal selection, whereas the spectra containing multiple
218 spikes were discarded. Spectra with abnormal features were also discarded if the extracted
219 compositions deviated by >2 standard deviations from the mean content of the markers of the
220 potential contamination. Ablation yields were corrected by referencing to the EPMA-measured
221 concentration of internal standards (Table 2). As vanadium is an element of especial interest in this
222 study, care was made to consider and resolve any significant analytical interferences with isobaric
223 species that could affect analytical accuracy. Specific to halogen-bearing minerals like apatite and
224 biotite is the possible interference of the $^{35}\text{Cl}\text{-}^{16}\text{O}$ molecule on ^{51}V . The magnitude of this
225 interference was assessed by analyzing a synthetic endmember Cl-apatite (containing 6.81 wt% Cl;
226 provided by John Hanchar, Memorial University), which was assumed to be vanadium-free. The
227 calculated vanadium concentration of this material, considered to be wholly from the $^{35}\text{Cl}\text{-}^{16}\text{O}$
228 interference, is $\sim 1.3 \mu\text{g/g}$, resulting in a contribution of $\sim 0.2 \mu\text{g/g/wt\% Cl}$. The highest Cl
229 concentrations in measured phases are 0.84 wt% in apatite (FCT), 0.24 wt% in biotite (TT7) and 0.12

230 wt% in glass (FCT), resulting in maximum interference contributions of 0.16, 0.05 and 0.02 $\mu\text{g/g}$ in
231 apatite, biotite and glass, respectively. Reported vanadium concentrations reflect this minor
232 correction.

233 Comparison between the measured and reported values for secondary standards yields
234 average relative differences of $\sim 7\%$ for BIR-1 and BHVO-1 (Jochum et al., 2005) and $\sim 14\%$ for
235 Durango apatite (Marks et al., 2012). Measurements of our Durango apatite fragment were cross-
236 verified against the specimen at the MANTIS lab, with the median relative differences being $\sim 4.6\%$.
237 Summaries of the major and trace element concentrations of the analyzed phases are provided in
238 the Supplementary Tables ST1-6.

239 **4. Results**

240 **4.1 Phase assemblage and textures**

241 *Fish Canyon tuff* is sampled at its relatively lithic-rich, lower part of the thick proximal
242 vitrophyre ignimbrite. The sample consists of plagioclase, sanidine, biotite, hornblende, quartz,
243 magnetite, titanite, and ilmenite phenocrysts in a matrix of microcrysts, phenocryst fragments, and
244 glass. The relative proportions within the phenocryst assemblage in the sample are close to the ones
245 reported by Whitney and Stormer (1985) - $\sim 55\%$ plagioclase, $\sim 15\%$ alkali feldspar, 10% biotite, 10%
246 hornblende, 5% quartz, 5% trace minerals. Matrix is predominantly composed of glass shards,
247 crystal and pumice fragments, devitrified glass with several pockets of massive, fresh glass. Biotite is
248 typically fresh, euhedral, often kinked, and compositionally uniform (Figure 2a), often contains
249 inclusions of apatite, Fe-Ti oxides, and zircon. Apatite is present as up to $300\ \mu\text{m}$ long, euhedral,
250 equant to tabular phenocrysts and biotite-hosted inclusions. Texturally, apatite crystals are uniform,
251 featuring few inclusions of zircon and Fe-Ti oxides.

252 *Macusani subvolcanics* comprise samples from the Revancha dyke and the Cerro Esquinani
253 stock, which consist of plagioclase, sanidine, biotite phenocrysts with trace amounts of monazite,
254 apatite, ilmenite, and zircon set in a massive, uniform holohyaline matrix without any macroscopic
255 evidence of weathering or hydrothermal alteration. The Revancha dike exhibits a glass-rich (up to 74
256 vol%) margin (represented by MAC2) and a crystal-rich (up to $50\ \text{vol}\%$) porphyritic interior,
257 separated by a flow-banded facies with an intermediate glass content (represented by MAC137;

258 Sandeman & Clark, 2003). MAC137 (Figure 2b) is rich in biotite phenocrysts and microphenocrysts,
259 typically reverse-zoned, particularly the older, larger phenocrysts, which commonly exhibit
260 resorption features. Iron numbers (molar Fe/[Fe+Mg]; Fe#) of the analyses bt02 (rim) and bt03
261 (interior, Figure 2b) are 0.48 and 0.51 respectively. The smaller biotite microphenocrysts, however,
262 are euhedral and lack zoning. Apatite is euhedral to subhedral, commonly equant, texturally uniform
263 without obvious zoning. Apatite crystals are present as microphenocrysts and biotite-hosted
264 inclusions. Apatite phenocrysts, up to hundreds of microns in size, host ubiquitous melt, zircon,
265 ilmenite, and monazite inclusions (Figure 2 c,d), few crystals feature inherited cores (Fig. 2e).
266 Mineral textures in the more crystal-poor MAC2 (Figure 2c) are generally the same as in MAC137.
267 Glass in both samples is unaltered, but rich in microlites with a few clear areas, typically surrounded
268 by perlitic cracks. In the Cerro Esquinani stock sample (MAC160), biotite is unzoned, with some
269 occurrences of partial resorption. Both apatite and zircon are present, but less abundant in Cerro
270 Esquinani than in the Revancha dyke. Zircon is rare, occurring as small (<30 μm), euhedral
271 microphenocrysts and as inclusions in other minerals (Supplementary Figure S1). Typical of igneous
272 zircons, the zircon grains exhibit concentric growth and sector zoning; inherited cores
273 (Supplementary Figure S1a) are comparatively uncommon.

274 *Tuk-Tuk tuff* samples are light gray-to-white, vesicular (6-7 vol%; Figure 3e), comprised of
275 glass (47-72 vol%), quartz (6-12 vol%), sanidine (1-12 vol%), plagioclase (9-34 vol%), biotite (1-4
276 vol%), and hornblende (≤ 2 vol%) with trace amounts of zircon, allanite, magnetite, ilmenite,
277 orthopyroxene, and apatite (Chesner et al., 2020). Biotite in both samples is euhedral and kinked
278 crystals are common. Biotite does not exhibit observable compositional zoning and resorption
279 features in biotite are rare. Biotite-hosted inclusions of zircon, monazite, magnetite, and feldspar
280 are common in both samples, and melt inclusions are rare. Biotite in TT7 contains ubiquitous
281 inclusions of columnar apatite crystals, which are more common than the free apatite phenocrysts.
282 Apatite crystals are typically <100 μm long, euhedral, compositionally uniform, and lack mineral or
283 melt inclusions. Sample TT, however, is completely devoid of apatite.

284 *The Mascota augite minette* sample consists of augite (~13 vol%), biotite (~10 vol%), and
285 apatite (~3 vol%) phenocrysts and microphenocrysts in a very fine-grained matrix of augite, biotite
286 and Fe-Ti oxides. Biotite is predominantly euhedral with the largest phenocrysts (>1000 μm)

287 exhibiting sieve textures, resorption features, and normal zoning. Smaller biotite crystals (<100 µm)
288 are uniform and euhedral. Compared to the other analysed biotite populations, Mascota biotite
289 contains much fewer inclusions of apatite and other minerals. Apatite is represented by euhedral,
290 columnar to tabular, up to 500 µm long crystals lacking any observable zoning and inclusions.
291 Apatite crystals in contact with biotite are usually not entirely surrounded by biotite.

292 *The Umiakovik biotite-hornblende granite* sample consists of alkali feldspar (43 vol.%), quartz
293 (25 vol.%), plagioclase (20 vol.%), biotite (7 vol.%), hornblende (5 vol.%) and trace amounts of
294 apatite, zircon, ilmenite, and fluorite (Emslie & Loveridge, 1992). Biotite is dark brown, often bent,
295 subhedral, up to 1-2 mm large crystals without noticeable zoning in reflected light or SEM. Biotite
296 occasionally contains up to 20 microns sized apatite and zircon inclusions. Apatite crystals are
297 typically up to 400 microns in size, are euhedral with a prismatic habit, and pale green to
298 transparent in color. Backscatter electron imaging reveals that approximately 30% of apatite
299 crystals exhibit a distinct darker, rounded core with >20 micron thick, bright rim. Inclusions in
300 apatite are rare, usually comprising micron-sized zircons.

301 **4.2. Major element compositions of the glasses**

302 The analysed suite of matrix glasses represents silica-rich (71-75 wt% SiO₂), moderately to
303 strongly peraluminous (A/CNK=1.0-1.4), K- (4.9-5.7 wt% K₂O) and Na-rich (2.4-3.0 wt% Na₂O),
304 rhyolitic melt compositions, poor in MgO, FeO, CaO, and TiO₂. The electron microprobe data totals
305 are typically 95-97 wt%, which suggests the presence of dissolved H₂O. Among other volatiles, F and
306 SO₃ were below detection limits (0.2 and 0.1 wt% respectively), whereas Cl contents vary between
307 0.03 wt% (Macusani subvolcanics) and 0.12 wt% (FCT) with intermediate values of 0.08-0.09 wt% in
308 the Tuk-Tuk samples. Within the rather uniformly rhyolitic sample suite, Macusani subvolcanics
309 stand out as the most peraluminous and least alkaline (Figure 3), thus overlapping with the
310 genetically related effusive Picotani and Quenamari samples reported by Pichavant et al. (2024).
311 Glass from the Fish Canyon tuff represents the most potassic and silicic compositions, and the Tuk-
312 Tuk tuffs are the most sodic and calcic in the sample group (Figure 3).

313 **4.3. Major element composition of mineral phases**

314 *Biotite* compositional diversity is reflected by their values of Fe# (iron number;
315 $(\text{Fe}^{2+}/\text{Fe}^{2+}/\text{Mg})$; molar basis), which describes the solid solution between phlogopite and annite
316 (Figure 4). Iron number varies more between, than within most groups, thus resulting in discrete
317 Fe# ranges for MM (0.15-0.21), FCT (0.38-0.42) , TT and TT7 (0.57 – 0.61), MAC160 (0.45-0.52), and
318 UP (0.83-0.90). The Revancha biotite Fe# range is broader (0.24-0.53), which corresponds to a
319 relatively higher variability in all other major element abundances, some of which (positive - Al, Mn,
320 Cl, negative - Na) exhibit a covariation with Fe#, whereas others (Ti, F) do not. For Revancha biotites,
321 which are the most Mg-rich ($\text{Fe}\# > 0.42$), the Ti content is highly variable (0.2 – 0.7 a.p.f.u.), whereas
322 the more Fe-rich biotites show less variation in Ti (0.34 - 0.42).

323 Across the analyzed rock suites, other major element abundances in biotite overlap, leaving
324 only few signature outliers. The strongly peraluminous composition of the Macusani subvolcanics is
325 reflected in biotite with a slightly increased abundance of total Al and tetrahedral Al, the latter
326 corresponding to a decreased silica content due to the common Al-Si substitution in the tetrahedral
327 site. Based on the MnO content, the biotite suites can be divided into low-Mn biotite (MAC and
328 MM) and high-Mn (FCT, TT, UP) biotite (Figure 4c). The Umiakovik biotite, which is annite-rich and
329 generally variable in its major element content, is particularly low in Na, just exceeding the
330 detection limit of 0.02 wt% (Fig. 4d).

331 The major element content of apatite is generally uniform across the suites – Ca contents
332 typically exceed 9.5 a.p.f.u., which almost entirely fills the 7-fold and 9-fold coordination sites.
333 Tetrahedral sites are primarily filled with P (5.6-5.8 a.p.f.u.) with a minor Si component (0.1-0.2
334 a.p.f.u.). The anion site is dominated by F (1-2 a.p.f.u.), leaving < 1 a.p.f.u. of OH^- , and trace amounts
335 of Cl in a negative correlation with Fe in apatite (Figure 5). Mascota apatite has an exceptionally high
336 Si content (~ 0.2 a.p.f.u.) compared to apatite from other suites (~ 0.1 a.p.f.u.).

337 **4.4. Trace element compositions**

338 The trace element content of the analyzed glasses are normalized to the average upper crust
339 (Rudnick & Gao, 2003) in Figure 6, where elements are grouped according to their chemical
340 classification as alkalis (Li, Rb, Cs), alkaline earth (Sr, Ba), transition metal (Sc, V, Mn, Co, Ni, Cu, Zn,

341 Mo), metalloid (Ga, Ge, Cd, In, Sn, Pb, Bi), rare earth elements (La, Ce, Pr, Nd, Sm, Eu, Gd, Tb, Dy, Ho,
342 Er, Tm, Yb, Lu), and high field strength elements (Zr, Nb, Hf, Ta, W). Within each group the elements
343 are ordered according to mass number. Relative to crustal abundances, the analyzed glasses are
344 enriched in most alkalis, high field-strength elements and post-transition metals, but depleted in
345 alkaline earth elements (except Ba) and transition metals. In their rare-earth element compositions,
346 the matrix glasses are relatively depleted in intermediate REE (FCT and TT) or heavy REE (MAC) with
347 a distinct negative Eu anomaly in MAC and TT. Macusani glasses are generally the most enriched in
348 incompatible elements (with anomalously high Li, Cs, As, In, Sn concentrations in all Macusani
349 glasses, Bi, Pb, Rb, Sb, U, W in Revancha glasses, and Zn in Cerro Esquinani glasses). The abundance
350 of heterovalent elements in matrix glasses often strongly vary across the sample suite. Vanadium is
351 relatively depleted in all glasses with the normalized abundance varying between ~0.04 in Fish
352 Canyon tuff to ~0.008 in Revancha glasses. Molybdenum is generally enriched (up to ~5x the upper
353 crustal abundance in Fish Canyon tuff), however, in Cerro Esquinani glass it is slightly depleted.
354 Arsenic, indium, and tin are all most enriched (4-20x) in the Revancha dyke, and are slightly
355 depleted (0.9-0.5x) in Fish Canyon tuff. Tungsten and uranium are also the most enriched in
356 Revancha glasses (~7 x) and least enriched (1-2x) in Tuk-Tuk glasses.

357 The trace element abundances of biotite were found to correlate with their major element
358 composition. Within the low-Al biotite group (all but MAC biotites), most of the trace elements
359 correlate with the Fe#: Cs, Ge, Pb, Rb, Sc, Sn, Ta, V are in a positive correlation whereas Ba, Co, Cu,
360 Eu, Hf, Ni, Sr, and Zr correlate negatively with Fe# (Supplementary Figure S5). The aluminous biotites
361 of the evolved Macusani suite are enriched in trivalent (In, REE, Sc, As), pentavalent (P, Nb, Ta),
362 other incompatible elements (Rb, Pb, Ge, Bi) and vanadium relative to the less aluminous biotites.

363 *Apatite* strontium content correlates with the bulk rock silica content in a trend (in order of
364 increasing Sr) of UP-MAC137-MAC2-TT7-MAC160-FCT-MM. Within this series, Ba, V, Zn, Zr increase
365 and REE+Y decrease with increasing Sr. MAC and MM apatite populations record the broadest Sr
366 ranges (554-179 $\mu\text{g/g}$ and 7875-5365 $\mu\text{g/g}$, respectively) and reveal compositional trends: in MM,
367 Ba, REE, Mn, Ta, Th, Ti, V are in a positive correlation with Sr, whereas in MAC, Ba, LREE, Th, V, Zr are
368 in positive correlation and HREE, Mn are negatively correlated with Sr. Apatite from the Umiakovik
369 pluton show the largest variability in compatible trace elements (REE, Y, U, Th) without any

370 correlation to Sr. Instead, the silica content is in a positive correlation with trivalent (Ga, As, REE+Y),
371 tetravalent (Ge, Zr, Hf, Th), and other highly charged ions (Ta, W, U) and Rb, without correlation to
372 Mn, Fe, and Sr. The magnitude of the Eu anomaly (Eu/Eu^*_{CN} , where $Eu^*=(Sm \times Gd)^{0.5}$ and all element
373 concentrations are normalized to McDonough & Sun (1995) chondritic abundances) in UP apatites
374 strongly correlates with the Si content. The variation of trace elements in Macusani apatites is
375 similar to that of other apatites.

376 **4.5. Apatite and biotite chemistry as tracers of evolution of Macusani subvolcanics**

377 The measured biotite and apatite compositions in the Ravencha dyke samples (MAC2,
378 MAC137) from the Macusani subvolcanics show a high degree of variability in their major (Fig. 4a-d)
379 and trace element abundances (Supplementary Figure S4-5), which often do not follow the
380 expectations for a continuous liquid line of descent (e.g. Fe# and Al^{IV} in biotite, total REE content in
381 apatite, F/Cl in either mineral). This compositional heterogeneity has been attributed to a thermal
382 pulse and volatile (H₂O, Cl, F) influx due to mafic magma underplating (Sandeman & Clark, 2004). To
383 extract empirical partition coefficients that represent equilibrium mineral and glass compositions
384 therefore requires identification of co-crystallizing phase assemblages. Based on biotite Fe#, F/Cl,
385 Na, and Rb/K (Fig. 4d-g), two distinct biotite generations can be distinguished in these samples: 1)
386 more primitive, magnesian (Fe# <0.41), F-rich (F/Cl >30), and Rb-poor (Rb/K <0.008) and 2) more
387 evolved, ferrous (Fe# >0.46), Cl-rich (F/Cl <15), and Rb-rich (Rb/K >0.010). Here we consider the
388 more evolved second generation biotite as in equilibrium with the surrounding glass, which is
389 supported by biotite-glass Fe-Mg exchange and interelement partitioning systematics consistent
390 with previous experimental studies (see below). In contrast to the Ravencha dyke, sample MAC160
391 from the Cerro Esquinani stock yielded biotite with a more narrow compositional range, which is
392 overall similar to the more evolved Ravencha dyke group, but the latter with lower Rb/K values.
393 Biotite in MAC160 is compositionally uniform and considered to have formed in a single
394 crystallization event.

395 In Macusani samples, two apatite generations can be distinguished based on Sr and
396 chondrite-normalized La/Sm, $(La/Sm)_{CN}$: one with low Sr (170-400 $\mu\text{g/g}$) and low La/Sm (0.6-1.2) and
397 the other with high Sr (450-560 $\mu\text{g/g}$) and high La/Sm (1.3-2.2) (Supplementary Figure 9). Both
398 compositional parameters can be associated with a control by plagioclase. As LREE are more

399 compatible in plagioclase than HREE (Bindeman & Davis, 2000; Pichavant et al., 2024), co-precipitation
400 with plagioclase diminishes the (La/Sm)_{CN} ratio. As well, a decrease in Sr content in apatite is known
401 to reflect fractionation of a Ca-rich phase, such as plagioclase (e.g., Belousova et al. (2001)). For the
402 Revancha dyke, the impact of a thermal event has been to destabilized plagioclase, as evidenced by
403 dissolution features (Sandeman & Clark, 2004), which in turn would liberate Sr to the melt. Due to the
404 absence of other abundant and stable Ca-bearing phases in the Macusani subvolcanics, Sr is
405 expected to accumulate in the melt and result in progressively increasing Sr content in apatite. Thus,
406 the earlier apatite compositions, which crystallized together with plagioclase prior to the thermal
407 event, are expected to have relatively lower Sr and La/Sm values, whereas the post-thermal apatite
408 is expected to record an increase in both these parameters. Therefore, apatite with (La/Sm)_{CN}>1.2
409 and Sr>400 µg/g are accepted as the latest generation of apatite in Macusani subvolcanics and in
410 equilibrium with the host glass.

411 **4.6. Trace element mineral/melt partition coefficients**

412 Empirical partition coefficients (D(element)^{A/B}), defined as C^A/C^B, have been calculated from
413 mean trace element concentrations (µg/g weight basis) in the phase A (C^A) divided by trace element
414 concentrations in the phase B (C^B). The associated uncertainty on partition coefficients is calculated
415 from:

416
$$\sigma = D^{A/B} \times \sqrt{\left(\frac{SD}{X}\right)_A^2 + \left(\frac{SD}{X}\right)_B^2}$$
, in which σ is the uncertainty of D^{A/B} and SD is the standard deviation
417 of the measurements of the element X in each phase. A summary of the mineral/melt partition
418 coefficients for all elements that were above the limit of detection is provided in Tables 3 and 4 and
419 plotted in Figure 7.

420 *Apatite.* Values of D^{ap/gl} are summarized in Figure 7a, which includes comparison to the results of
421 experimental studies on basaltic-andesitic systems at 1.0 GPa and 1250 °C (Prowatke & Klemme,
422 2006), basanitic-granitic systems at 950-1120 °C, 0.75-2.0 GPa (Watson & Green, 1981), basaltic
423 system at 1050 – 1100 °C, 1.0 GPa (Ji & Dygert, 2024) and a study of a natural phonolite system at
424 950±25 °C and 0.2 GPa (Li et al., 2023). Also considered were the experiments of Stokes et al. (2019),
425 carried out in compositions ranging from trachyte to basalt at 1250-1400°C and 1.0 GPa. Among the
426 measured trace elements, the REE are the most compatible in apatite, with the lowest D^{ap/gl} values

427 for alkalis (Rb, Cs). The compatibility of the REE is a downward concave function of atomic number
428 with the highest D values recorded for Gd and the lowest being La and Lu. Overall, the empirical rare
429 earth element D values are up to 10x higher than the range reported in experimental studies, the
430 origin of which is discussed in the section below on mineral-melt equilibrium. Other compatible
431 trace elements include Ge and Mn with D values in all suites of ~ 20 and 10 , respectively. $D(\text{Ge})^{\text{ap/gl}}$
432 has not been previously reported but likely follows Si substituting for $(\text{PO}_4)^{3-}$ as the oxyanion
433 $(\text{GeO}_4)^{4-}$ (Pan & Fleet, 2002). Values of $D(\text{Mn})^{\text{ap/gl}}$ are consistent with experimental determinations
434 involving highly polymerized ($\text{NBO/T} = 0.03 - 0.10$) and peraluminous melts ($\text{ASI} = 1.0-1.3$) reported
435 by Stokes et al. (2019). Empirical partition coefficients for Sr, Th, U correspond to the upper limits of
436 the range recorded in the experimental studies of Ji & Dygert (2024). Values of $D(\text{V})^{\text{ap/gl}}$ from the
437 natural samples range between 0.5 and 4 , generally increasing with the $f\text{O}_2$ estimated for each suite,
438 with a further discussion of this provided below; we are unaware of any previous experimental
439 measurements of $D(\text{V})^{\text{ap/gl}}$ for comparison. Transition metals are increasingly incompatible with
440 increasing atomic number, ranging from $D(\text{Cu})^{\text{ap/gl}} \sim 1$ to $D(\text{Zn})^{\text{ap/gl}} \sim 0.1$, with the latter values for
441 $D(\text{Zn})^{\text{ap/gl}}$ consistent with the range reported by Ji & Dygert (2024). Apatite-melt partition
442 coefficients for Pb coincide with the lower limit of the experimentally determined range reported by
443 Prowatke & Klemme (2006) and Li et al. (2023). Like V, $D^{\text{ap/gl}}$ for Sn and Bi have not been reported from
444 experiments, with Bi showing weak incompatibility ($D^{\text{ap/gl}}$ of ~ 0.3 to 1), similarly for Sn, although the
445 D range is larger (0.05 to 1) and reflects some $f\text{O}_2$ dependence (see below). Elements from the LIL
446 and HFSE groups are the least compatible in apatite, with D values generally below 0.1 , overlapping
447 with the range of determinations from Prowatke and Klemme (2006), although the corresponding
448 uncertainties are large due to the low abundance of these elements in the natural samples.

449 *Biotite.* Values of $D^{\text{bt/gl}}$ are assembled in Figure 7b and compared to the experimental
450 determinations of Icenhower and London (1995), Stepanov and Hermann (2013), Pichavant et al.,
451 (2016), Gion et al. (2018), Were and Keppler (2021), Wei et al. (2024) and empirical determinations
452 from glassy volcanic rock suites (El Hoyazo dacite, SE Spain; Acosta-Vigil et al., 2010) including
453 previous measurements for the FCT (Bachmann et al., 2005) and the effusive Macusani suites
454 (Pichavant et al., 2024) related to the Macusani subvolcanics analyzed in this study. Previous biotite-
455 melt partitioning experiments were done on rhyolitic compositions over the temperature range of

456 600-1000 °C, pressures from 0.1 to 2.5 GPa and most fO_2 near FMQ+1, but Wei et al. (2024)
457 investigated FMQ-1 to FMQ+8.

458 Of the elements considered, the transition metals are generally the most compatible in
459 biotite, with the largest $D^{bt/gl}$ for V, Co, and Ni (>50), and other transition metals (Sc, Mn, Zn, Cu)
460 being moderately compatible ($D^{bt/gl}$ 1-10). Alkalis, alkali earth metals, and metalloids are moderately
461 compatible ($D^{bt/gl}$ 1-10; Ba, Rb, Ga, In) to moderately incompatible (Li, Cs, Sr, Ge, Pb, Bi with $D^{bt/gl}$
462 0.1-1). High field strength elements (Zr, Hf, W, Mo) are strongly incompatible ($D^{bt/gl}$ = 0.5-0.01).
463 $D(Nb)^{bt/gl}$ (2-10) exceeds the $D(Ta)^{bt/gl}$ (0.6-3) in all cases. Rare earth elements are the most
464 incompatible group with $D(REE+Y)^{bt/gl}$ <0.2, except Eu with $D^{bt/gl}$ of 0.1 to 1.0. The empirically
465 determined $D^{bt/gl}$ values determined in this study, overlap with the experimentally determined
466 range of partitioning coefficients. The values $D^{bt/gl}$ for Co, Ni, Zn, Mn, Nb, Ta, Ba, Rb, Cs, Mo, Eu, Gd,
467 Zr overlap with the experimental determinations by Were & Keppler (2021). Indium $D^{bt/gl}$ was found to
468 be sensitive to the biotite composition by Gion et al. (2018). Our empirical determinations
469 correspond with the experimental values by Gion et al. (2018) despite the natural biotites having a
470 higher annite component than any of the synthetic biotites reported by Gion et al (2018). For Y, Sc,
471 Ge, and Hf, we are not aware of any experimentally established $D^{bt/gl}$, however, our findings agree
472 with the other empirical determinations. Partition coefficient values for Sr (0.05-0.22) are within the
473 range found by Icenhower & London (1995), below the $D(Sr)^{bt/gl}$ value (0.57) reported by Were &
474 Keppler (2021) in a single, more calcic melt (1.87 wt% CaO, compared to <1.1 wt% in our samples and
475 Icenhower & London experiments) at 800 °C. Our determined range of $D(Li)^{bt/gl}$ (0.1-0.7) overlaps
476 with results from experiments in peraluminous systems (0.4-1.0) by Pichavant et al. (2016), and are
477 close to the range of $D(Li)^{bt/gl}$ (0.8-1.7) determined in three peraluminous experiments by Icenhower
478 & London (1995). Both sets of experiments indicate that $D(Li)^{bt/gl}$ is negatively correlated with melt
479 ASI and positively correlated with biotite Al^{IV} content, thus implying a melt and/or mineral
480 compositional effect on lithium partitioning. Results are also consistent with values measured by
481 Pichavant et al. (2016) whose melt composition (72.6-75.7 wt% SiO_2) and biotite Al^{IV} content (2.33-
482 2.56 a.p.f.u.) are close to our natural samples (72.3-74.8 wt% SiO_2 in glass, 2.28-2.61 Al^{IV} a.p.f.u. in
483 biotite).

484 Partitioning systematics for vanadium, tungsten, europium, and tin indicate a redox-
485 sensitivity. Vanadium $D^{bt/gl}$ decreases from 586 to 56 with increasing fO_2 with the range
486 corresponding to the results from El Hoyazo dacite (335-15) by Acosta-Vigil et al. (2012).
487 Experimental determinations of $D(V)^{bt/gl}$ by Were & Keppler (2021) point to a more moderate
488 compatibility (23-47) in biotite, however, their measurements were carried out in Ti-poor biotites
489 (<1.6 wt% TiO_2) in comparison to our compositions (3.9-4.5 wt% TiO_2). As discussed in Section 5.2,
490 TiO_2 content is expected to enhance vanadium partitioning. Values of $D^{bt/gl}$ for W decrease from
491 0.16 to 0.02 with increasing oxidation. This is below the determinations reported by Pichavant et al.
492 (2024) for the Macusani volcanics (0.38 ± 0.06) and from the experiments of Were & Keppler (2021)
493 (1.2 ± 0.8), but agrees with the findings of Dailey et al. (2018) involving the Spor Mountain topaz
494 rhyolite (0.06 ± 0.06). As tungsten is predominantly hexavalent even at the most reducing terrestrial
495 fO_2 conditions (O'Neill et al., 2008), this element is expected to be incompatible with most rock-
496 forming minerals (Arevalo & McDonough, 2008; Fonseca et al., 2014), which is inconsistent with the
497 relatively large partition coefficients reported by Were & Keppler (2021). The value of $D^{bt/gl}$ for Sn
498 varies between ~ 0.1 and 3, with an increase in values with fO_2 of the sample suite. This result is
499 consistent with the experimental measurements of $D(Sn)^{bt/melt}$ reported by Wei et al. (2024) in
500 which values increase from ~ 0.02 at FMQ-1 to ~ 3 at FMQ+8.

501 The empirical biotite-melt partition coefficients presented here are also generally consistent
502 with values reported for mineral/glass pairs from similar samples. Bachmann et al. (2005) measured
503 a number of the same trace elements in biotite and glass (as well as other phenocryst phases) from
504 samples of the FCT and showed similar values to our empirical determinations (Supplementary
505 Figure S8). Our results from the MAC subvolcanic samples are in general agreement with the results
506 for the Macusani tuffs reported by Pichavant et al. (2024) (Supplementary Figure S7), except values
507 for $D(Li)^{bt/gl}$ of 0.14-0.57 determined in this study are much lower than the value of ~ 3.7 reported for
508 the Macusani tuffs. Values of $D(Li)$ for the Macusani subvolcanics are consistent with results from
509 other suites in this study along with experimental determinations of Pichavant et al. (2016) and
510 Acosta-Vigil et al. (2012) involving melts of dacitic composition. Pichavant et al. (2024) suggest that a
511 secondary Li enrichment or redistribution in tuffs could have altered the Li content in phenocrysts
512 and matrix. Furthermore, we note that the composition of biotite from the samples for which $D^{bt/gl}$

513 were measured by Pichavant et al (2024) differ somewhat from those measured here, in that the
514 Macusani tuffs are generally more compositionally evolved, with higher Fe# (~0.65 – 0.80), Al₂O₃
515 (19.0-21.4 wt.%), and Rb content (912-2242 µg/g) compared to our samples (Fe#<0.54, Al₂O₃<19.7
516 wt.%, Rb<1150 µg/g). How these differences influence Li partitioning are not completely clear,
517 although of the intensive parameters that affect D(Li)^{bt/gl}, Icenhower and London (1995) document
518 an overall decrease in D(Li)^{bt/gl} with increasing temperature. We therefore speculate that the overall
519 more evolved nature of the Macusani tuff biotites could suggest a lower crystallization temperature,
520 and therefore a higher value of D(Li)^{bt/gl}.

521 **4.7. Oxybarometry of Macusani subvolcanics**

522 Apart from qualitative assessments by Pichavant et al. (1988a) and Sandeman & Clark (2003),
523 the fO₂ of Macusani igneous rocks, including the Macusani subvolcanics, has not been determined
524 quantitatively. This is necessary, however, to assess fO₂ controls on heterovalent element
525 partitioning. Here, we use the major and REE compositions of Macusani zircon and glass
526 compositions along with the Ce-in-zircon oxybarometer of Smythe & Brenan (2016) to determine the
527 oxygen fugacity of the Revancha dyke (measured in sample MAC137) and the Cerro Esquinani stock
528 (MAC 160) samples. As described above, zircon occurs in both sample suites as small (<50 µm),
529 euhedral crystals, exhibiting well-developed, concentric growth zoning, with rare textural evidence
530 for inheritance. In total, 24 zircon and 75 glass analyses were obtained from these samples.
531 Analysis of the zircons was particularly challenging because of their small size, and therefore
532 susceptibility to contamination by the laser sampling inclusions of other minerals, or surrounding
533 glass. To minimize the non-zircon contribution, the time-resolved spectrum for each zircon analysis
534 was carefully reviewed, and the REE and zircon-incompatible element (Na, Al) patterns were used to
535 filter those subject to contamination within the ablated volume. Following this, 11 measurements
536 from the Revancha dyke and 4 measurements from the Cerro Esquinani stock were accepted as
537 representative of uncontaminated zircon trace element compositions.

538 The oxybarometer of Smythe & Brenan (2016) uses the concentrations of Ce in zircon and
539 melt, as well as estimates of D(Ce³⁺)^{zrn/melt} and D(Ce⁴⁺)^{zrn/melt} obtained from linear interpolation of
540 trivalent REE and tetravalent element (Th, U, Hf, Zr) partition coefficients expressed as a function of
541 ionic radii (Shannon, 1976) to calculate the proportions of the Ce³⁺ and Ce⁴⁺ species in the melt.

542 Results are then compared to a calibration that expresses species proportions as a function of fO_2 ,
543 melt composition (including H_2O content) and temperature. Zircon crystallization temperatures
544 were calculated using Ti concentrations following the expression of Ferry & Watson (2007) and Ti
545 activity following Borisov & Aranovich (2020). The melt H_2O content estimate (4.2 wt% for MAC137,
546 4.8 wt% for MAC160) is based on the EPMA totals, which agrees with the H_2O estimate in Macusani
547 tuffs (4.5-6.5 wt%) reported by Pichavant & Montel (1988). The measured trace element
548 concentration of zircon, and resulting oxygen fugacities are provided in the Supplementary Table S1.
549 The oxybarometry results suggest similar, reduced fO_2 values for both Macusani subvolcanic units:
550 FMQ- 2.8 ± 1.1 for the Revancha dyke and FMQ- 1.9 ± 1.0 for the Cerro Esquinani stock. This is
551 consistent with the absence of magnetite and the very low hematite content ($<1\%$ Fe_2O_3) in ilmenite
552 from the Revancha dyke and Macusani tuffs (Pichavant et al., 1988b; Sandeman & Clark, 2003).

553 **5. Discussion**

554 **5.1. Evidence for crystal-melt equilibrium**

555 *Textural evidence*

556 Biotite crystals have been observed in all of the analyzed samples, occurring as ubiquitous,
557 lamellar phenocrysts and microphenocrysts. Phenocrysts are chemically uniform and euhedral in
558 FCT and TT samples, whereas the larger biotites from both MAC and MM samples frequently exhibit
559 resorption features and compositional zoning observable in both optical and BSE imaging. Free
560 microphenocrysts, however, are commonly euhedral and unzoned, with the exception of the
561 Revancha dyke, where reversly zoned biotite is present (Fig. 2c).

562 Apatite in the sample suite is present in trace amounts as microphenocrysts and biotite-
563 hosted inclusions. Apatite microphenocrysts are commonly euhedral, and tabular to equant. In most
564 samples apatite is chemically uniform, with rare cases of concentric growth zoning or inherited,
565 partially resorbed cores, as observable in BSE imaging (Fig. 2e). Apatites from the UP, however,
566 commonly display bright, up to 20-30 μm thick rims in BSE images, suggesting at least two stages of
567 apatite growth. In most samples, apatite phenocrysts are free from inclusions, with the exception of
568 Revancha dyke samples, where apatite phenocrysts (ocasionally exceeding 1000 μm size) contain a
569 multitude of mineral (monazite, zircon) and melt inclusions.

570 As natural intra-crystal and intercrystal compositional variation is present in at least some of
571 the samples, further verification of mineral-melt equilibria must be provided, as described in the
572 sections that follow.

573 *Mineral /melt equilibria*

574 Comparison to experimentally established major element exchange coefficients (K_d) and
575 trace element D values for mineral/melt partitioning enable evaluation of the chemical equilibrium
576 between biotite, apatite, and glass from the natural samples. Biotite-glass major element
577 equilibrium was assessed using Fe-Mg exchange partitioning, expressed as $K_d(\text{Fe-Mg}) = (\text{Fe/Mg})_{\text{biotite}}$
578 $\times (\text{Mg/Fe})_{\text{melt}}$ (Fe and Mg as molar proportions). Figure 8a provides a comparison of $K_d(\text{Fe-Mg})$ values
579 determined in the natural samples to the results of the experimental studies involving water-
580 saturated granitic melts (Were & Keppler, 2021; Icenhower & London, 1997). Results of the
581 experimental studies suggest an overlapping range of $K_d(\text{Fe-Mg})$ from 0.060 to ~0.177 that would be
582 characteristic of biotite and granitic melts in equilibrium. The range of $K_d(\text{Fe-Mg})$ from the natural
583 samples is 0.06 to 0.277, which is similar to the experimentally determined values, consistent with
584 Fe-Mg exchange equilibrium.

585 Experimentally established values of $D(\text{Sr})^{\text{ap/gl}}$ (Prowatke & Klemme, 2006; Watson & Green,
586 1981) were used to assess apatite-melt equilibrium. Strontium was selected for verification of
587 equilibrium due to its measureable abundance in the analyzed glasses and high compatibility in
588 apatite. Most of the $D(\text{Sr})^{\text{ap/gl}}$ values obtained in this study are similar to or greater than the highest
589 values reported from experiments (~5; Prowatke and Klemme, 2006). Significantly, Prowatke and
590 Klemme (2006) found a strong negative correlation between the melt CaO content and $D(\text{Sr})^{\text{ap/gl}}$,
591 with the highest partition coefficients recorded for the most CaO poor melts (i.e., ~5 wt% CaO;
592 Figure 8b). A less pronounced trend is also seen in the results from Watson and Green (1981).
593 These data are shown in Figure 8b, along with values determined in this study. Our results plot at
594 the low CaO (i.e., <1 wt%) extension of the experimentally-determined correlation. Therefore,
595 although $D(\text{Sr})^{\text{ap/gl}}$ measured for the natural samples do not overlap with the experimental
596 measurements, values seem to be predicted from the trends established by the experimental data.

597 Another test for mineral-melt equilibrium is to compare partition coefficients for isovalent
 598 series of elements to expectations of the so-called lattice strain model, as formulated by Blundy and
 599 Wood (1994). In this model, the total change in free energy for the substitution of a trace element,
 600 I, for the “primary” cation, J, on a normal lattice site, can be represented by the reaction:

$$601 \quad \Delta G_I^0 = \Delta G_J^0 + \Delta G_{strain}^{melt} - \Delta G_{strain}^{crystal} \quad (1)$$

602 where ΔG_J^0 and ΔG_I^0 describe the free energy of melting for the I and J end-members, ΔG_{strain}^{melt} and
 603 $\Delta G_{strain}^{crystal}$ refer to the strain energies induced by replacing one mole of J by one mole of I in an
 604 infinite J-endmember melt and crystal. As the strain energy of substitution into the melt is
 605 insignificant, the equilibrium constant, K_I , for the I-J substitution can be expressed as:

$$606 \quad K_I = \exp\left(\frac{-\Delta G_J^0 + \Delta G_{strain}^{crystal}}{RT}\right) = K_0 \exp\left(\frac{\Delta G_{strain}^{crystal}}{RT}\right) \quad (2).$$

607 Assuming that the activity coefficient of the J-endmember is constant and near unity and the activity
 608 of both end-members in melt are identical (which is likely due to the the identical charge) the
 609 equilibrium constants in Eq. 2 can be related to the partition coefficients (D):

$$610 \quad D_I = D_0 \exp\left(\frac{-\Delta G_{strain}^{crystal}}{RT}\right) \quad (3),$$

611 where D_I and D_0 are the mineral/melt coefficient of I and J, respectively, the latter being unhindered
 612 by strain related to entering the crystal lattice.

613 By applying the Brice (1975) expression of the mechanical strain energy around a
 614 homovalent cation defect as a function of Young’s Modulus (E) of a host crystal, the size of the
 615 lattice site (r_0), the substituent cation (r_i), and Avogadro’s number (N_A), Blundy and Wood
 616 formulated the trace element partition coefficient at specific pressure (P), temperature (T), and
 617 composition (X) as a function of the “strain-compensated partition coefficient” [$D_0(P,T,X)$] as:

$$618 \quad D_I(P, T, X) = D_0(P, T, X) \cdot \exp\left[\frac{-4\pi EN_A \left[\frac{r_0}{2}(r_i - r_0)^2 + \frac{1}{3}(r_i - r_0)^3\right]}{RT}\right] \quad (4)$$

619 in which R is the gas constant and T is degrees K. Assuming crystal-melt equilibrium, at constant P, T
 620 and X, D_i values for a series of isovalent trace elements is a function of r_i with the maxima at strain-

621 free substitution ($r_i=r_0$) and decreasing D_i as the mismatch between r_i and r_0 (and therefore the
622 mechanical strain in the crystal lattice) increases. Thus, plots of D_i versus r_i , termed Onuma diagrams
623 (Onuma et al., 1968), result in concave functions with maxima at D_0 and r_0 , and the width of the
624 parabola decreasing with increasing E . The value of r_0 is primarily controlled by the mineral
625 composition, whereas E is controlled by the ionic charge (Wood & Blundy, 2013). The correlation
626 between D_i and the r_0-r_i mismatch has been confirmed experimentally and empirically in a great
627 number of mineral/silicate melt partitioning studies (e.g., Beattie, 1994; Lee et al., 2007; Shimizu et al.,
628 2017; van Westrenen & Draper, 2007; Zajacz & Halter, 2007) including several focused on biotite
629 (LaTourrette et al., 1995; Schmidt et al., 1999; Were & Keppler, 2021) and apatite (Klemme & Dalpé, 2003; Li
630 et al., 2023; Prowatke & Klemme, 2006). Thus, results for mineral-melt equilibrium are tested by
631 adherence to the expectations from the successful Blundy-Wood lattice strain model.

632 In applying the Blundy-Wood model, temperatures of crystal-melt equilibrium were
633 estimated from the Ti-in-biotite calibration of Henry et al. (2005) due to the peraluminous and
634 titania-rich sample compositions, which are saturated with ilmenite or other Fe-Ti oxide phase.
635 Values of D_0 , r_0 , and E were determined using least squares regression for each isovalent series of
636 trace element D_i values (Supplementary Table ST7). Values of r_i for a specific trace element will
637 depend on both ionic charge and coordination (Shannon, 1976), and were therefore selected with
638 guidance from previous partitioning and mineral structural studies (Padilla & Gualda, 2016; Pan & Fleet,
639 2002; Pichavant et al., 2024; Were & Keppler, 2021) and size-charge considerations. Partitioning arrays
640 are shown in Figures 9 and 10 for apatite and biotite, respectively.

641 The apatite structure contains three types of cation sites: VII- and IX-fold coordination
642 (generally occupied by Ca with r_0 being 0.106 in VII-fold and 0.118 in IX-fold coordination) along with
643 tetrahedrally coordinated site typically containing phosphorous with $IR=0.017$ nm (Pan & Fleet, 2002).
644 Here it is assumed that all of the ions with IR exceeding 0.07 nm in VIII-fold coordination solely enter
645 the VII- and IX-fold sites, with radii corresponding to an intermediate VIII-fold coordination.

646 Divalent and trivalent cations are the most compatible with the VII- and IX-fold coordinated
647 sites. Both of the isovalent arrays adhere to concave D_i-r_i functions with similar r_0 values (0.111-
648 0.113 nm for divalent and 0.106-0.108 for trivalent ions) with the trivalent array recording higher E

649 (270-349 MPa) and D_0 (103 – 177) than the divalent series ($E=250-303$ MPa, $D_0=64-129$). The
650 proximity of D_0 of the trivalent series to the Ca^{VII} site indicates a REE preference for entering in the
651 smaller Ca^{VII} site, supported by earlier studies (Pan & Fleet, 2002). The larger r_0 values of the divalent
652 array place it between the two Ca sites thus suggesting an even divalent ion distribution between
653 Ca^{VII} and Ca^{IX} . Several of the less compatible divalent elements (Zn, Mg, Pb, Ba), however, show
654 deviations from fitted D_i - r_i functions. Each of these elements show a preference for one of the Ca
655 sites: Pb, Ba, Zn preferentially enter the Ca^{VII} site, but Mg the Ca^{IX} site (Elliott, 1994; Pan & Fleet, 2002).
656 The partitioning of Mg, however, is enhanced by high melt polymerization with the effect amplified
657 at low temperature (Zhan et al., 2022). Experimentally determined D_{Mg} in low-P-T siliceous
658 peraluminous systems exceed unity (Trend 2 - Zhan et al., 2022), which coincides with the elevated
659 D_{Mg} values (up to 6.0) in the Macusani samples.

660 Similar to the trivalent series, the tetravalent series (Hf-Zr-Th) with $r_0=0.106-0.109$ indicate
661 affinity for the Ca^{VII} site as previously described by Luo et al. (2009). Related to the tetravalent
662 series, the ratio of $D_{\text{U}}/D_{\text{Th}}$ is below 1 in the reduced Macusani rocks, equals 1 in Tuk-Tuk tuff, and
663 exceeds 1 in the oxidized Fish Canyon tuff. While thorium exists exclusively in the tetravalent state,
664 uranium in silicate melts can be present in valence states (Schreiber, 1983) of U^{4+} (IR=0.100 nm in
665 VIII-fold coordination), U^{5+} (IR=0.084 nm in VII-fold coordination), U^{6+} (IR=0.081 nm in VII-fold
666 coordination). With its charge and size being the closest to Ca^{2+} in VII-fold coordination, U^{4+} is the
667 most compatible in the apatite structure (Clarke & Altschuler, 1958). Thus, $D_{\text{U}}/D_{\text{Th}}$ is likely to vary as a
668 function of $\text{U}^{4+}/\Sigma\text{U}$ in melt, which at least in part is controlled by the $f\text{O}_2$, which stabilizes the more
669 compatible U^{4+} under reduced conditions (Fonseca et al., 2014).

670 Monovalent ions are generally incompatible ($D_i < 0.1$) in the apatite structure. The arrays of
671 Na-K-Rb reach the maxima at near r_{Na} ($r_0=0.115-0.120$), which suggests a preference for entering the
672 larger, IX-fold coordination site. D_{Li} , however, exceeds the values expected from the monovalent r_i -
673 D_i fit. The relatively lower IR of lithium (0.092 nm in VIII-coordination with no data about any higher
674 coordination) could lead to a preference for a lower coordination.

675 Although the relative apatite-melt partitioning of the trivalent REE + Y is consistent with the
676 lattice strain model, as mentioned previously, absolute values of partition coefficients for this

677 element group are up to 10 times higher than those reported in previous experimental studies
678 (Watson & Green, 1981; Prowatke & Klemme, 2006). Mineral or melt composition effects may serve as
679 possible explanations, as past work has shown that the $D(\text{REE})^{\text{ap/gl}}$ increases both with the Si content
680 in apatite and the degree of melt polymerization, the latter simply expressed as melt SiO_2 content.
681 The Si contents of the apatites measured in this study are comparable to those produced in past
682 experiments, so that is an unlikely cause. However, the natural glasses are significantly more
683 evolved ($\text{SiO}_2 = 72\text{-}75$ wt.%) than the range from previous experimental studies ($\text{SiO}_2 = 36\text{-}70$ wt%).
684 Prowatke & Klemme (2006) combined their data with the results from Watson and Green (1981) to
685 show that $D(\text{Sm})^{\text{ap/gl}}$, a representative REE, increases approximately exponentially with melt SiO_2
686 content. This relationship is shown in Figure 11, along with results from this study, Little Glass
687 Mountain (LGM) rhyolite (USA) reported by Brophy et al. (2011), and from Erebus (Antarctica),
688 reported by Li et al. (2023). Values of $D(\text{Sm})^{\text{ap/gl}}$ determined in this study are similar to those
689 measured for the LGM sample, which is consistent with overlapping glass SiO_2 concentrations. All
690 datasets seem to project smoothly from the experimental results, suggesting that the unusually
691 large values of $D(\text{Sm})^{\text{ap/gl}}$ (and by extension other REE + Y) measured in this study are the result of
692 melt composition control.

693 As for biotite, its structure comprises three kinds of cation sites – XII-fold coordinated
694 (usually hosting LILE, e.g. K), VI-fold coordinated, most commonly hosting di- and trivalent elements
695 (e.g., Mg, transition metals, REE), and a IV-fold coordinated site, typically occupied by Si or Al
696 (Bailey, 1984). The Onuma diagram for biotite-melt partitioning (Figure 10) reveals five groups of
697 concave isovalent element arrays: monovalent elements in XII-fold coordination (comprising Na, K,
698 Rb, Cs), divalent elements in VI-fold coordination (Mg, Co, Fe, Mn), trivalent elements in VI-fold
699 coordination (Ga, Sc, In, Lu, Yb, Y), trivalent elements in IV-fold coordination (Al, Ga, In), and
700 tetravalent elements in IV-fold coordination (Si, Ge, Hf, Zr). For the XII-fold coordinated site, the
701 monovalent element array peaks at $r_0 = 0.164\text{-}0.170$ nm with $D_0 = 1.6\text{-}2.1$, consistent with K as the
702 most suitable occupier. Divalent Ba^{XII} has an $r_0 = 0.161$ nm, which results in high $D(\text{Ba})^{\text{bt/gl}}$ values (2.4-
703 8.4), however, developing a meaningful Brice fit for divalent elements is precluded by the large
704 uncertainties of $D(\text{Ca})^{\text{bt/gl}}$ and the electron configuration of Pb, which leads to formation of partial
705 covalent bonds, which do not obey the Wood-Blundy $r_i\text{-}D_i$ model (Engel et al., 1975; Were & Keppler,

706 2021). The biotite octahedral site is known to accommodate cations of several valence states
707 (Nickel, 1954). In this study, two isovalent arrays are fitted: divalent elements form the higher D tier
708 with $r_0 = 0.065 - 0.070$ nm and $D_0 = 165-447$, compared to the trivalent cation array with overlapping
709 $r_0 = 0.067-0.072$ and lower D_0 values = 2.7-13.0. The r_0 value of the divalent array appears to
710 decrease with increasing Al content and the opposite is true for the trivalent array. In the divalent
711 series, Mg^{2+} (IR=0.072 nm in VI-fold coordination) is the closest to r_0 thus it is the most compatible
712 element. In the trivalent series, the octahedral site r_0 values are similar to the ionic radii of Ga and
713 Sc (0.062 and 0.0745 nm, respectively) and positively correlate with the biotite alumina content thus
714 implying that the size of the octahedral cation sites for divalent and trivalent elements is altered by
715 the abundance of Al. Ionic radii of several highly-charged ions are close to the r_0 of the octahedral
716 site: Ti^{4+} (IR=0.0605 nm), V^{3+} (0.064 nm), V^{4+} (0.058 nm), Nb^{5+} and Ta^{5+} (both 0.064 nm), Sn^{4+} (0.069
717 nm), which explains their compatibility in the analyzed biotite suites. Given that the D_i-r_i curves for
718 the highly charged elements would be much narrower than that of divalent elements (Blundy &
719 Wood, 1994), even a minor change in the r_0 of the site due change to the crystal chemistry can
720 strongly alter the D_i values of the HFSE, therefore biotite Al^{VI} could be important when considering
721 and comparing the D values of other, octahedrally coordinated elements.

722 In general, the empirical partitioning measurements are consistent with experimental
723 measurements, either as overlapping values, or on the extension of trends with other melt
724 composition parameters (e.g., wt% CaO, wt% SiO_2). Onuma diagrams defined for biotite- and
725 apatite-melt partitioning of similarly-sized isovalent cations display parabolic relations with values of
726 r_0 and D_0 consistent with the major substituent cations for a particular site. Results therefore
727 suggest that the mineral/melt partitioning of the trace elements measured for the natural samples
728 broadly adhere to the systematics established by the experimental database, and by extension,
729 reflect crystal-melt equilibrium.

730 **5.2. Redox control on heterovalent element partitioning**

731 Amongst the group of elements for which empirical partition coefficients have been
732 determined, several are expected to have multiple valence states over the range in fO_2 of terrestrial
733 magmas. These include V (2+, 3+, 4+, 5+), As (3+, 5+), Eu (2+, 3+), Mo (4+, 6+), Sn (2+, 4+) and W (4+,

734 6+) (Canil, 1999; Mallman and O'Neill, 2009; Maciag & Brennan, 2020; Drake, 1975; Linnen et al., 1995;
735 1996; Holzheid et al., 1975; Fonseca et al., 2014). As shown in Figure 12, all of these elements show
736 a systematic variation in values of $D^{\text{mineral/glass}}$ with the estimated fO_2 of each magmatic suite, which
737 here we ascribe to a predominant control of fO_2 on the ionic radius and charge of progressively
738 changing proportions of cation species.

739 The partitioning of vanadium between biotite and melt is highest (up to 585) in the most
740 reduced end of the sample suite (Macusani subvolcanics), while the lowest $D(V)^{\text{bt/gl}}$ is found in the
741 most oxidized rocks (Fish Canyon tuff). The opposite trend is observed for $D(V)^{\text{ap/gl}}$. The difference is
742 further amplified if apatite/biotite partitioning is considered – $D(V)^{\text{ap/bt}}$ changes from 0.001 in the
743 reduced MAC137 to 0.547 in the oxidized Mascota minette. As described in the introduction, the VI-
744 fold coordination ionic radii of the species V^{2+} , V^{3+} , V^{4+} , V^{5+} are 0.079, 0.064, 0.058 and 0.054 nm,
745 respectively, hence the V^{2+} and V^{4+} species are suitable substituting for divalent Mg or Fe and Ti^{4+} ,
746 leading to their compatibility in biotite at lower fO_2 , but relative exclusion of V^{5+} at higher fO_2 . Only
747 V^{5+} exhibits a potential for being compatible in the apatite structure, as the oxyanion $(VO_4)^{-3}$ can
748 substitute for $(PO_4)^{-3}$ (Pan & Fleet, 2002). Apatite VII- and IX-fold coordinated sites (usually occupied
749 by Ca^{2+}), however are too large to accommodate any of the other vanadium species. As the higher
750 charged V species are stabilized in oxidized melts, the higher abundance of more compatible V^{5+} is
751 expected to enhance the overall vanadium compatibility in apatite, which is consistent with the
752 observed increase in $D(V)^{\text{ap/gl}}$ with fO_2 .

753 In contrast to vanadium, values of $D(Sn)^{\text{mineral/melt}}$ increase with fO_2 for *both* biotite and
754 apatite, and this sympathetic relation results in essentially constant values of $D(Sn)^{\text{ap/bt}}$ (0.40 ± 0.24)
755 over the fO_2 range of the sample suites. The change in the biotite- and apatite-melt partition
756 coefficients likely reflects the difference in compatibility of the Sn^{2+} and Sn^{4+} species, and their
757 changes in proportion with fO_2 . At \sim FMQ and below, Sn^{2+} is the predominant species in
758 peraluminous melt compositions (Linnen et al., 1996; Farges et al., 2006), with an estimated ionic
759 radius of 0.111 nm in VI-fold coordination (Uchida et al., 2002). Divalent Sn is therefore a poor fit for
760 isovalent substitution with Mg^{2+} (IR = 0.072 nm) or Fe^{2+} (IR = 0.078 nm) in biotite, whereas Sn^{4+}
761 (IR=0.069 nm) is close in size to Ti^{4+} (IR = 0.061 nm). The increase in $D(Sn)^{\text{bt/gl}}$ with increasing fO_2 is

762 therefore consistent with an increased abundance of Sn^{4+} and its preferential substitution for Ti^{4+} in
763 the biotite structure. This interpretation is consistent with the experimental results of Wei et al.
764 (2024) who found strong positive correlations between $D(\text{Sn})$ and $D(\text{Ti})$ for biotite and other
765 ferromagnesium minerals obtained under highly oxidized conditions, at which the Sn^{4+} species
766 would dominate. As for apatite, although the Sn^{2+} species would be a suitable fit for either of the
767 two large cation sites in apatite (IR = 0.106 and 0.118 nm in VII- and IX-fold coordination), this is
768 inconsistent with low values of $D(\text{Sn})^{\text{ap/gl}}$ for the lowest $f\text{O}_2$ samples. However, when ionized to the
769 2^+ state, tin donates two 5p electrons and obtains a stable filled $5s^2$ electron configuration, resulting
770 in an inert pair effect. This likely plays an inhibiting role for the incorporation of Sn^{2+} into apatite
771 (and likely biotite as well), which would otherwise be a suitable fit from size considerations alone. In
772 contrast to the 2^+ species, Sn^{4+} lacks the filled shell configuration, and therefore would have a higher
773 affinity for the apatite structure. In tetrahedral coordination, the IR of Sn (0.055 nm) is relatively
774 close to the IR of Ge (0.039 nm), which is one of the most compatible trace elements in the apatite
775 structure ($D(\text{Ge})^{\text{ap/gl}}$ of ~8-20). Therefore, despite Sn^{4+} being a poorer fit than Sn^{2+} , the more
776 favorable bonding environment for the former seems to overcome this size mismatch, accounting
777 for the increase in $D(\text{Sn})^{\text{ap/gl}}$ with $f\text{O}_2$.

778 Arsenic is found to become more compatible in apatite with increasing $f\text{O}_2$ (from 0.04 to
779 1.6). This element was not detected in biotite from most samples, however, thus precluding
780 $D(\text{As})^{\text{bt/gl}}$ estimates. In silicate melts, arsenic is present as As^{3+} and As^{5+} in proportions primarily
781 controlled by the $f\text{O}_2$ with the As^{3+} being the dominant species in natural silicate melts (Maciag &
782 Brenan, 2020). Pentavalent arsenic, however, likely is compatible with apatite as it enters solid
783 solutions with apatites forming the arsenate endmembers (Pan & Fleet, 2002), where As^{5+} (IR = 0.0335
784 nm in tetrahedral coordination) substitutes for P^{5+} (IR = 0.017 nm). Due to the size and charge
785 mismatch As^{3+} (IR = 0.058 in octahedral coordination) is much less likely to enter any of the cation
786 sites in apatite structure. Thus, the increasing compatibility of As in apatite could be caused by a
787 shift to higher melt $\text{As}^{5+}/\text{As}^{3+}$ values, a prediction borne out by the apatite/melt partitioning
788 experiments reported in Maciag (2023) involving felsic melt compositions.

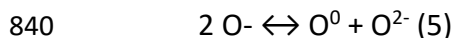
789 Tungsten is incompatible in both minerals, with $D(W)^{bt/gl}$ decreasing with fO_2 , but no
790 systematic change in $D(W)^{ap/gl}$ across the same fO_2 interval. The decrease in $D(W)^{bt/gl}$ could result
791 from a change in speciation from W^{4+} to W^{6+} , as W^{4+} has an IR=0.066 nm, allowing a good fit into the
792 biotite octahedral site, with an appropriate charge compensation mechanism (e.g., $^{VI}Fe^{3+} + ^{IV}Si^{4+} =$
793 $^{VI}W^{4+} + ^{IV}Al^{3+}$). On the contrary, partitioning of W^{6+} into either biotite or apatite is inhibited by the
794 large excess of charge, and the general exclusion of W^{6+} from silicate minerals is well documented
795 (e.g., Fonseca et al., 2014). Although the change in $D(W)^{bt/gl}$ seems consistent with a change in
796 speciation, available W solubility data indicates that the fO_2 at which the transition from W^{4+} to W^{6+}
797 takes place is ~FMQ-7 (O'Neill et al., 2008), which is far more reduced than the conditions recorded
798 by the sample suite. In contrast, Fonseca et al. (2014) provide evidence from mineral-melt
799 partitioning experiments for the presence of W^{4+} and W^{6+} in the range of FMQ to FMQ-4, as
800 revealed by large changes in the $D(W)^{mineral/melt}$ for olivine and pyroxene. Fonseca et al. (2014)
801 account for this discrepancy with the solubility data by proposing that melt composition may play a
802 role in W speciation, either by the stabilization of the $CaWO_4$ complex (O'Neill et al., 2008) or by
803 affecting the fO_2 of the W^{4+} to W^{6+} transition. In terms of the latter, by analogy to the geochemically
804 similar molybdenum, it has been shown that melt compositions in the MgO-Al₂O₃-SiO₂ system
805 exhibit the Mo^{4+} to Mo^{6+} transition at almost 2 log units higher fO_2 than melts in the CaO-Al₂O₃-SiO₂
806 system (O'Neill and Eggins, 2002). Fonseca et al. (2014) emphasize that even small changes in the
807 fO_2 of the W^{4+} to W^{6+} transition could impact partitioning given the large differences in the
808 compatibility of the two species. Our results for Mo partitioning between biotite and glass, indeed,
809 follow a similar pattern to tungsten with decreasing compatibility ($D(W)^{bt/gl} = 2 - 0.1$) reflecting a
810 transition from the compatible Mo^{4+} (IR = 0.065 nm in octahedral coordination) to the highly
811 charged, incompatible Mo^{6+} (IR = 0.059 nm), which takes place at more oxidized conditions (~FMQ-
812 4; Holzheid et al., 1994), closer to the fO_2 range of the sample group. Therefore, a higher proportion
813 of the compatible Mo^{4+} could lead to a higher $D(Mo)^{bt/gl}$ values in comparison $D(W)^{bt/gl}$. As
814 molybdenum was not detected in most of the sampled apatite compositions, $D(Mo)^{ap/gl}$ could not be
815 determined.

816 Values of $D(Eu)^{bt/gl}$ do not show a systematic change with fO_2 , however, $D(Eu)^{ap/gl}$ increases
817 with more oxidizing conditions (Figure 12a). Europium in silicate melts is present in two valence

818 states – Eu^{2+} and Eu^{3+} (Drake, 1975). Experimental studies have shown that both valence states are
819 present over the $f\text{O}_2$ range represented by the sample suite, and that the $\text{Eu}^{3+}/\Sigma\text{Eu}$ increases with
820 $f\text{O}_2$ (as well as T, and decreasing melt polymerization; Burnham et al., 2015). Due to the larger size
821 (0.120 nm in VII-fold coordination), Eu^{2+} is expected to be less compatible than Eu^{3+} (0.101 pm in VII-
822 fold coordination) with either cation site in apatite. The observed increase in $D(\text{Eu})^{\text{ap/gl}}$ with
823 increasing $f\text{O}_2$ is therefore consistent with the preferential uptake of the more compatible Eu^{3+}
824 relative to Eu^{2+} .

825 **5.3. Estimate of the redox control on vanadium intermineral partitioning systematics**

826 As mineral/melt partitioning of vanadium for apatite and biotite follow diverging trends with
827 $f\text{O}_2$, results suggest that the intermineral partitioning of vanadium is a potential oxybarometer. As
828 discussed above, the observed change in $D(\text{V})^{\text{ap/bt}}$ is generally consistent with differences in species
829 compatibility into the apatite and biotite structures as predicted from ionic radius and charge.
830 However, a concern is whether the increase in $D(\text{V})^{\text{ap/bt}}$ with $f\text{O}_2$ is simply due to the $f\text{O}_2$ control on
831 vanadium speciation, or reflects other factors that could influence species proportions without a
832 change in $f\text{O}_2$, notably melt composition. This latter effect arises because the redox equilibria
833 between the species of multivalent elements are controlled by the balance between the three kinds
834 of oxygen bonding in the silicate melts: singly bonded O^- , doubly bonded O^0 , and O^{2-} , free oxygen
835 (Fincham & Richardson, 1954; Moretti, 2005). O^0 forms a covalent bond with Si^{4+} or other highly
836 charged network formers in tetrahedral coordination (thus earning the name of bridging oxygens or
837 T), but O^- form ionic bonds with network modifiers and are therefore denoted as ‘non-bridging
838 oxygens’ (NBO). The balance between the three kinds of oxygens in silicate melts is described in the
839 following equation:



841 The ratio of NBO/T describes the melt structure and viscosity with its values ranging
842 between 0 (fully polymerized melt) and 4 (fully depolymerized melt), yet in natural silicate melts, it
843 generally varies between 0 and 1 (Mysen, 1983). NBO/T is inversely correlated to the melt basicity
844 (Λ), which is controlled by the activity of the metal network modifiers. Thus, the melt polymerization
845 and its acid-base character, which determines the stability of heterovalent element ligands, are

846 linked. Generally, the oxidation-reduction equilibria are expected to shift toward the more oxidized
847 species with increasing melt basicity (higher NBO/T), which coincides with lower polymerization
848 (Cicconi et al., 2020). However, as the heterovalent element equilibria are subject to both redox and
849 acid-base chemistry, the potential amphoteric nature of one of the species (e.g., Fe³⁺) can be
850 affected by additional significant variables. For example, in peraluminous systems, increasing alkali
851 content leads to stabilization of Fe²⁺, while the opposite is true in metaluminous and peralkaline
852 systems. This illustrates the necessity for experimental investigations of compositional controls of
853 each equilibrium, which have proven to be essential in a number of studies on heterovalent element
854 species and partitioning including iron (Cicconi et al., 2015; Dingwell & Virgo, 1987; Lange & Carmichael,
855 1987; Ottonello et al., 2001), sulphur (Nash et al., 2019; O'Neill & Mavrogenes, 2002), tin (Linnen et al.,
856 1996), cerium (Smythe & Brenan, 2015), and vanadium (Arató & Audétat, 2017a; Leuthold et al., 2023;
857 Mallmann & O'Neill, 2013; Sossi et al., 2018). The melt structural control of vanadium species in silicate
858 systems is experimentally studied by McKeown et al. (2011) and Wang et al. (2016). McKeown et al.
859 measured the V speciation in borosilicate glasses synthesized at 1050 °C and 0.1 MPa with varying
860 alkali contents. They found a positive correlation between the melt Na₂O content and the average V
861 oxidation state in the glass, measured by XANES. They remark that this is consistent with with the
862 results for Cr in less polymerized melts reported by Berry et al. (2006), in which a higher proportion
863 of network modifying cations stabilizes the Cr³⁺ over Cr²⁺. Similarly, in their study of the CaO-MgO-
864 Al₂O₃-SiO₂-VO_x system, Wang et al (2016) found that a higher basicity, defined as
865 $(\text{CaO}+\text{MgO})/(\text{SiO}_2+\text{Al}_2\text{O}_3)$, stabilizes the higher oxidation state of vanadium. As redox reactions are
866 endothermic, higher temperatures are expected to stabilize the reduced species – this is confirmed
867 by the Wang et al., (2016) experiments for several compositions. Therefore, we interpret the
868 unusually large values of $D(\text{V})^{\text{ap/bt}}$ for the Mascota sample as likely the result of melt composition
869 (see below), even though the equilibration temperatures (1080-1100°C) are higher than for the
870 other sample suites (634-825°C).

871 To verify that the observed vanadium partitioning patterns originate predominantly from the
872 redox control on heterovalent element species instead of melt structural controls, we likewise plot a
873 set of homovalent elements against the sample $f\text{O}_2$ state. In Figure 13a, a set of trivalent,
874 tetravalent, and pentavalent element $D^{\text{ap/bt}}$ values from all samples except the Mascota minette are

875 plotted in the fO_2 space. Results from the Mascota minette are excluded due to the effect of
 876 significantly higher alkali content, which sets them apart from the rest of the analyzed samples with
 877 overlapping T ranges (Table 1) and comparable peraluminous compositions (Figure 3). Within the
 878 peraluminous, low-T group, the $D^{ap/bt}$ values of homovalent elements show no correlation with the
 879 sample fO_2 , thus precluding any role of melt structure overprinting the redox effect on heterovalent
 880 element partitioning. Following the experimental studies of McKeown et al. (2011) and Wang et al.
 881 (2016), the relatively high value of $D(V)^{ap/bt}$ measured in the Mascota minette sample is likely due to
 882 the enhanced stabilization of V^{5+} due to the alkaline melt composition, which outweighs the shift
 883 towards the less oxidized species due to the increased temperature, as described previously. This
 884 illustrates the intricate interplay between the intensive parameters controlling the speciation of
 885 vanadium and its partitioning between the igneous species.

886 **6.0 Geological implications**

887 **6.1. Preliminary formulation of an apatite-biotite oxybarometer**

888 Towards quantifying the redox control on vanadium partitioning between apatite and biotite,
 889 and its use in oxygen barometry, we present a preliminary partitioning model that takes into
 890 account the change in proportion of the vanadium species with fO_2 , with estimates of the
 891 partitioning of the endmember vanadium species.

892 The relevant model parameters are identified by first considering the relation describing the
 893 individual apatite-melt and biotite-melt partition coefficients ($D(V)^{bt,ap/melt}$), expressed as:

$$894 \quad D(V)^{ap, bt/melt} = \{C(V^{3+})^{bt, ap} + C(V^{4+})^{bt, ap} + C(V^{5+})^{bt, ap}\} / \{C(V^{3+})^{melt} + C(V^{4+})^{melt} + C(V^{5+})^{melt}\} \quad (6)$$

895 In which $C(V^{x+})^{bt, ap}$ and $C(V^{x+})^{melt}$ are the concentrations of the vanadium species in apatite or biotite,
 896 and melt, respectively. The contribution from V^{2+} is assumed to be insignificant under the relatively
 897 oxidized conditions of the sample suites considered (Sutton et al., 2005). For each vanadium
 898 species, the individual mineral/melt partition coefficients can be expressed as:

$$899 \quad D(V^{x+})^{ap, bt/melt} = C(V^{x+})^{ap, bt} / C(V^{x+})^{melt} \quad (7)$$

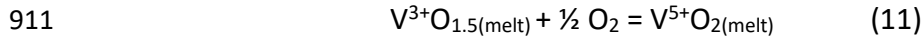
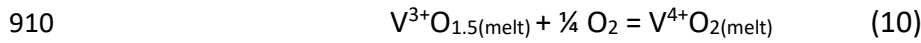
900 Which can be substituted into equation 6 to remove the apatite or biotite compositional terms to
 901 yield:

902 $D(V)^{ap, bt/melt} = \{ D(V^{3+})^{ap, bt/melt} C(V^{3+})^{melt} + D(V^{4+})^{ap, bt/melt} C(V^{4+})^{melt} + D(V^{5+})^{ap, bt/melt} C(V^{5+})^{melt} \} /$
 903 $\{ C(V)^{total, melt} \}$ (8)

904 In which $C(V)^{total, melt}$ is the sum of the contributions of each vanadium species to the total
 905 concentration in the melt. Considering just apatite/biotite partitioning ($D(V)^{ap/bt}$) yields the relation:

906 $D(V)^{ap/bt} = \{ D(V^{3+})^{ap/melt} C(V^{3+})^{melt} + D(V^{4+})^{ap/melt} C(V^{4+})^{melt} + D(V^{5+})^{ap/melt} C(V^{5+})^{melt} \} / \{ \{ D(V^{3+})^{bt/melt}$
 907 $C(V^{3+})^{melt} + D(V^{4+})^{bt/melt} C(V^{4+})^{melt} + D(V^{5+})^{bt/melt} C(V^{5+})^{melt} \} \}$ (9)

908 In terms of the speciation of vanadium, the relative proportions are governed by the homogenous
 909 redox equilibria:



912 Assuming ideal solution behavior of the vanadium species (the activity of V^{x+} is therefore equal to
 913 the mole fraction, $X_{V^{x+}}$), the corresponding equilibrium constants, $K(10)_{eq}$ and $K(11)_{eq}$ are:

914 $K(6)_{eq} = X_{V^{4+}O_2(melt)} / \{ X_{V^{3+}O_{1.5(melt)}} * fO_2^{1/4} \}$ (12)

915 $K(7)_{eq} = X_{V^{5+}O_2(melt)} / \{ X_{V^{3+}O_{1.5(melt)}} * fO_2^{1/2} \}$ (13)

916 The abundance of vanadium species at a given fO_2 is determined using values of $K(6)_{eq}$ and $K(7)_{eq}$
 917 estimated by Sossi et al. (2018) for a granitic composition measured from experiments done at 0.5
 918 GPa and 800°C using magnetite-melt partitioning systematics. Estimates of $D^{ap/bt}$ for the
 919 endmember vanadium species were chosen from similar, homovalent “surrogate” trace elements,
 920 i.e., Ga (IR = 0.062 nm) for V^{3+} and Ti (IR = 0.060 nm) for V^{4+} . For $D(V^{5+})^{ap/bt}$, however, no suitable
 921 “surrogate” homovalent elements are available as both Nb and Ta have almost 2x larger ionic radii
 922 in comparison to V^{5+} , therefore the value of $D(V^{5+})^{ap/bt}$ was determined by least squares
 923 minimization to match the modeled $D(\Sigma V)^{ap/bt}$ values to the measured ones. Estimates for the
 924 endmember $D(V^{x+})$ are provided in Table 6. The value for $D(V^{5+})^{ap/bt}$ of 0.165 regressed from the data
 925 is consistent with the lattice strain-based $D^{ap/bt}$ systematics for other pentavalent elements – P^{5+} (IR
 926 = 0.017 nm) and identically-sized Ta^{5+} and Nb^{5+} (IR=0.064 nm). Assuming $D(P)^{ap/bt}$ as the upper D
 927 limit (element strongly concentrated in apatite) and $D(Ta)^{ap/bt}$ as the lower limit (element strongly

928 concentrated in biotite), the modeled $D(V^{5+})^{ap/bt}$ value falls within the expected D interval, describing
929 a lesser compatibility in apatite and a moderate compatibility with biotite.

930 The apatite/biotite vanadium partitioning systematics were subsequently calculated using
931 equations 9, 12 and 13 and a comparison of the calculated and measured partitioning is provided in
932 Figure 14a. As can be seen, with the exception of the Mascota minette sample, the model provides
933 a very good description of the data for the suites with similar, peraluminous compositions, capturing
934 values within analytical uncertainty. Results of this modelling indicate that the high compatibility of
935 V^{3+} and V^{4+} in biotite and their low compatibility in apatite leads to V^{5+} as being the most important
936 species, as its abundance and $D^{ap/bt}$ almost entirely determines the total $D(V)^{ap/bt}$. The model,
937 although preliminary, therefore provides a first insight into the controls of vanadium intermineral
938 partitioning, and it seems clear that factors that affect the V^{5+} speciation and partitioning will
939 influence the accuracy of this method in oxybarometry. As mentioned in section 5.3, a number of
940 studies have already shown that aspects of melt composition, particularly the presence of network-
941 modifying cations, such as alkalis and alkaline earth elements, will affect the species proportions,
942 and hence vanadium partitioning, at a given fO_2 .

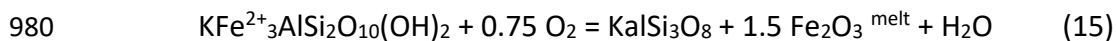
943 **6.2 Example of application to natural apatite and biotite-bearing samples**

944 Currently, the most precise oxybarometry methods are based on the equilibrium between
945 coexisting Fe-Ti oxides (Andersen & Lindsley, 1988; Carmichael, 1967; Ghiorso & Evans, 2008; Spencer &
946 Lindsley, 1981) with other methods formulated from the mineral/melt partitioning of heterovalent
947 elements (Arató & Audétat, 2017c; Burnham et al., 2015; Smythe & Brenan, 2016). Despite the
948 widespread application of these approaches, oxybarometry of plutonic igneous systems, or those
949 lacking one or both Fe-Ti-oxides, remains a challenge. Although a comprehensive application of
950 apatite-biotite oxygen barometry awaits additional experimental calibration, and the more
951 widespread availability of vanadium concentration data for apatite, we present here two examples
952 of how the method could be applied to rock suites for which direct fO_2 determinations are
953 unavailable.

954 The chosen suites represent samples provided from our own research collection for which
955 coexisting apatite and biotite were measured using the identical analytical protocols as described

956 in section 3.2. The suites comprise samples from the peraluminous South Mountain Batholith
957 (SMB), Nova Scotia, Canada (Brenan et al., 2023) and the Palabora carbonatite, South Africa (Dixon,
958 1979). Petrographic relations indicate that samples from both suites were saturated in only a single
959 Fe-Ti oxide phase during crystallization (ilmenite in SMB and magnetite in Palabora). Importantly for
960 comparative purposes, each has other petrological indications of the prevailing redox conditions.
961 Both samples from the SMB and Palabora carbonatite contain petrographic evidence for co-
962 saturation in apatite and biotite as reflected by ubiquitous biotite-hosted apatite inclusions (Figure
963 15). Biotite crystallization temperatures for the SMB are estimated to be in the range of 603-722°C
964 (Brenan et al., 2023), so temperatures and melt compositions are similar to the natural calibration
965 dataset. Temperatures for Palabora reported by Solovova et al. (1998) indicate apatite crystallized
966 at 720-750 °C, overlapping the results of olivine-magnetite thermometry (510-760 °C) reported by
967 Braunger et al. (2020). Although crystallization temperatures are similar to the natural calibration
968 suite, the host carbonatite melt composition is silica-poor and significantly richer in network
969 modifying cations.

970 The vanadium content of apatite and biotite from 20 samples encompassing 9 constituent
971 plutons of the SMB and one sample from the Palabora transgressive carbonatite facies are reported
972 in Supplementary Table ST4 and ST5. Values of $D(V)^{ap/bt}$ were calculated from coexisting pairs from
973 each sample, and the mean and standard deviation of values are compared to the preliminary
974 partitioning model in Figure 14b. For the SMB, the range in $D(V)^{ap/bt}$ is 0.0008 to 0.0190 and
975 suggests biotite-apatite equilibration under generally reducing conditions, with the mean $D(V)^{ap/bt}$ of
976 0.0052 corresponding to ~FMQ-1.5. As far as other fO_2 estimates for the SMB, previous
977 experimental studies (summarized in Bucholz et al., 2018) have shown that, at a given temperature,
978 biotite $Fe/(Fe+Mg)$ increases with decreasing fO_2 , consistent with a shift to the left of the
979 heterogeneous redox equilibrium:



981 Applying this equilibrium to the multicomponent natural system, Brenan et al. (2023) used the
982 MELTS thermodynamic model to track biotite compositional evolution in SMB samples as a function
983 of fO_2 , with results indicating biotite crystallization within a narrow fO_2 interval of FMQ to FMQ-1.

984 Also consistent with this indication of generally reduced conditions are previous fO_2 estimates for
985 the SMB based on Ce-in-zircon oxygen barometry yielding FMQ to FMQ-5 (Bickerton et al., 2022).

986 The mean $D(V)^{ap/bt}$ from the carbonatite sample of $0.186 (\pm 0.046)$ indicates a higher
987 abundance of highly charged vanadium in the melt compared to the SMB, suggestive of more
988 oxidizing conditions. However, the measured $D(V)^{ap/bt}$ exceeds the model curve. Assuming that the
989 measured $D(V)^{ap/bt}$ represents equilibrium, then the unusually high value for $D(V)^{ap/bt}$ may be
990 influenced by other factors besides fO_2 . As discussed in section 5.3, several previous studies have
991 shown that melt composition may affect the vanadium speciation, with a higher proportion of
992 oxidized species stabilized in less polymerized melts containing greater abundances of network
993 modifying cations (McKeown et al., 2011; Wang et al., 2016 and references therein). The same
994 interpretation is applied to explain the elevated $D(V)^{ap/bt}$ for the Mascota minette sample.
995 Carbonate melts represent an extreme endmember in terms of structure and composition, with
996 very low SiO_2 , high alkali and alkaline earth element concentrations, and a largely ionic liquid
997 structure (Jones et al., 2013). The extent to which the speciation determinations from silicate melt
998 based studies can be used to interpret partitioning involving carbonate melt is uncertain. However,
999 Jones et al. (1995) report the results of silicate melt-carbonate melt partitioning experiments which
1000 may offer some insights. Their experiments done at $1250^\circ C$ and 1 GPa reveal a simple linear
1001 decrease $\ln D^{silicate/carbonate}$ with increasing Z/r , in which Z is the ionic charge and r the ionic radius (in
1002 angstroms). Results revealed two groupings, however, divided according to $Z/r < \text{or} > 7$, with higher
1003 $D^{silicate/carbonate}$ for $Z/r > 7$, therefore indicating that the V^{5+} species ($Z/r = 9.2$) would be more strongly
1004 partitioned into the carbonate relative to the V^{3+} or V^{4+} species (Z/r of 4.7 and 6.9, respectively).
1005 Thus, there is some evidence, albeit indirect, that the more highly charged V^{5+} species may be
1006 preferentially stabilized in carbonate melt, relative to the more reduced species, thus accounting for
1007 the anomalously high values of $D^{ap/bt}$ measured for the Palabora sample. In addition to melt
1008 structure, biotite composition could also play a role, in that the Palabora biotite is Al- and Ti-poor
1009 compared to the reference group (Supplementary Table 2), which could hinder the uptake of V^{3+}
1010 and V^{4+} and amplify the melt composition-induced shift towards a higher $D(V)^{ap/bt}$ value. Despite
1011 the likely complications imposed by other factors, the relatively oxidized conditions for the Palabora
1012 sample implied by the high value of $D(V)^{ap/bt}$ are broadly consistent with some independent

1013 measures of sample redox state. For example, the only primary Fe oxide mineral in the sample is
1014 magnetite, which together with coexisting tetraferriphlogopite, implies a moderately high fO_2
1015 (Giebel et al., 2019). Also, using the composition of ilmenite exsolved from host magnetite, Milani et
1016 al. (2017) tracked a T- fO_2 path of re-equilibration with maximum temperatures at 560-590 °C, and
1017 fO_2 of $\sim FMQ+1$. This agrees with measurements reported by Braunger et al. (2020), using a similar
1018 method which suggesting an fO_2 of $\sim FMQ+0.9 (\pm 0.4)$ at T=570-650 °C.

1019 5. Conclusions

1020 Results reported in this study show that the partitioning of vanadium and other heterovalent
1021 elements (As, Eu, Mo, Sn, W) between apatite, biotite and high silica glass show changes with
1022 sample redox state. With increasing fO_2 from FMQ-2.8 to FMQ+2.8, vanadium becomes more
1023 compatible in apatite, ($D(V)^{ap/gl}$ from ~ 0.6 to ~ 5), and less compatible in biotite, ($D(V)^{bt/gl}$ from ~ 580
1024 to ~ 50). Over the same fO_2 interval, tin compatibility increases in both minerals ($D(Sn)^{ap/gl}$ from 0.05-
1025 0.3, $D(Sn)^{bt/gl}$ from 0.1-1), europium compatibility increases in apatite ($D(Eu)^{ap/gl}$ from ~ 20 - ~ 90), and
1026 tungsten compatibility decreases in biotite ($D(W)^{bt/gl}$ from ~ 0.13 to ~ 0.02). Given the diverging fO_2
1027 trends for $D(V)^{bt/gl}$ and $D(V)^{ap/gl}$, the vanadium partitioning between apatite and biotite is amplified
1028 from values of ~ 0.003 at FMQ-2.8 to ~ 0.5 at FMQ+4.3. Comparison of partitioning for an internally
1029 consistent dataset of homovalent elements also collected in this study suggests that the changes in
1030 partitioning behaviour of the heterovalent elements are primarily controlled by the fO_2 . Based on
1031 these results, a preliminary model of $D(V)^{ap/bt}$ applicable to high-silica, peraluminous systems is
1032 developed. The model reveals that the species abundance and $D^{ap/bt}$ of V^{5+} almost entirely
1033 determines the total $D(V)^{ap/bt}$. Vanadium intermineral partitioning in the peraluminous South
1034 Mountain Batholith (SMB) implies reducing conditions ($\sim FMQ-1.5$) consistent with fO_2
1035 determinations from independent phase-equilibria-based models and zircon-melt partitioning. The
1036 elevated $D(V)^{ap/bt}$ values measured for the Palabora carbonatite indicate a high proportion of V^{5+}
1037 during crystallization, which in part could reflect more oxidizing conditions, but also be influenced
1038 by melt and/or mineral composition controls. Further experimental studies of vanadium
1039 partitioning between apatite and biotite are necessary to quantify these effects.

1040 Previous experimental studies of mineral-melt partitioning relations involving
1041 ferromagnesian phases (pyroxene, olivine, Fe-Ti oxides; Arató & Audétat, 2017a; Mallmann & O'Neill,

1042 2009, 2013)) for vanadium have established that $D(V)$ decreases with increasing fO_2 , owing to the
1043 increasingly poor mismatch between the higher valence vanadium species and the dominant
1044 substituent cations in these phases. Because of this sympathetic partitioning relationship,
1045 intermineral partitioning of vanadium involving these phases shows little change with fO_2 . Minerals
1046 that exhibit exceptions to this behavior are rutile (Holycross & Cottrell, 2020, 2022) and apatite (this
1047 study), in which the V^{5+} species is the most compatible. Although the distribution of rutile is
1048 somewhat more restricted to specific igneous bulk compositions, apatite is a ubiquitous phase in
1049 compositions ranging from lunar basalts to high silica rhyolites (McCubbin & Jones, 2015; Webster &
1050 Piccoli, 2015). Hence, the change in apatite/biotite partitioning of vanadium documented in this
1051 study is almost certainly to be seen for the cases of apatite in equilibrium with pyroxenes, olivine
1052 and Fe-Ti oxides, providing the basis for a number of potentially new oxybarometers applicable to a
1053 range of rock-types.

1054 **Acknowledgements**

1055 The authors acknowledge research funding provided by the Natural Resources Canada
1056 Targeted Geoscience Initiative and the NSERC Discovery Grant program. Student support was
1057 provided to Rozenbaks through a Doctoral Award from the Department of Earth and Environmental
1058 Sciences at Dalhousie University and a Nova Scotia Graduate Scholarship. Drs Ray Donelick, Craig
1059 Chesner, Hamish Sandeman, John Hanchar, Jacob Hanley, and the Smithsonian Institution are
1060 thanked for providing rock samples analysed in this study. Ms. Natasha Drage, Drs Yanan Liu, Xiang
1061 Yang, Brandon Boucher and Bryan Maciag are thanked for their support in the SEM, EPMA, and LA-
1062 ICP-MS analyses.

1063

1064 **List of figures**

1065 **Figure 1.** Sample localities and oxidation of the analysed rock suites.

1066 **Figure 2.** Backscattered electron (BSE) images of biotite occurrences in the investigated rock suites.
1067 A) Fish Canyon tuff showing chemically uniform biotite with typical bent and broken textures. B)
1068 MAC137 is a biotite microphenocryst-rich sample of the glassy, flow-banded Revancha dike facies
1069 showing both zoned and “spongy-textured” generation of biotite in apparent disequilibrium (biotite
1070 on left side) along with relatively unzoned, euhedral biotites (e.g., crystal with bt02, bt03 labels and
1071 laser ablation analysis scars). C) MAC2 is a sample of the crystal-poor facies of the Revancha dike
1072 glassy chill margin, however, the biotite shows a similar textural distinction between the older and
1073 younger biotite generations. D) Apatite occurrences in Revancha dyke (MAC137) – subhedral,
1074 inclusion-rich apatite (on the right) and euhedral, inclusion-poorer apatite (on the left). E) Biotite
1075 and apatite occurrences in Cerro Esquinani stock (MAC160): euhedral and subhedral biotite, apatite
1076 phenocryst with a partially resorbed core and a biotite-hosted apatite inclusion. F) Mascota minette
1077 euhedral and subhedral biotite with laser ablation scars and acicular apatite set in a microcrystalline
1078 matrix. G) Occurrences of subhedral and euhedral apatite in Mascota minette. H) Large euhedral
1079 biotite phenocryst in Tuk-Tuk tuff (TT). I) Apatite occurrences in Tuk-Tuk tuff (TT7) as subhedral
1080 crystals set in vitreous matrix and hosted in a bent biotite crystal. J) Unzoned subhedral and
1081 euhedral biotite occurrences in TT7. K) Biotite flake, extracted from Umiakovik granite, contains
1082 apatite, ilmenite, and zircon inclusions. L) Zoned apatite in heavy mineral separate from UP. Mineral
1083 abbreviations from (Whitney & Evans, 2010).

1084 **Figure 3 .** Aluminium saturation and alkalinity of the analysed rock suites and glasses. Sources of the
1085 whole rock compositional data provided in Table 1.

1086 **Figure 4.** Biotite major element composition: proportions of tetrahedral Al (a), Ti (b), Mn (c), Na (d),
1087 Cl (e), F (f) as a function of Fe/(Fe+Mg) in biotite from the glassy volcanic suites from which empirical
1088 partitioning data were obtained. All values are calculated on the basis of 22 oxygen equivalents. The
1089 field of peraluminous and metaluminous granites is taken from data compiled by Gion et al. (2022).
1090 Field of lamprophyres taken from compilation by Saha et al. (2021).

1091 **Figure 5.** Anion and rare earth element composition of apatite. a) Occupancy of the apatite anionic
1092 site. OH abundance calculated assuming 2 anions per formula unit and subtracting the measured F
1093 and Cl abundances. Symbols from Fig. 4. b) Mean chondrite-normalized REE composition of the
1094 apatites. Error bars represent 1 SD of the apatite populations selected for D value calculations.

1095 **Figure 6.** Trace element concentration in the analyzed matrix glasses normalized to the average
1096 upper crust (Rudnick & Gao, 2003). Symbols from the Figure 4.

1097 **Figure 7.** Summary of mineral/melt partitioning coefficients determined in this study compared to
1098 other studies of natural and experimental systems. a) Ap/gl partitioning coefficients determined in
1099 this study in comparison to the results of experimental studies (PK 2006 – Prowatke & Klemme (2006),
1100 WG 1981 – Watson & Green (1981), JD 2004 - Ji & Dygert (2024), Letal 2023 – Li et al. (2023). b) Bt/gl

1101 partitioning coefficients (For comparison, studies in natural systems: FCT - Bachmann et al. (2005),
1102 AV – Acosta-Vigil et al. (2012), Petal 2024 – Pichavant et al. (2024). Experimental studies: Getal 2018
1103 – Gion et al. (2018), W&K, 2021 – Were & Keppler (2021), Petal 2016 - - Pichavant et al. (2016)).

1104 **Figure 8.** Mineral/melt chemical equilibria in the glass-phyric suites analyzed in this study. **A)**
1105 Biotite-glass Mg-Fe equilibrium. Gray lines represent the K_D for Mg-Fe exchange between biotite and
1106 melt established by Were and Keppler (2021), mean value marked as a solid line, dashed lines mark
1107 the maximal and minimal $K_D(\text{Fe-Mg})$ values. Black dashed lines mark the range of $K_D(\text{Fe-Mg})$ values
1108 determined by Icenhower & London (1997). Equilibrium in Were & Keppler experiments was
1109 approached by a prolonged duration of the experiments (30-45 days) and was confirmed using
1110 textural evidence and chemical uniformity of the phenocrysts and matrix glass. **B)** Apatite/glass
1111 partition coefficient of strontium ($D(\text{Sr})^{\text{ap/gl}}$) as a function of glass CaO. Experimental data from
1112 Prowatke & Klemme (2006) and Watson & Green (1981). Prowatke and Klemme suggested trend of $D(\text{Sr})$
1113 in the mafic compositions in a correlation with the melt CaO. Data in this study lay near the
1114 minimum CaO with high $D(\text{Sr})$ values suggesting a continuation from the felsic Watson & Green
1115 compositions.

1116 **Figure 9.** Major and trace element $D^{\text{ap/gl}}$ values as a function of ionic radius in VIII-fold coordination.
1117 Curves are produced as least square regressions to Eq. 4 for Na, K, Rb in monovalent array, Zn, Mg,
1118 Fe, Ca, Sr, Ba in divalent array, REE and Y in trivalent array, Hf, Zr, Th in tetravalent array.
1119 Pentavalent elements (P, Nb, Ta) lack sufficient datapoints to model the r_i - D_i relationships. When
1120 selecting the D values for the isovalent array fits, several elements were excluded from the
1121 regression (Li for monovalent, Ga for trivalent, Si, Ti, Ge for tetravalent array) as their IR are
1122 sufficiently small to enter the tetrahedral site, thus reducing the IR. Similarly, the heterovalent
1123 elements (V, W, U) are not included in the fitting. Symbols from Fig. 4. Error bars depict uncertainty
1124 of D, propagated from standard errors of element concentrations in apatite and glass.

1125 **Figure 10.** Major and trace element $D^{\text{bt/gl}}$ values as a function of ionic radii. Curves are produced as
1126 least square regressions to Eq. 4. for Na, K, Cs in XII-fold coordinated monovalent array, Mg, Co, Fe,
1127 Mn in VI-fold coordinated divalent array, Si, Ge, Hf, Zr in IV-fold coordinated tetravalent array. In the
1128 Al^{VI} -rich Macusani biotite, it is assumed that the trivalent trace elements (Ga, In, Sc, Lu, Yb, Y)
1129 exclusively enter the octahedral sites, whereas in the less-aluminous biotites of FCT and TT the two
1130 smallest trivalent trace elements (Ga, In) enter the tetrahedral site and the other, larger trivalent
1131 ions enter the octahedral site. Symbols from Fig. 4. Error bars depict uncertainty of D, propagated
1132 from standard deviations of element concentrations in biotite and glass.

1133 **Figure 11.** Comparison of empirical and experimental ap/gl partition coefficients for samarium as a
1134 function of the SiO_2 content of the coexisting melt demonstrating the large increase in partition
1135 coefficients with increasing SiO_2 . Experimental data from Prowatke and Klemme (2006; P&K) and
1136 Watson and Green (1981; W&G); Empirical data from Brophy et al (2011; B et al), Li et al. (2023) and
1137 this study.

1138 **Figure 12.** Redox sensitive heterovalent element partitioning between biotite and melt (a), apatite
1139 and melt (b), apatite and biotite (c). Error bars depict the reported range of fO_2 and D uncertainty
1140 propagated from standard errors of the element concentrations.

1141 **Figure 13.** Homovalent element apatite/biotite partitioning coefficients as a function of oxygen
1142 fugacity (a) and inverse temperature (b). Sample group for $D^{ap/bt}-1/T$ correlation includes all
1143 samples, the $D_{ap/bt}-fO_2$ correlation is based on all samples except Mascota minette.

1144 **Figure 14.** a) Model of the $D(\Sigma V)^{apatite/biotite}$ as a function of oxygen fugacity. Inputs: surrogate $D(V^{3+})$
1145 = $D(Ga)$, $D(V^{4+}) = D(Ti)$, $D(V^{5+}) =$ approximation from $D(Nb)$ and $D(Ta)$ given in the legend,
1146 abundances of V species from Sossi et al. (2018). High-T model is based on the surrogate
1147 homovalent element D values in Mascota minette, low-T model is based on the rest of the sample
1148 group. b) Variation of $D(\Sigma V)^{apatite/biotite}$ in South Mountain Batholith (purple) and Palabora
1149 carbonatite (green). Vanadium partitioning between apatite and biotite suggests fO_2 below FMQ in
1150 South Mountain Batholith whereas the D values in the Palabora carbonatite correspond with
1151 stronger oxidation.

1152 **Figure 15.** Backscattered electron images showing the textural relations for biotite and apatite
1153 indicating co-crystallization of both phases. A) Palabora carbonatite (xxx facies) and B) peraluminous
1154 South Mountain Batholith (sample BM0001, Cloud Lake Pluton)

- 1155 **List of tables**
- 1156 **Table 1.** Summary of the analysed samples.
- 1157 **Table 2.** Microanalytical conditions of EPMA and LA-ICP-MS used in this study.
- 1158 **Table 3.** Ap/gl D values
- 1159 **Table 4.** Bt/gl D values
- 1160 **Table 5.** Apatite/biotite D values
- 1161 **Table 6.** Vanadium intermineral partitioning coefficient values used in the model.

1162 **References**

- 1163 Acosta-Vigil, A., Buick, I., Cesare, B., London, D., & Morgan, G. B. (2012). The extent of equilibration between
1164 melt and residuum during regional anatexis and its implications for differentiation of the continental
1165 crust: A study of partially melted metapelitic enclaves. *Journal of Petrology*, 53(7), 1319–1356.
- 1166 Andersen, D. J., & Lindsley, D. H. (1988). Internally consistent solution models for Fe-Mg-Mn-Ti oxides: Fe-Ti
1167 oxides. *American Mineralogist*, 7(3), 714–726.
- 1168 Arató, R., & Audétat, A. (2017a). Experimental calibration of a new oxybarometer for silicic magmas based on
1169 vanadium partitioning between magnetite and silicate melt. *Geochimica et Cosmochimica Acta*, 209,
1170 284–295.
- 1171 Arató, R., & Audétat, A. (2017b). FeTiMM - A new oxybarometer for mafic to felsic magmas. *Geochemical
1172 Perspectives Letters*, 5, 19–23.
- 1173 Arató, R., & Audétat, A. (2017c). Vanadium magnetite–melt oxybarometry of natural, silicic magmas: a
1174 comparison of various oxybarometers and thermometers. *Contributions to Mineralogy and Petrology*,
1175 172(7).
- 1176 Arevalo, R., & McDonough, W. F. (2008). Tungsten geochemistry and implications for understanding the
1177 Earth's interior. *Earth and Planetary Science Letters*, 272(3–4), 656–665.
1178 <https://doi.org/10.1016/j.epsl.2008.05.031>
- 1179 Bachmann, O., Dungan, M. A., & Bussy, F. (2005). Insights into shallow magmatic processes in large silicic
1180 magma bodies: the trace element record in the Fish Canyon magma body, Colorado. *Contributions to
1181 Mineralogy and Petrology*, 149(3), 338–349.
- 1182 Bachmann, O., Oberli, F., Dungan, M. A., Meier, M., Mundil, R., & Fischer, H. (2007). ⁴⁰Ar/³⁹Ar and U-Pb
1183 dating of the Fish Canyon magmatic system, San Juan Volcanic field, Colorado: Evidence for an extended
1184 crystallization history. *Chemical Geology*, 236(1–2), 134–166.
- 1185 Bailey, S. W. (1984). Classification and structures of the micas. In S. W. Bailey (Ed.), *Micas. Reviews in
1186 Mineralogy* (1st Edition, Vol. 13).
- 1187 Ballhaus, C., Berry, R. F., & Green, D. H. (1991). High-pressure experimental calibration of the olivine-
1188 orthopyroxene-spinel oxygen geobarometer: implications for the oxidation state of the upper mantle.
1189 *Contributions to Mineralogy and Petrology*, 107, 27–40.
- 1190 Ballouard, C., Massuyeau, M., Elburg, M. A., Tappe, S., Viljoen, F., & Brandenburg, J. T. (2020). The magmatic
1191 and magmatic-hydrothermal evolution of felsic igneous rocks as seen through Nb-Ta geochemical
1192 fractionation, with implications for the origins of rare-metal mineralizations. *Earth-Science Reviews*, 203.
- 1193 Beattie, P. (1994). Systematics and energetics of trace-element partitioning between olivine and silicate
1194 melts: Implications for the nature of mineral/melt partitioning. *Chemical Geology*, 117, 57–71.
- 1195 Belousova, E. A., Walters, S., Griffin, W. L., & O'Reilly, S. Y. (2001). Trace-element signatures of apatites in
1196 granitoids from the Mt Isa Inlier, Northwestern Queensland. *Australian Journal of Earth Sciences*, 48(4),
1197 603–619.

- 1198 Berg, J. H. (1977). Regional Geobarometry in the Contact Aureoles of the Anorthositic Nain Complex,
1199 Labrador. *Journal of Petrology*, *18*, 399–430.
- 1200 Berg, J. H. (1979). Physical Constraints and tectonic setting of the Nain complex. *Geological Association of*
1201 *Canada - Mineralogical Association of Canada Annual Meeting Abstracts*, *4*, 39.
- 1202 Berry, A. J., O'Neill, H. S. C., Scott, D. R., Foran, G. J., & Shelley, J. M. G. (2006). The effect of composition on
1203 Cr²⁺/Cr³⁺ in silicate melts. *American Mineralogist*, *91*(11–12), 1901–1908.
1204 <https://doi.org/10.2138/am.2006.2097>
- 1205 Bindeman, I. N., & Davis, A. M. (2000). Trace element partitioning between plagioclase and melt:
1206 Investigation of dopant influence on partition behavior. *Geochimica et Cosmochimica Acta*, *64*, 2863–
1207 2878.
- 1208 Blundy, J., & Wood, B. (1994). Prediction of crystal-melt partition coefficients from elastic moduli. *Nature*,
1209 *372*, 452–454.
- 1210 Borisov, A., & Aranovich, L. (2020). Rutile solubility and TiO₂ activity in silicate melts: An experimental study.
1211 *Chemical Geology*, *556*.
- 1212 Braunger, S., Marks, M. A. W., Wenzel, T., Chmyz, L., Guitarrari Azzone, R., & Markl, G. (2020). Do
1213 carbonatites and alkaline rocks reflect variable redox conditions in their upper mantle source? *Earth and*
1214 *Planetary Science Letters*, *533*.
- 1215 Brice, J. C. (1975). Some thermodynamic aspects of the growth of strained crystals. *Journal of Crystal Growth*,
1216 *28*, 249–253.
- 1217 Burnham, A. D., Berry, A. J., Halse, H. R., Schofield, P. F., Cibin, G., & Mosselmans, J. F. W. (2015). The
1218 oxidation state of europium in silicate melts as a function of oxygen fugacity, composition and
1219 temperature. *Chemical Geology*, *411*, 248–259.
- 1220 Canil, D. (1999). Vanadium partitioning between orthopyroxene, spinel and silicate melt and the redox states
1221 of mantle source regions for primary magmas. *Geochimica et Cosmochimica Acta*, *63*(3/4), 557–572.
- 1222 Carmichael, I. S. E. (1967). The Iron-Titanium Oxides of Salic Volcanic Rocks and their Associated
1223 Ferromagnesian Silicates. *Contributions to Mineralogy and Petrology*, *14*, 36–64.
- 1224 Carmichael, I. S. E., & Ghiorso, M. S. (1990). The Effect of Oxygen Fugacity on the Redox State of Natural
1225 Liquids and Their Crystallizing Phases. *Reviews in Mineralogy and Geochemistry*, *24*, 191–212.
- 1226 Carmichael, I. S. E., Lange, R. A., & Luhr, J. F. (1996). Quaternary minettes and associated volcanic rocks of
1227 Mascota, western Mexico: a consequence of plate extension above a subduction modified mantle
1228 wedge. *Contributions to Mineralogy and Petrology*, *124*, 302–333.
- 1229 Chesner, C. A. (1998). Petrogenesis of the Toba Tuffs, Sumatra, Indonesia. *Journal of Petrology*, *39*(3), 397–
1230 438.
- 1231 Chesner, C. A. (2012). The Toba Caldera Complex. *Quaternary International*, *258*, 5–18.
- 1232 Chesner, C. A., Barbee, O. A., & McIntosh, W. C. (2020). The enigmatic origin and emplacement of the
1233 Samosir Island lava domes, Toba Caldera, Sumatra, Indonesia. *Bulletin of Volcanology*, *82*(3).

- 1234 Cicconi, M. R., Giuli, G., Ertel-Ingrisch, W., Paris, E., & Dingwell, D. B. (2015). The effect of the [Na/(Na+K)]
1235 ratio on Fe speciation in phonolitic glasses. *American Mineralogist*, *100*(7), 1610–1619.
- 1236 Cicconi, M. R., Le Losq, C., Moretti, R., Neuville, D. R., & Magmas, D. R. N. (2020). the Largest Repositories and
1237 Carriers of Earth's Redox Processes. *Elements*, *16*(3), 173–178.
- 1238 Clark, A. H., Farrar, E., Kontak, D. J., Langridge, R. J., Arenas F., M. J., France, L. J., McBride, S. L., Woodman, P.
1239 L., Wasteneys, H. A., Sandeman, H. A., & Archibald, D. A. (1990). Geologic and geochronologic
1240 constraints on the metallogenic evolution of the Andes of southeastern Peru. *Economic Geology*, *85*(7),
1241 1520–1583.
- 1242 Clarke, D. B., Renno, A. D., Hamilton, D. C., Gilbricht, S., & Bachmann, K. (2021). The spatial association of
1243 accessory minerals with biotite in granitic rocks from the South Mountain Batholith, Nova Scotia,
1244 Canada. *Geosphere*, *18*(1), 1–18.
- 1245 Clarke, R. S., & Altschuler, Z. S. (1958). Determination of the oxidation state of uranium in apatite and
1246 phosphorite deposits. *Geochimica et Cosmochimica Acta*, *13*, 127–141.
- 1247 Corfu, F., Hanchar, J. M., Hoskin, P. W. O., & Kinny, P. (2003). Atlas of Zircon Textures. *Reviews in Mineralogy
1248 and Geochemistry*, *53*, 469–500.
- 1249 Cottrell, E., Birner, S. K., Brounce, M., Davis, F. A., Waters, L. E., & Kelley, K. A. (2021). Oxygen Fugacity Across
1250 Tectonic Settings. In *Magma Redox Geochemistry* (pp. 33–61).
- 1251 Dailey, S. R., Christiansen, E. H., Dorais, M. J., Kowallis, B. J., Fernandez, D. P., & Johnson, D. M. (2018). Origin
1252 of the fluorine- and beryllium-rich rhyolites of the Spor Mountain Formation, Western Utah. *American
1253 Mineralogist*, *103*(8), 1228–1252. <https://doi.org/10.2138/am-2018-6256>
- 1254 Dingwell, D. B., & Virgo, D. (1987). The effect of oxidation state on the viscosity of melts in the system Na₂O-
1255 FeO-Fe₂O₃-SiO₂. *Geochimica et Cosmochimica Acta*, *51*, 195–205.
- 1256 Drake, M. (1975). The oxidation state of europium as an indicator of oxygen fugacity. *Geochimica and
1257 Cosmochimica Acta*, *39*, 55–64.
- 1258 Dymek, R. F. (1983). Titanium, aluminum and interlayer cation substitutions in biotite from high-grade
1259 gneisses, West Greenland. *American Mineralogist*, *6*, 880–399.
- 1260 Elliott, J. C. (1994). Fluorapatite and Chlorapatite. In *Studies in Inorganic Chemistry* (Vol. 18, Issue C, pp. 63–
1261 110).
- 1262 Emslie, R. F., & Loveridge, W. D. (1992). Fluorite-bearing Early and Middle Proterozoic granites, Okak Bay
1263 area, Labrador: Geochronology, geochemistry and petrogenesis. *Lithos*, *28*, 87–109.
- 1264 Emslie, R. F., & Stirling, J. A. R. (1993). Rapakivi and related granitoids of the Nain plutonic suite:
1265 geochemistry, mineral assemblages and fluid equilibria. *Canadian Mineralogist*, *31*(4), 821–847.
- 1266 Engel, G., Krieg, F., & Reif, G. (1975). Mischkristallbildung und Kationenordnung im System Bleihydroxylapatit-
1267 Calciumhydroxylapatit. *Journal of Solid State Chemistry*, *15*, 117–126.
- 1268 Ferry, J. M., & Watson, E. B. (2007). New thermodynamic models and revised calibrations for the Ti-in-zircon
1269 and Zr-in-rutile thermometers. *Contributions to Mineralogy and Petrology*, *154*(4), 429–437.

- 1270 Fincham, C. J. B., & Richardson, F. D. (1954). The behaviour of sulphur in silicate and aluminate melts.
1271 *Proceedings of the Royal Society of London. Series A. Mathematical and Physical Sciences*, 223, 40–62.
- 1272 Fonseca, R. O. C., Mallmann, G., Sprung, P., Sommer, J. E., Heuser, A., Speelmanns, I. M., & Blanchard, H.
1273 (2014). Redox controls on tungsten and uranium crystal/silicate melt partitioning and implications for
1274 the U/W and Th/W ratio of the lunar mantle. *Earth and Planetary Science Letters*, 404, 1–13.
- 1275 Frost, B. R. (1991). Introduction to Oxygen Fugacity and Its Petrologic Importance. In D. H. Lindsley (Ed.),
1276 *Oxide minerals: Petrologic and Magnetic Significance, Reviews in Mineralogy* (Vol. 25, pp. 1–10).
- 1277 Fuhrman, M. L., & Lindsley, D. H. (1988). Ternary-feldspar modeling and thermometry. *American*
1278 *Mineralogist*, 73, 201–215.
- 1279 Gaillard, F., Scaillet, B., Pichavant, M., & Iacono-Marziano, G. (2015). The redox geodynamics linking basalts
1280 and their mantle sources through space and time. *Chemical Geology*, 418, 217–233.
- 1281 Gao, M., Xiong, X., Huang, F., Wang, J., & Wei, C. (2023). Key Factors Controlling Biotite–Silicate Melt Nb and
1282 Ta Partitioning: Implications for Nb–Ta Enrichment and Fractionation in Granites. *Journal of Geophysical*
1283 *Research: Solid Earth*, 128(7).
- 1284 Giorso, M. S., & Evans, B. W. (2008). Thermodynamics of rhombohedral oxide solid solutions and a revision
1285 of the Fe–Ti two-oxide geothermometer and oxygen-barometer. *American Journal of Science*, 308, 957–
1286 1039.
- 1287 Giorso, M. S., & Sack, R. O. (1991). Fe–Ti oxide geothermometry: thermodynamic formulation and the
1288 estimation of intensive variables in silicic magmas. *Contributions to Mineralogy Petrology*, 108, 485–
1289 510.
- 1290 Giorso, M. S., & Sack, R. O. (1995). Chemical mass transfer in magmatic processes IV. A revised and
1291 internally consistent thermodynamic model for the interpolation and extrapolation of liquid–solid
1292 equilibria in magmatic systems at elevated temperatures and pressures. *Contributions to Mineralogy*
1293 *and Petrology*, 119, 197–212.
- 1294 Gion, A. M., Piccoli, P. M., & Candela, P. A. (2018). Partitioning of indium between ferromagnesian minerals
1295 and a silicate melt. *Chemical Geology*, 500, 30–45.
- 1296 Gion, A. M., Piccoli, P. M., & Candela, P. A. (2022). Characterization of biotite and amphibole compositions in
1297 granites. *Contributions to Mineralogy and Petrology*, 177(4).
- 1298 Gleadow, A., Harrison, M., Kohn, B., Lugo-Zazueta, R., & Phillips, D. (2015). The Fish Canyon Tuff: A new look
1299 at an old low-temperature thermochronology standard. *Earth and Planetary Science Letters*, 424, 95–
1300 108.
- 1301 Henry, D. J., Guidotti, C. V., & Thomson, J. A. (2005). The Ti-saturation surface for low-to-medium pressure
1302 metapelitic biotites: Implications for geothermometry and Ti-substitution mechanisms. *American*
1303 *Mineralogist*, 90(2–3), 316–328.
- 1304 Hensen, B. J., & Green, D. H. (1972). Experimental Study of the Stability of Cordierite and Garnet in Pelitic
1305 Compositions at High Pressures and Temperatures II. Compositions without Excess Alumino-Silicate.
1306 *Contributions to Mineralogy and Petrology*, 35, 331–354.

- 1307 Hensen, B. J., & Green, D. H. (1973). Experimental Study of the Stability of Cordierite and Garnet in Pelitic
1308 Compositions at High Pressures and Temperatures III. Synthesis of Experimental Data and Geological
1309 Applications. *Contributions to Mineralogy and Petrology*, 38, 151–166.
- 1310 Holycross, M., & Cottrell, E. (2020). Partitioning of V and 19 other trace elements between rutile and silicate
1311 melt as a function of oxygen fugacity and melt composition: Implications for subduction zones.
1312 *American Mineralogist*, 105(2), 244–254.
- 1313 Holycross, M., & Cottrell, E. (2022). Experimental quantification of vanadium partitioning between eclogitic
1314 minerals (garnet, clinopyroxene, rutile) and silicate melt as a function of temperature and oxygen
1315 fugacity. *Contributions to Mineralogy and Petrology*, 177(2).
- 1316 Holzheid, A., Borisov, A., & Palme, H. (1994). The effect of oxygen fugacity and temperature on solubilities of
1317 nickel, cobalt, and molybdenum in silicate melts. *Geochimica et Cosmochimica Acta*, 58(8).
- 1318 Icenhower, J., & London, D. (1995). An experimental study of element partitioning among biotite, muscovite,
1319 and coexisting peraluminous silicic melt at 200 MPa (H₂O). *American Mineralogist*, 80(11–12), 1229–
1320 1251. <https://doi.org/10.2138/am-1995-11-1213>
- 1321 Icenhower, J. P., & London, D. (1997). Partitioning of fluorine and chlorine between biotite and granitic melt:
1322 experimental calibration at 200 MPa H₂O. *Contributions to Mineralogy and Petrology*, 127, 17–29.
- 1323 Ji, D., & Dygert, N. (2024). Trace element partitioning between apatite and silicate melts: Effects of major
1324 element composition, temperature, and oxygen fugacity, and implications for the volatile element
1325 budget of the lunar magma ocean. *Geochimica et Cosmochimica Acta*, 369, 141–159.
- 1326 Jochum, K. P., Nohl, U., Herwig, K., Lammel, E., Stoll, B., & Hofmann, A. W. (2005). GeoReM: A New
1327 Geochemical Database for Reference Materials and Isotopic Standards. *Geostandards and Geoanalytical
1328 Research*, 29(3), 333–338.
- 1329 Johnson, M. C., & Rutherford, M. J. (1989). Experimentally Determined Conditions in the Fish Canyon Tuff,
1330 Colorado, Magma Chamber. *Journal of Petrology*, 30(3), 711–737.
- 1331 Jones, A. P., Genge, M., & Carmody, L. (2013). Carbonate melts and carbonatites. *Reviews in Mineralogy and
1332 Geochemistry*, 75, 289–322.
- 1333 Jones, J. H., Walker, D., Pickett, D. A., Murrell, M. T., & Beattie, P. (1995). Experimental investigations of the
1334 partitioning of Nb, Mo, Ba, Ce, Pb, Ra, Th, Pa, and U between immiscible carbonate and silicate liquids.
1335 *Geochimica et Cosmochimica Acta*, 59(7), 1307–1320.
- 1336 Klemme, S., & Dalpé, C. (2003). Trace-element partitioning between apatite and carbonatite melt. *American
1337 Mineralogist*, 88, 639–646.
- 1338 Kreidler, E. R., & Hummel, F. A. (1970). The crystal chemistry of apatite: structure fields of fluor- and
1339 chlorapatite. *The American Mineralogist*, 55, 170–184.
- 1340 Kress, V. C., & Carmichael, I. S. E. (1991). The compressibility of silicate liquids containing Fe₂O₃ and the
1341 effect of composition, temperature, oxygen fugacity and pressure on their redox states. *Contributions to
1342 Mineralogy and Petrology*, 108, 82–92.

- 1343 Lange, R. A., & Carmichael, I. S. E. (1990). Hydrous Basaltic Andesites Associated with Minette and Related
1344 Lavas in Western Mexico. *Journal of Petrology*, *31*, 1225–1259.
- 1345 Lange, R., & Carmichael, I. S. E. (1987). Densities of Na₂O-K₂O-CaO-MgO-FeO-Fe₂O₃-Al₂O₃-TiO₂-SiO₂ liquids:
1346 New measurements and derived partial molar properties. *Geochimica et Cosmochimica Acta*, *51*, 293–
1347 2946.
- 1348 LaTourrette, T., Hervig, R. L., & Holloway, J. R. (1995). Trace element partitioning between amphibole,
1349 phlogopite, and basanite melt. *Earth and Planetary Science Letters*, *135*, 13–30.
- 1350 Lee, C. T. A., Harbert, A., & Leeman, W. P. (2007). Extension of lattice strain theory to mineral/mineral rare-
1351 earth element partitioning: An approach for assessing disequilibrium and developing internally
1352 consistent partition coefficients between olivine, orthopyroxene, clinopyroxene and basaltic melt.
1353 *Geochimica et Cosmochimica Acta*, *71*(2), 481–496.
- 1354 Leuthold, J., Blundy, J., & Ulmer, P. (2023). Trace element partitioning in basaltic systems as a function of
1355 oxygen fugacity. *Contributions to Mineralogy and Petrology*, *178*(12).
- 1356 Li, W., Costa, F., Oppenheimer, C., & Nagashima, K. (2023). Volatile and trace element partitioning between
1357 apatite and alkaline melts. *Contributions to Mineralogy and Petrology*, *178*(2).
- 1358 Linnen, R. L., Pichavant, M., & Holtz, F. (1996). The combined effects of fO₂ and melt composition on SnO₂
1359 solubility and tin diffusivity in haplogranitic melts. *Geochimica et Cosmochimica Acta*, *60*(24), 4965–
1360 4976.
- 1361 Luo, Y., Hughes, J. M., Rakovan, J., & Pan, Y. (2009). Site preference of U and Th in Cl, F, and Sr apatites.
1362 *American Mineralogist*, *94*(2–3), 345–351.
- 1363 Maciag, B. J., & Brenan, J. M. (2020). Speciation of arsenic and antimony in basaltic magmas. *Geochimica et*
1364 *Cosmochimica Acta*, *276*, 198–218. <https://doi.org/10.1016/j.gca.2020.02.022>
- 1365 Mallmann, G., & O'Neill, H. St. C. (2009). The crystal/melt partitioning of V during mantle melting as a
1366 function of oxygen fugacity compared with some other elements (Al, P, Ca, Sc, Ti, Cr, Fe, Ga, Y, Zr and
1367 Nb). *Journal of Petrology*, *50*(9), 1765–1794.
- 1368 Mallmann, G., & O'Neill, H. St. C. (2013). Calibration of an Empirical Thermometer and Oxybarometer Based
1369 on the Partitioning of Sc, Y and V between Olivine and Silicate melt. *Journal of Petrology*, *54*(5), 933–
1370 949.
- 1371 Marks, M. A. W., Wenzel, T., Whitehouse, M. J., Loose, M., Zack, T., Barth, M., Worgard, L., Krasz, V., Eby, G.
1372 N., Stosnach, H., & Markl, G. (2012). The volatile inventory (F, Cl, Br, S, C) of magmatic apatite: An
1373 integrated analytical approach. *Chemical Geology*, *291*, 241–255.
- 1374 McCubbin, F. M., & Jones, R. H. (2015). Extraterrestrial apatite: Planetary geochemistry to astrobiology.
1375 *Elements*, *11*(3), 183–188.
- 1376 McDonough, W. F., & Sun, S. -s. (1995). The composition of the Earth. *Chemical Geology*, *120*, 223–253.
- 1377 McFarlane, C. R. M., & Luo, Y. (2012). U-Pb Geochronology Using 193 nm Excimer LA-ICP-MS Optimized for In
1378 Situ Accessory Mineral Dating in Thin Sections. *Geoscience Canada*, *39*(3), 158.

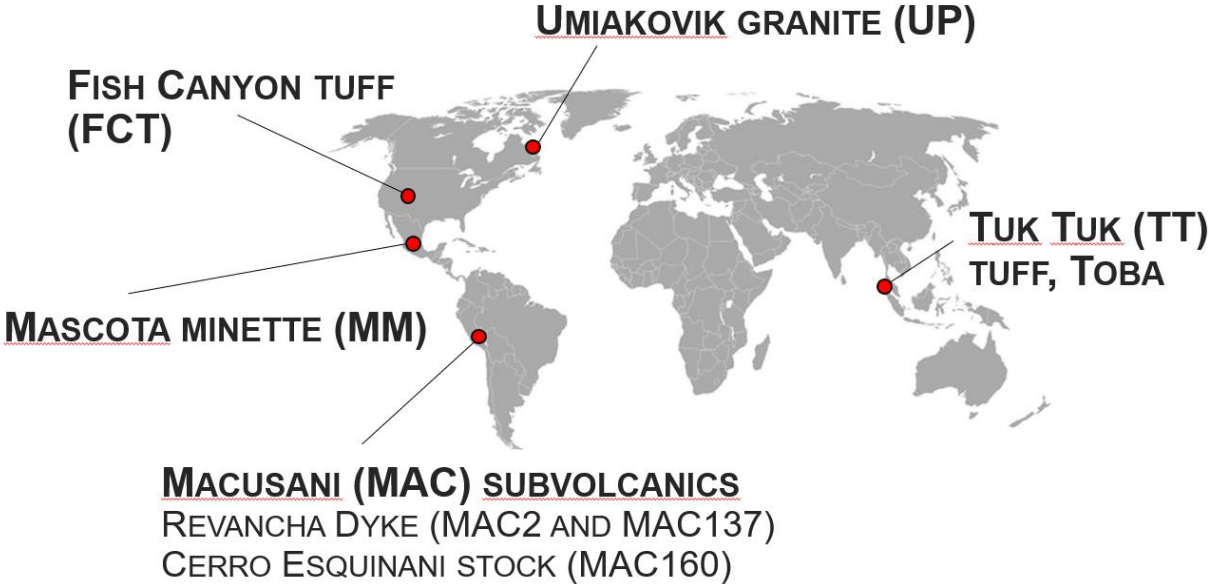
- 1379 McKeown, D. A., Muller, I. S., Gan, H., Feng, Z., Viragh, C., & Pegg, I. L. (2011). Vanadium and chromium redox
1380 behavior in borosilicate nuclear waste glasses. *Journal of Non-Crystalline Solids*, 357(14), 2735–2743.
- 1381 Moretti, R. (2005). Polymerisation, basicity, oxidation state and their role in ionic modelling of silicate melts.
1382 *Annals of Geophysics*, 48, 583–608.
- 1383 Moretti, R., & Neuville, D. (2021). Redox Equilibria: From Basic Concepts to the Magmatic Realm. In R.
1384 Moretti & D. Neuville (Eds.), *Magma Redox Geochemistry. Geophysical Monograph Series* (Vol. 266, pp.
1385 1–18).
- 1386 Mungall, J. E. (2002). Roasting the mantle: Slab melting and the genesis of major Au and Au-rich Cu deposits.
1387 *Geology*, 30, 915–918.
- 1388 Mysen, B. O. (1983). The structure of silicate melts. *Annual Review of Earth and Planetary Sciences*, 11, 75–
1389 97. www.annualreviews.org
- 1390 Nash, W. M., Smythe, D. J., & Wood, B. J. (2019). Compositional and temperature effects on sulfur speciation
1391 and solubility in silicate melts. *Earth and Planetary Science Letters*, 507, 187–198.
- 1392 Nickel, E. H. (1954). The distribution of major and minor elements among some co-existing ferromagnesian
1393 silicates. *American Mineralogist*, 39, 486–493.
- 1394 O'Neill, H. S. C., Berry, A. J., & Eggins, S. M. (2008). The solubility and oxidation state of tungsten in silicate
1395 melts: Implications for the comparative chemistry of W and Mo in planetary differentiation processes.
1396 *Chemical Geology*, 255(3–4), 346–359. <https://doi.org/10.1016/j.chemgeo.2008.07.005>
- 1397 O'Neill, H. St. C., & Mavrogenes, J. A. (2002). The Sulfide Capacity and the Sulfur Content at Sulfide Saturation
1398 of Silicate Melts at 1400°C and 1 bar. *Journal of Petrology*, 43, 1049–1087.
- 1399 Onuma, N., Higuchi, H., Wakita, H., & Nagasawa, H. (1968). Trace element partition between two pyroxenes
1400 and the host lava. *Earth and Planetary Science Letters*, 5, 47–51.
- 1401 Ottonello, G., Moretti, R., Marini, L., & Zuccolini, M. V. (2001). Oxidation state of iron in silicate glasses and
1402 melts: a thermochemical model. *Chemical Geology*, 174, 157–179.
- 1403 Padilla, A. J., & Gualda, G. A. R. (2016). Crystal-melt elemental partitioning in silicic magmatic systems: An
1404 example from the Peach Spring Tuff high-silica rhyolite, Southwest USA. *Chemical Geology*, 440, 326–
1405 344.
- 1406 Pan, Y., & Fleet, M. E. (2002). Compositions of the Apatite-Group Minerals: Substitution Mechanisms and
1407 Controlling Factors. *Phosphates: Geochemical, Geobiological and Materials Importance. Reviews in*
1408 *Mineralogy and Geochemistry*, 48, 13–50.
- 1409 Paton, C., Hellstrom, J., Paul, B., Woodhead, J., & Hergt, J. (2011). Lolite: Freeware for the visualisation and
1410 processing of mass spectrometric data. *Journal of Analytical Atomic Spectrometry*, 26(12), 2508–2518.
- 1411 Pichavant, M., Erdmann, S., Kontak, D. J., Michaud, J. A. S., & Villaros, A. (2024). Trace element partitioning in
1412 strongly peraluminous rare-metal silicic magmas – Implications for fractionation processes and for the
1413 origin of the Macusani Volcanics (SE Peru). *Geochimica et Cosmochimica Acta*, 229–252.

- 1414 Pichavant, M., Kontak, D. J., Briqueu, L., Herrera, J. V., & Clark, A. H. (1988a). The Miocene-Pliocene Macusani
1415 Volcanics, SE Peru. *Contributions to Mineralogy and Petrology*, *100*(3), 325–338.
- 1416 Pichavant, M., Kontak, D. J., Briqueu, L., Herrera, J. V., & Clark, A. H. (1988b). The Miocene-Pliocene Macusani
1417 Volcanics, SE Peru II. Geochemistry and origin of a felsic peraluminous magma. *Contributions to*
1418 *Mineralogy and Petrology*, *100*(3), 325–338.
- 1419 Pichavant, M., & Montel, J.-M. (1988). Petrogenesis of a two-mica ignimbrite suite: Macusani Volcanics, SE
1420 Peru. *Transactions of the Royal Society of Edinburgh: Earth Sciences*, *79*, 14–16.
- 1421 Pichavant, M., Villaros, A., Deveaud, S., Scaillet, B., & Lahlafi, M. (2016). The influence of redox state on mica
1422 crystallization in leucogranitic and pegmatitic liquids. *Canadian Mineralogist*, *54*, 559–581.
- 1423 Prowatke, S., & Klemme, S. (2006). Trace element partitioning between apatite and silicate melts. *Geochimica*
1424 *et Cosmochimica Acta*, *70*(17), 4513–4527.
- 1425 Righter, K., & Carmichael, I. S. E. (1996). Phase equilibria of phlogopite lamprophyres from western Mexico:
1426 biotite-liquid equilibria and P-T estimates for biotite-bearing igneous rocks. *Contrib Mineral Petrol*, *123*,
1427 1–21.
- 1428 Rudnick, R. L., & Gao, S. (2003). Composition of the Continental Crust. In *Treatise on Geochemistry* (Vols. 3–9,
1429 pp. 1–64). Elsevier Inc.
- 1430 Saha, R., Upadhyay, D., & Mishra, B. (2021). Discriminating Tectonic Setting of Igneous Rocks Using Biotite
1431 Major Element chemistry—A Machine Learning Approach. *Geochemistry, Geophysics, Geosystems*,
1432 *22*(11).
- 1433 Sandeman, H. A., & Clark, A. H. (2003). Glass-rich, Cordierite-Biotite Rhyodacite, Valle Ninahuisa, Puno, SE
1434 Peru: Petrological evidence for hybridization of “Lachlan S-type” and potassic mafic magmas. *Journal of*
1435 *Petrology*, *44*(2), 355–385.
- 1436 Sandeman, H. A., & Clark, A. H. (2004). Commingling and mixing of S-type peraluminous, ultrapotassic and
1437 basaltic magmas in the Cayconi volcanic field, Cordillera de Carabaya, SE Peru. *Lithos*, *73*(3–4), 187–213.
- 1438 Sandeman, H. A., Clark, A. H., Farrar, E., & Arroyo-Pauca, G. (1997). Lithostratigraphy, petrology and ⁴⁰Ar-
1439 ³⁹Ar geochronology of the Crucero Supergroup, Puno Department, SE Peru. *Journal of South American*
1440 *Earth Sciences*, *10*(3–4), 223–245.
- 1441 Schmidt, K. H., Bottazzi, P., Vannucci, R., & Mengel, K. (1999). Trace element partitioning between
1442 phlogopite, clinopyroxene and leucite lamproite melt. *Earth and Planetary Science Letters*, *168*, 287–
1443 299.
- 1444 Schreiber, H. D. (1983). The chemistry of uranium in glass-forming aluminosilicate melts. *Journal of the Less-*
1445 *Common Metals*, *91*, 129–147.
- 1446 Shimizu, K., Liang, Y., Sun, C., Jackson, C. R. M., & Saal, A. E. (2017). Parameterized lattice strain models for
1447 REE partitioning between amphibole and silicate melt. *American Mineralogist*, *102*(11), 2254–2267.
- 1448 Smythe, D. J., & Brenan, J. M. (2015). Cerium oxidation state in silicate melts: Combined fO₂, temperature
1449 and compositional effects. *Geochimica et Cosmochimica Acta*, *170*, 173–187.

- 1450 Smythe, D. J., & Brenan, J. M. (2016). Magmatic oxygen fugacity estimated using zircon-melt partitioning of
1451 cerium. *Earth and Planetary Science Letters*, *453*, 260–266.
- 1452 Sossi, P. A., Prytulak, J., & O'Neill, H. S. C. (2018). Experimental calibration of vanadium partitioning and
1453 stable isotope fractionation between hydrous granitic melt and magnetite at 800 °C and 0.5 GPa.
1454 *Contributions to Mineralogy and Petrology*, *173*(4).
- 1455 Spencer, K. J., & Lindsley, D. H. (1981). A solution model for coexisting iron-titanium oxides. *American*
1456 *Mineralogist*, *66*, 1189–1201.
- 1457 Stokes, T. N., Bromiley, G. D., Potts, N. J., Saunders, K. E., & Miles, A. J. (2019). The effect of melt composition
1458 and oxygen fugacity on manganese partitioning between apatite and silicate melt. *Chemical Geology*,
1459 *506*, 162–174.
- 1460 Sutton, S. R., Karner, J., Papike, J., Delaney, J. S., Shearer, C., Newville, M., Eng, P., Rivers, M., & Dyar, M. D.
1461 (2005). Vanadium K edge XANES of synthetic and natural basaltic glasses and application to microscale
1462 oxygen barometry. *Geochimica et Cosmochimica Acta*, *69*(9), 2333–2348.
- 1463 Taylor, W. R., & Green, D. H. (1988). Measurement of reduced peridotite-C-O-H solidus and implications for
1464 redox melting of the mantle. *Nature*, *332*(6162), 349–352.
- 1465 Wang, H., Wang, L., & Seetharaman, S. (2016). Determination of Vanadium Oxidation States in CaO-MgO-
1466 Al₂O₃-SiO₂-VO_x System by K Edge XANES Method. *Steel Research International*, *87*(2), 199–209.
- 1467 Watson, E. B., & Green, T. H. (1981). Apatite/liquid partition coefficients for the rare earth elements and
1468 strontium. *Earth and Planetary Science Letters*, *56*, 405–421.
- 1469 Webster, J. D., & Piccoli, P. M. (2015). Magmatic apatite: A powerful, yet deceptive, mineral. *Elements*, *11*(3),
1470 177–182. <https://doi.org/10.2113/gselements.11.3.177>
- 1471 Wei, C., Xiong, X., Wang, J., Huang, F., & Gao, M. (2024). Partitioning of tin between mafic minerals, Fe-Ti-
1472 oxides and silicate melts: Implications for tine enrichment in magmatic processes. *Geochimica et*
1473 *Cosmochimica Acta*, *372*, 81–100.
- 1474 Were, P., & Keppler, H. (2021). Trace element fractionation between biotite, allanite, and granitic melt.
1475 *Contributions to Mineralogy and Petrology*, *176*(9).
- 1476 Westrenen van, W., & Draper, D. S. (2007). Quantifying garnet-melt trace element partitioning using lattice-
1477 strain theory: New crystal-chemical and thermodynamic constraints. *Contributions to Mineralogy and*
1478 *Petrology*, *154*(6), 717–730.
- 1479 Whitney, D. L., & Evans, B. W. (2010). Abbreviations for names of rock-forming minerals. *American*
1480 *Mineralogist*, *95*(1), 185–187.
- 1481 Whitney, J. A., & Stormer, J. C. (1985). Mineralogy, Petrology, and Magmatic Conditions from the Fish Canyon
1482 Tuff, Central San Juan Volcanic Field, Colorado. *Journal of Petrology*, *26*(3), 726–762.
- 1483 Wood, B. J., & Blundy, J. D. (2013). Trace Element Partitioning: The Influences of Ionic Radius, Cation Charge,
1484 Pressure, and Temperature. In K. K. Turekian & Holland. H. D. (Eds.), *Treatise on Geochemistry: Second*
1485 *Edition* (Vol. 3, pp. 421–448). Elsevier Inc.

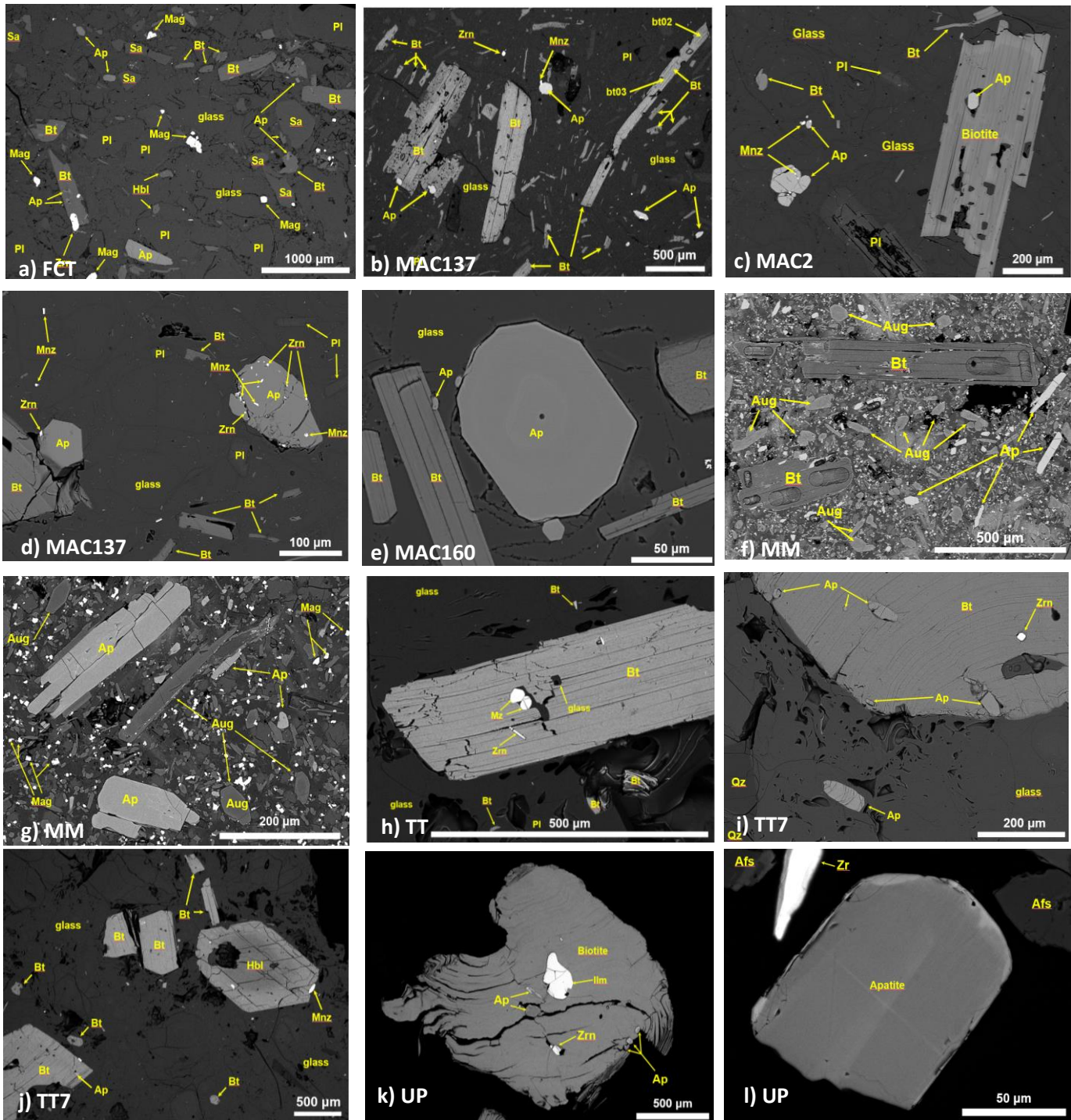
- 1486 Young, E. J., Myers, A. T., Munson, E. L., & Conklin, N. M. (1969). Mineralogy and geochemistry of fluorapatite
1487 from Cerro de Mercado, Durango, Mexico. *U.S. Geological Survey Paper, 650D*, 84–93.
- 1488 Zajacz, Z., & Halter, W. (2007). LA-ICPMS analyses of silicate melt inclusions in co-precipitated minerals:
1489 Quantification, data analysis and mineral/melt partitioning. *Geochimica et Cosmochimica Acta, 71(4)*,
1490 1021–1040.
- 1491 Zhan, Q. Y., Zhu, D. C., Weinberg, R. F., Wang, Q., Xie, J. C., Zhang, L. L., & Zhao, Z. D. (2022). Cumulate
1492 granites: A perspective from new apatite MgO partition coefficients. *Geology, 50(6)*, 681–685.
- 1493
- 1494

1495 Figures



1496

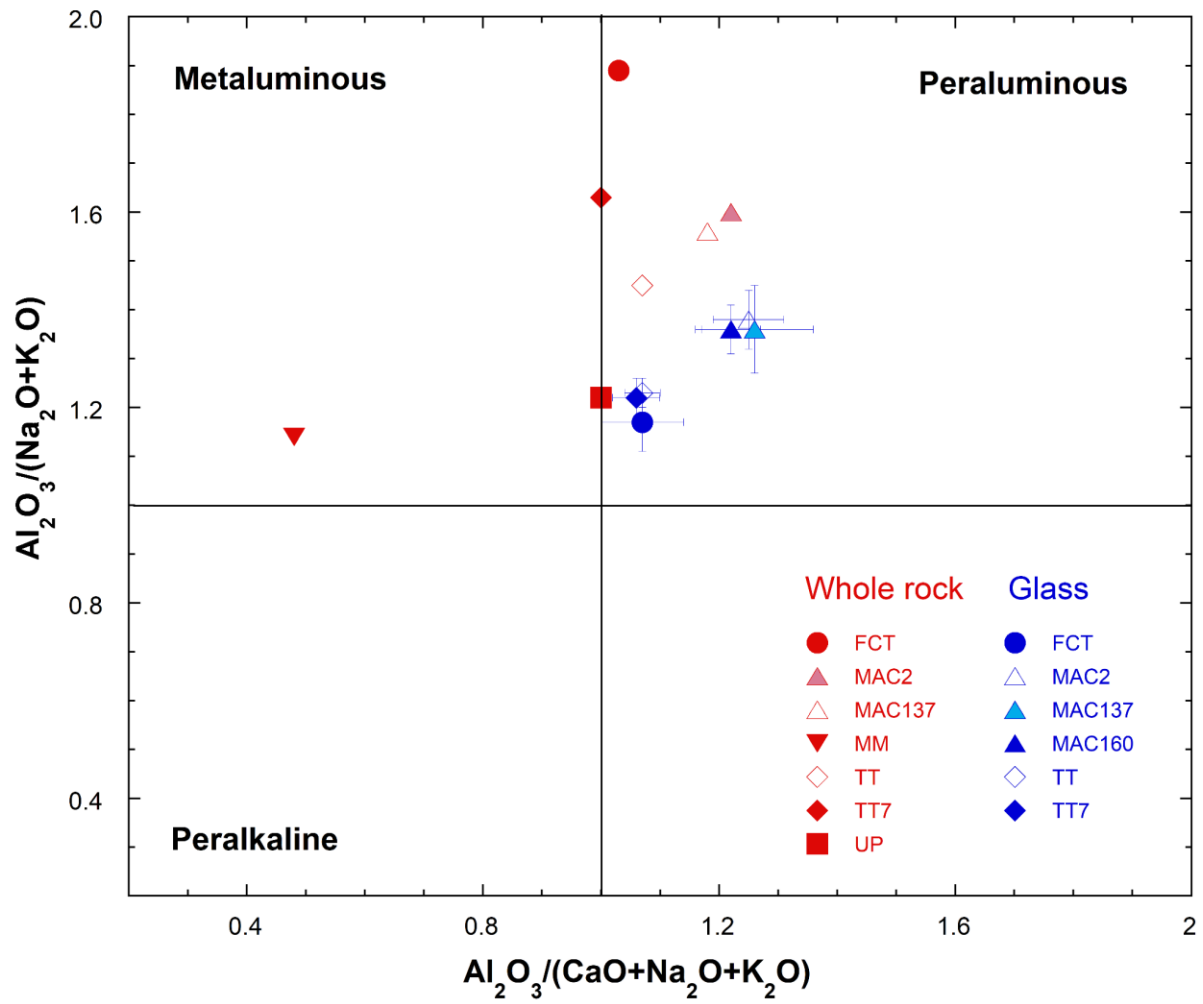
1497 Figure 1.



1498

1499 **Figure 2.**

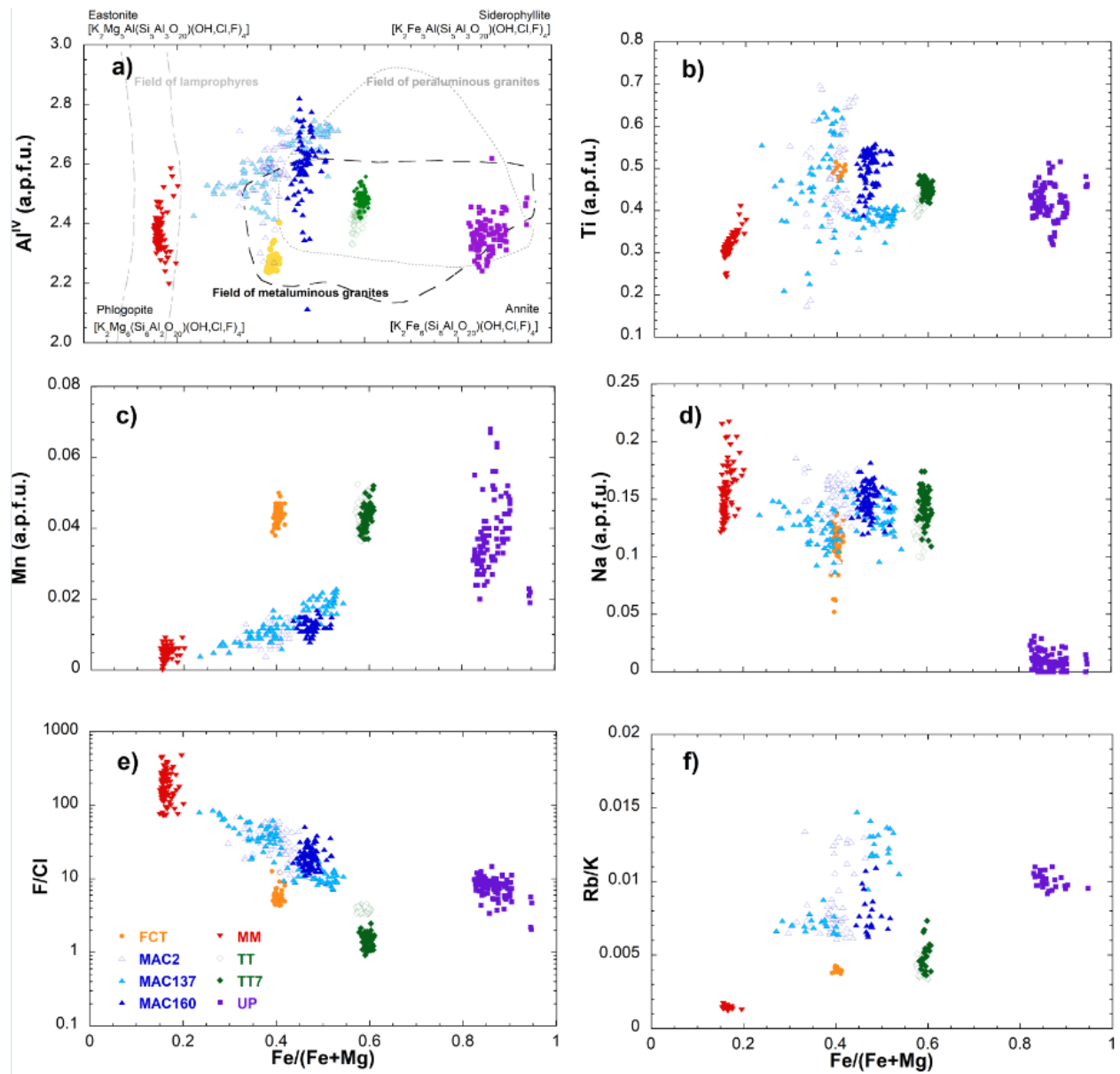
1500



1501

1502 **Figure 3 .**

1503



1504

1505 **Figure 4.**

1506

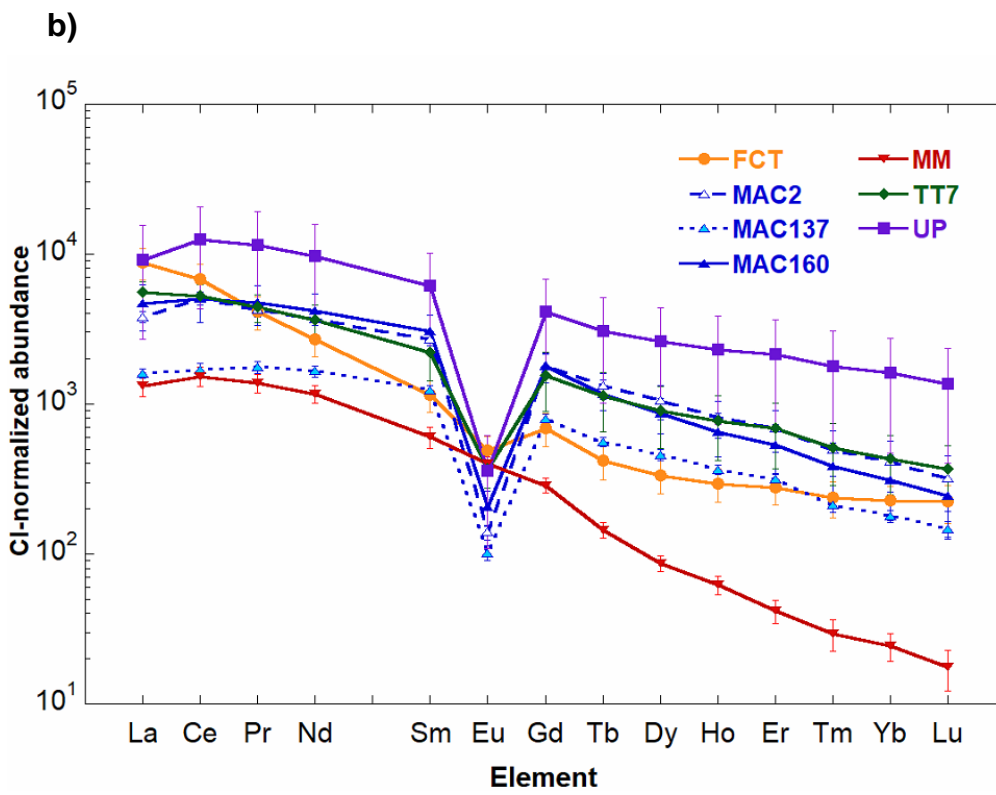
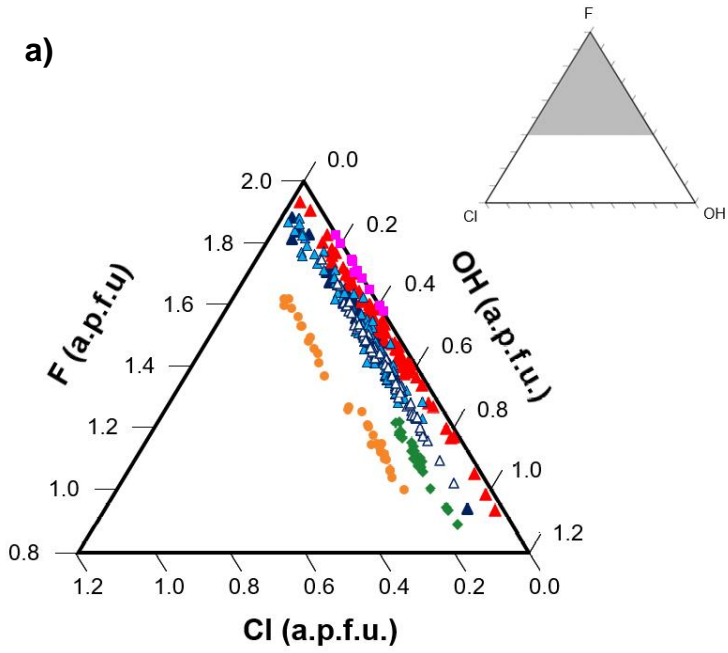
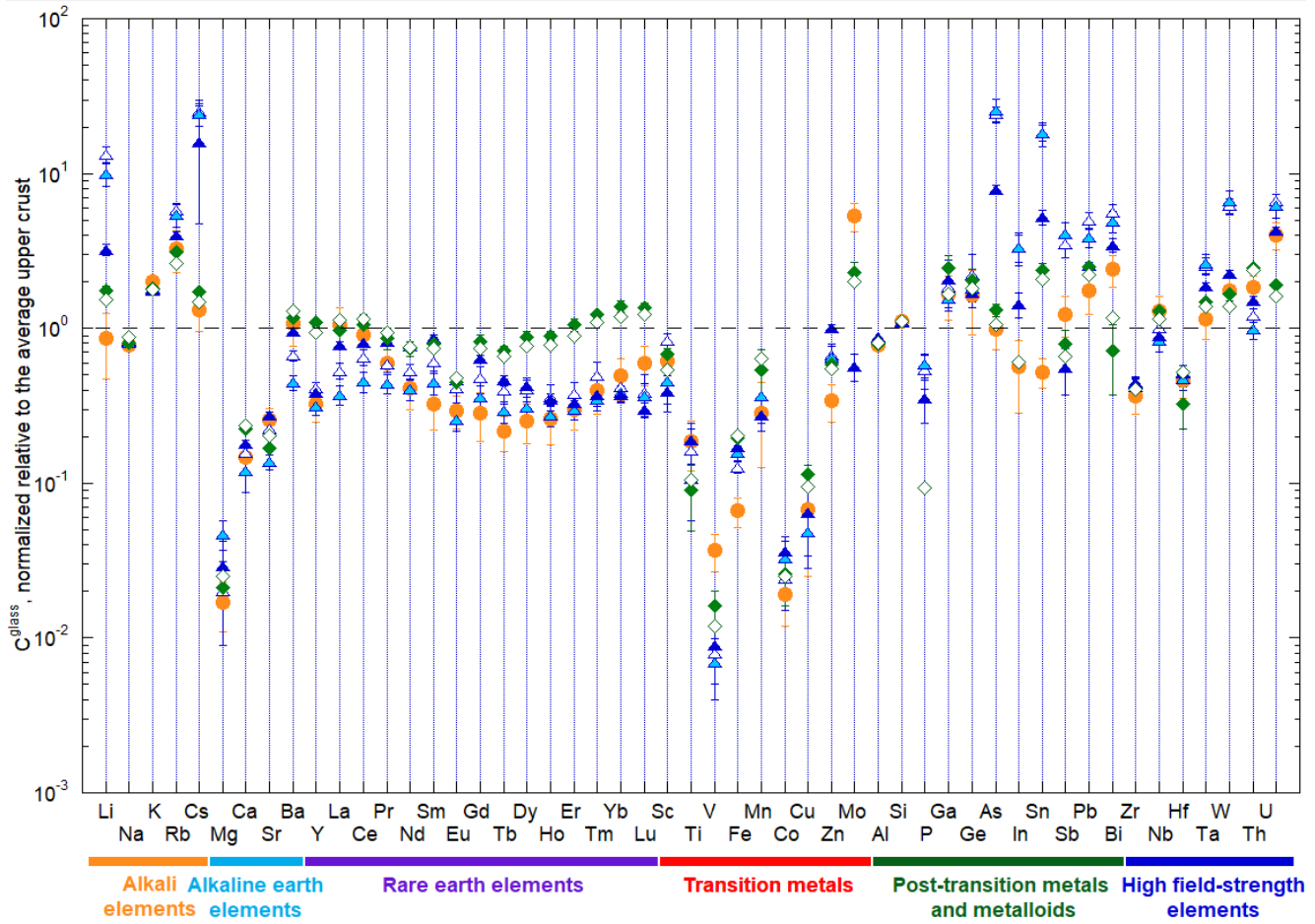


Figure 5.

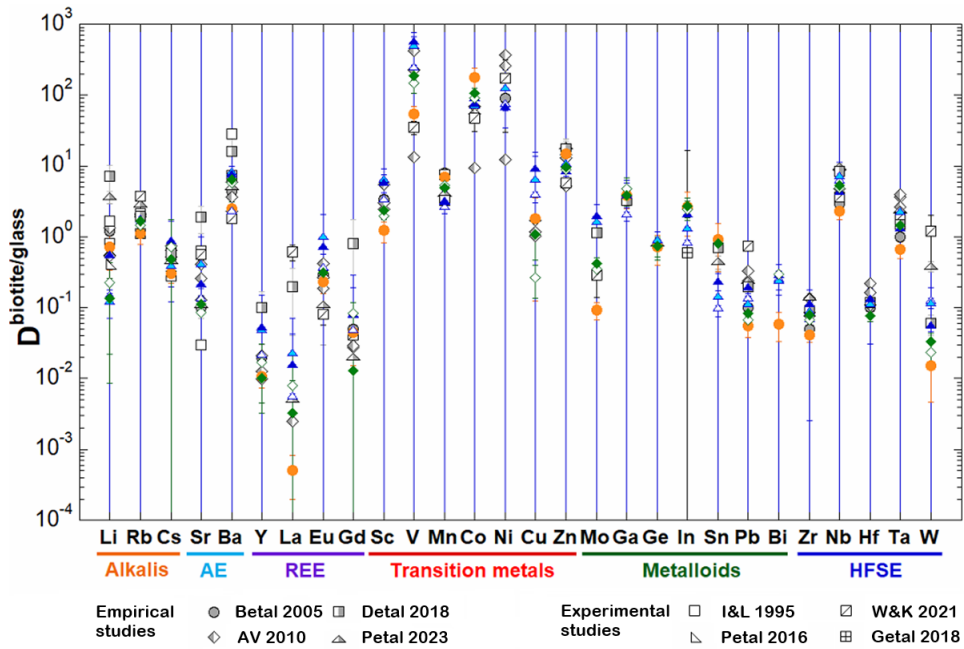


1511

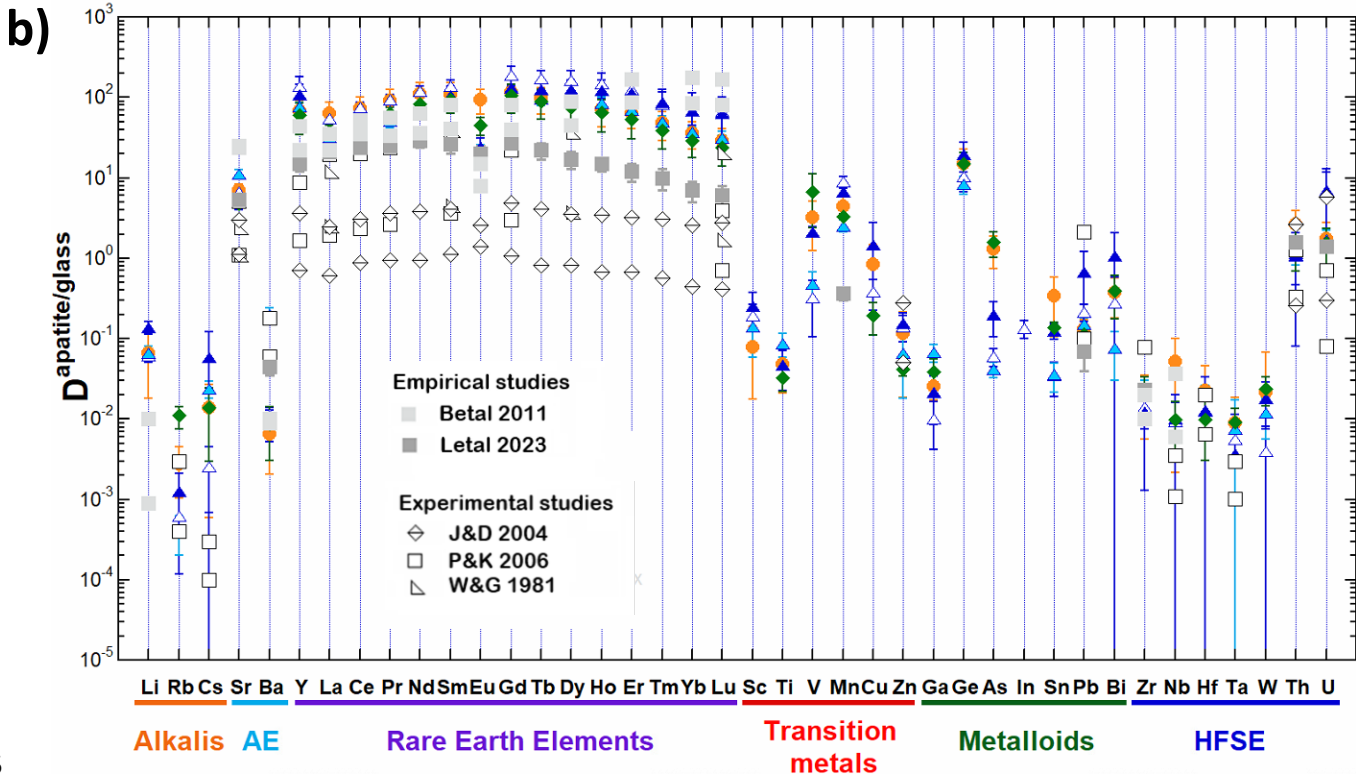
1512 **Figure 6.**

1513

a)



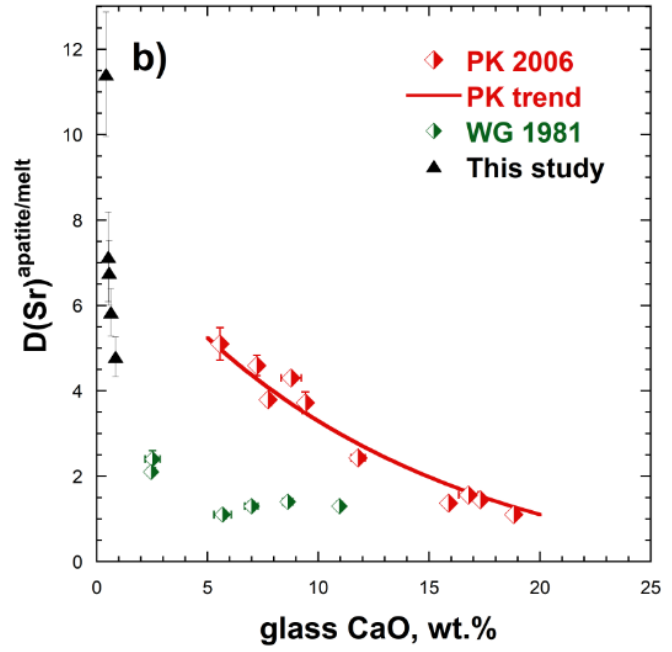
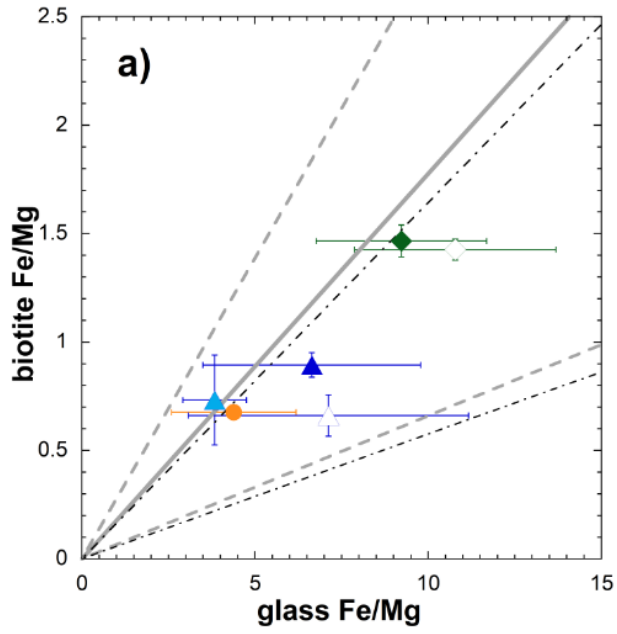
1514



1515

1516

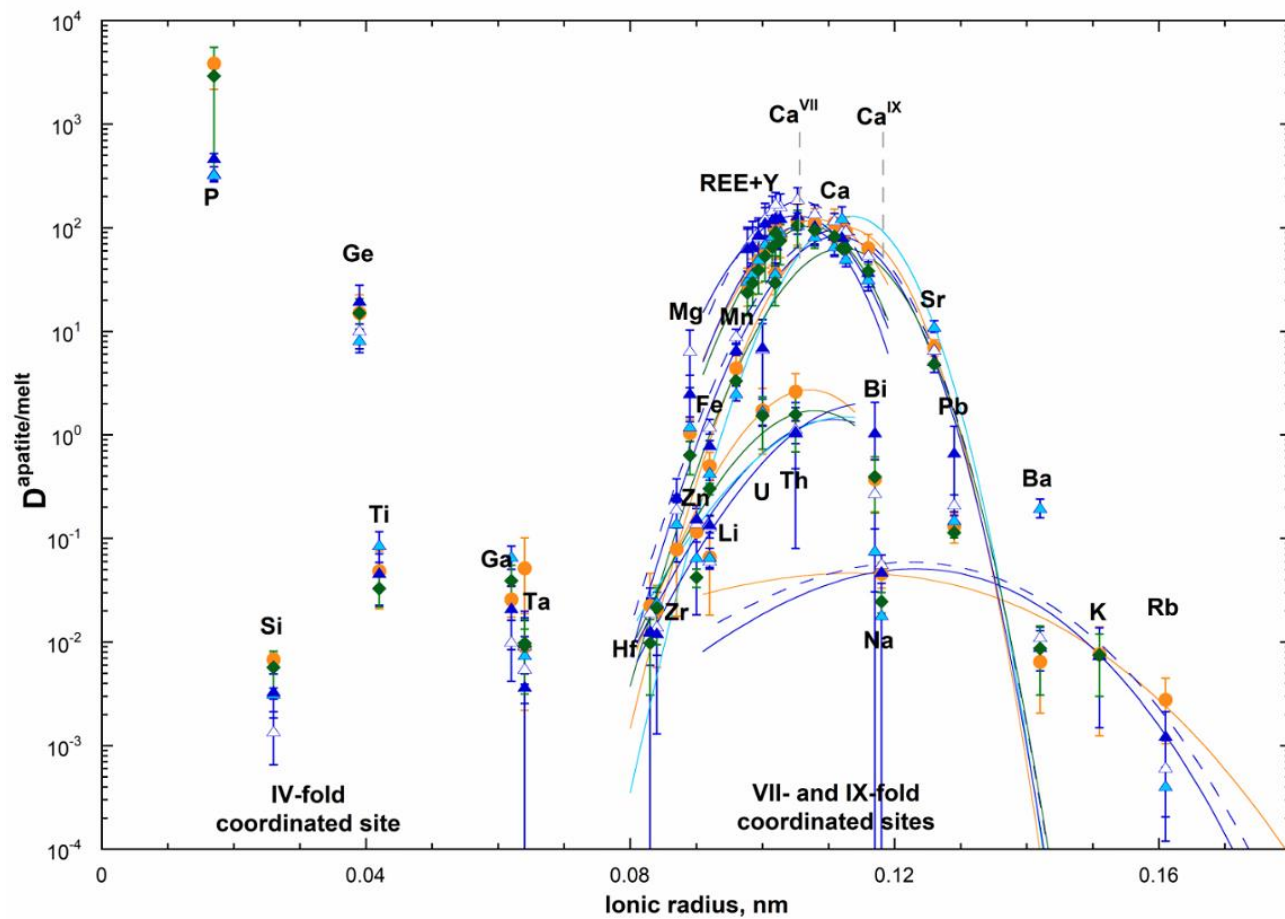
Figure 7.



1517

1518 **Figure 8.**

1519

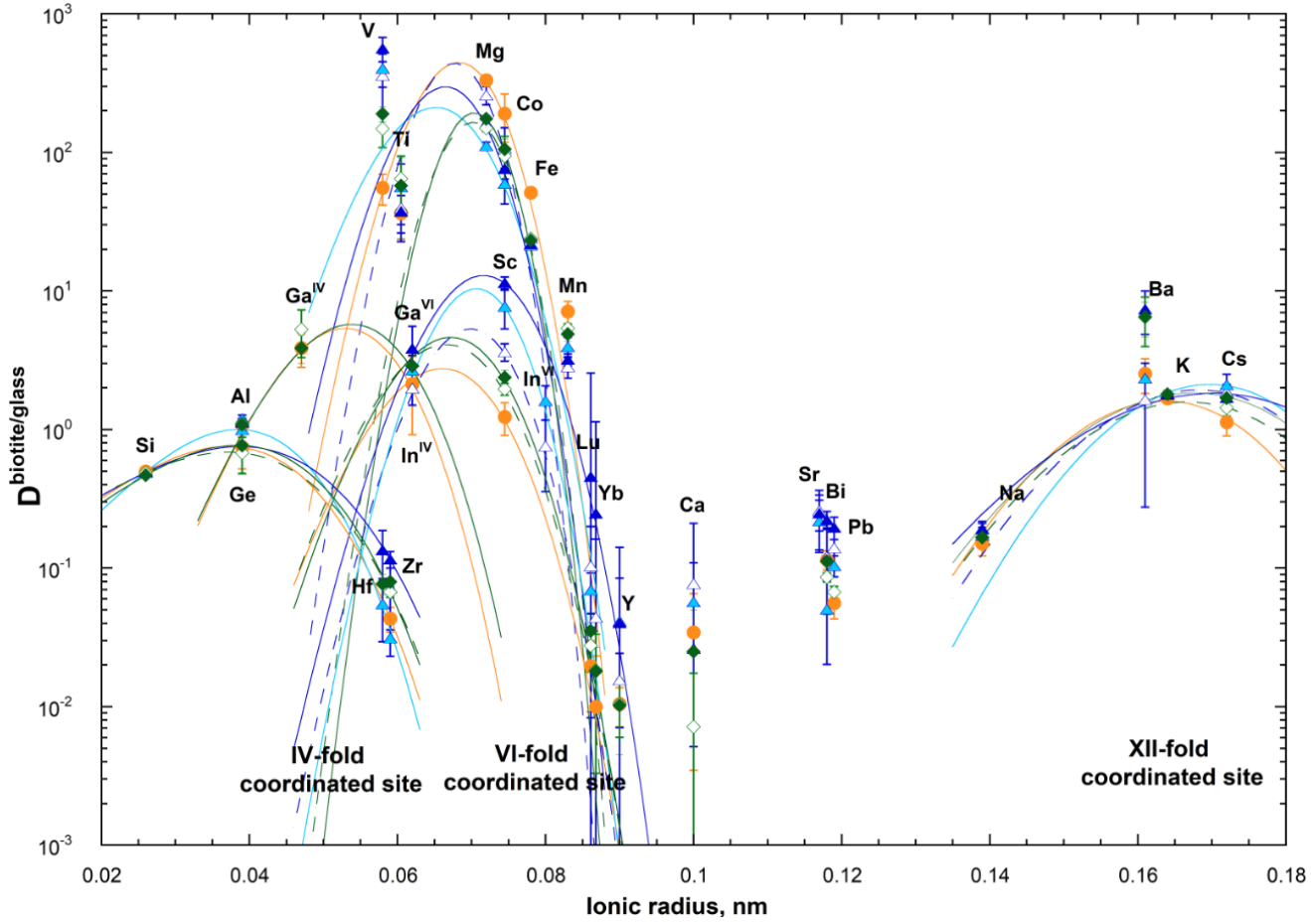


1520

1521 **Figure 9.**

1522

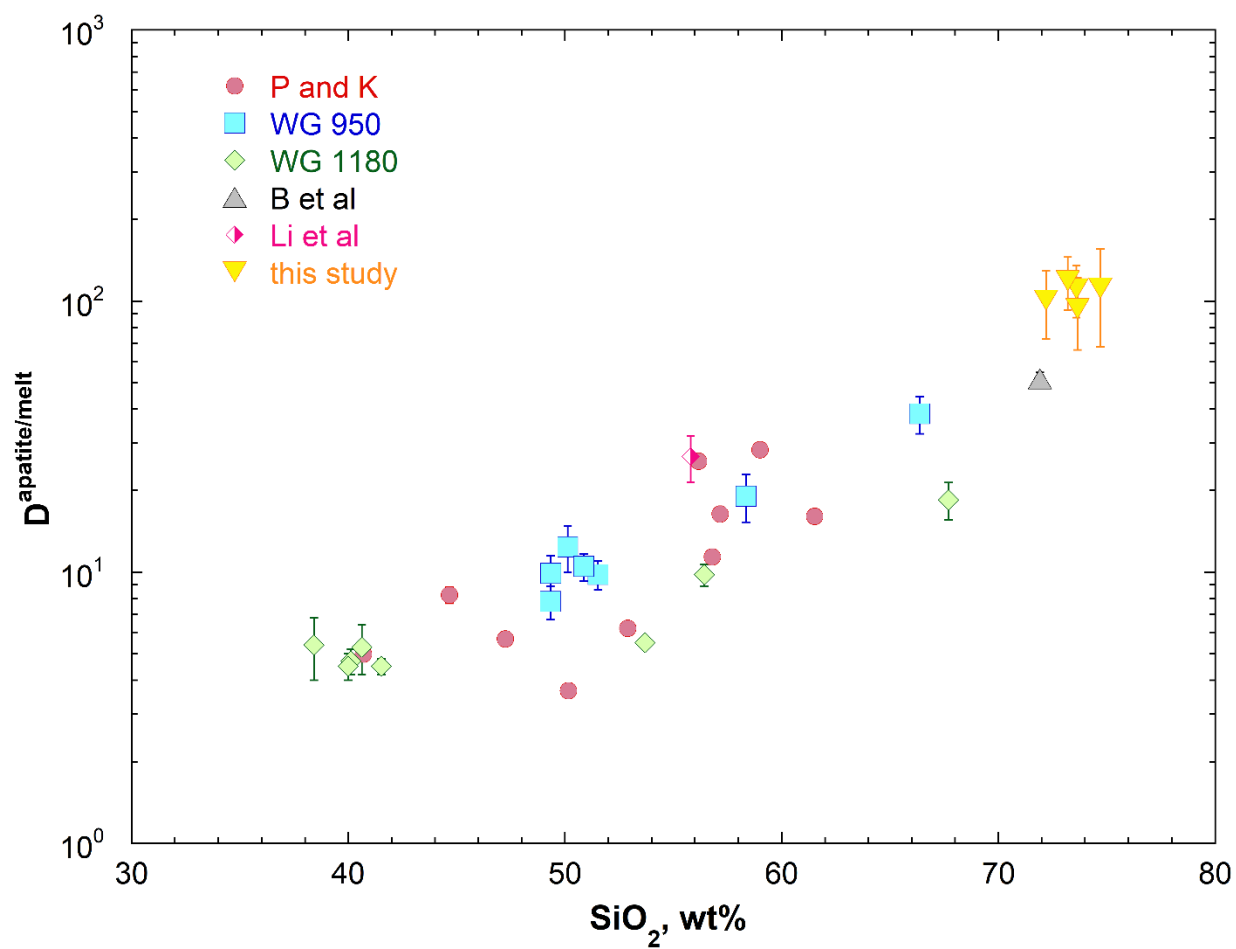
1523



1524

1525 **Figure 10.**

1526

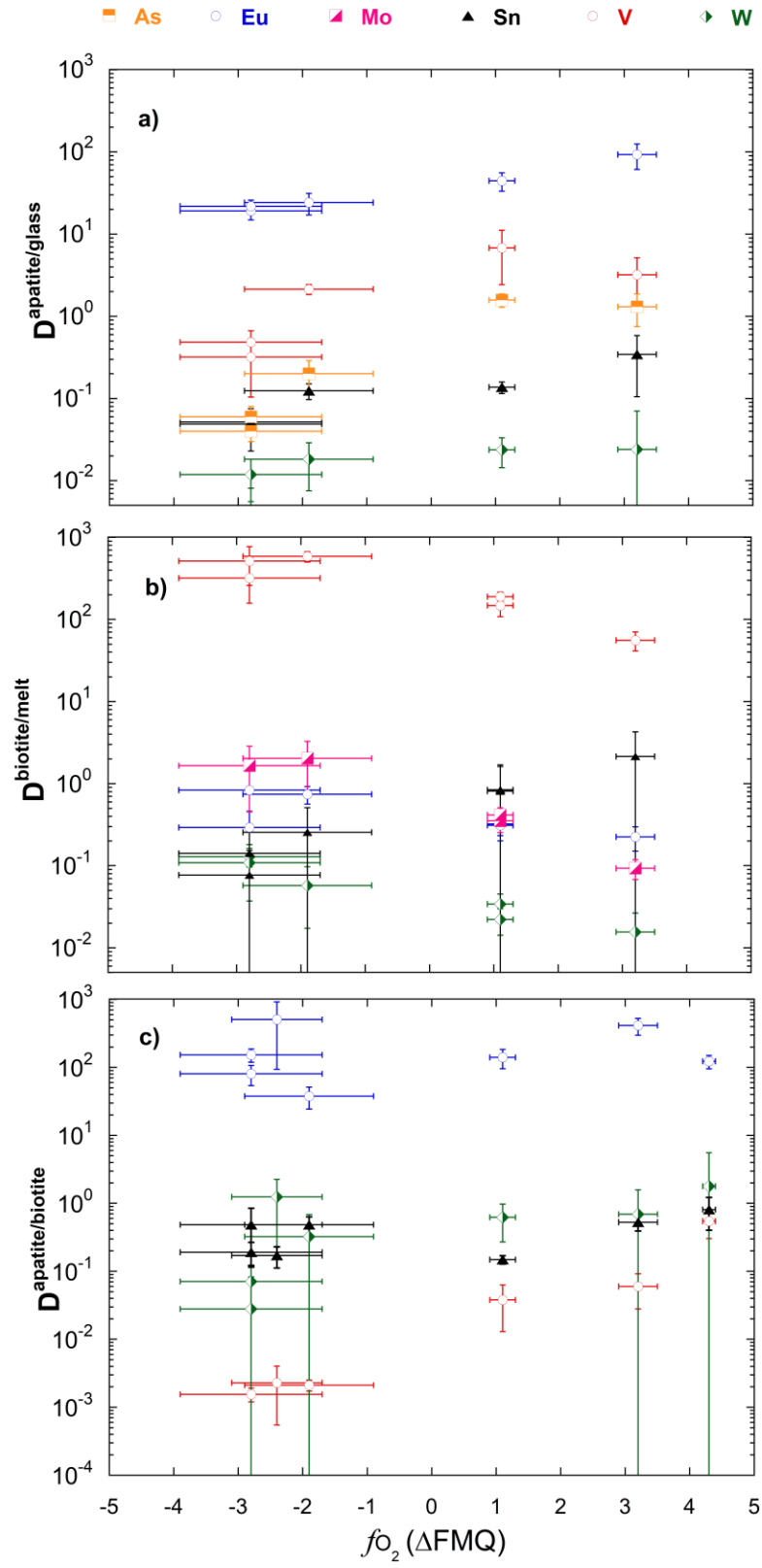


1527

1528 **Figure 11.**

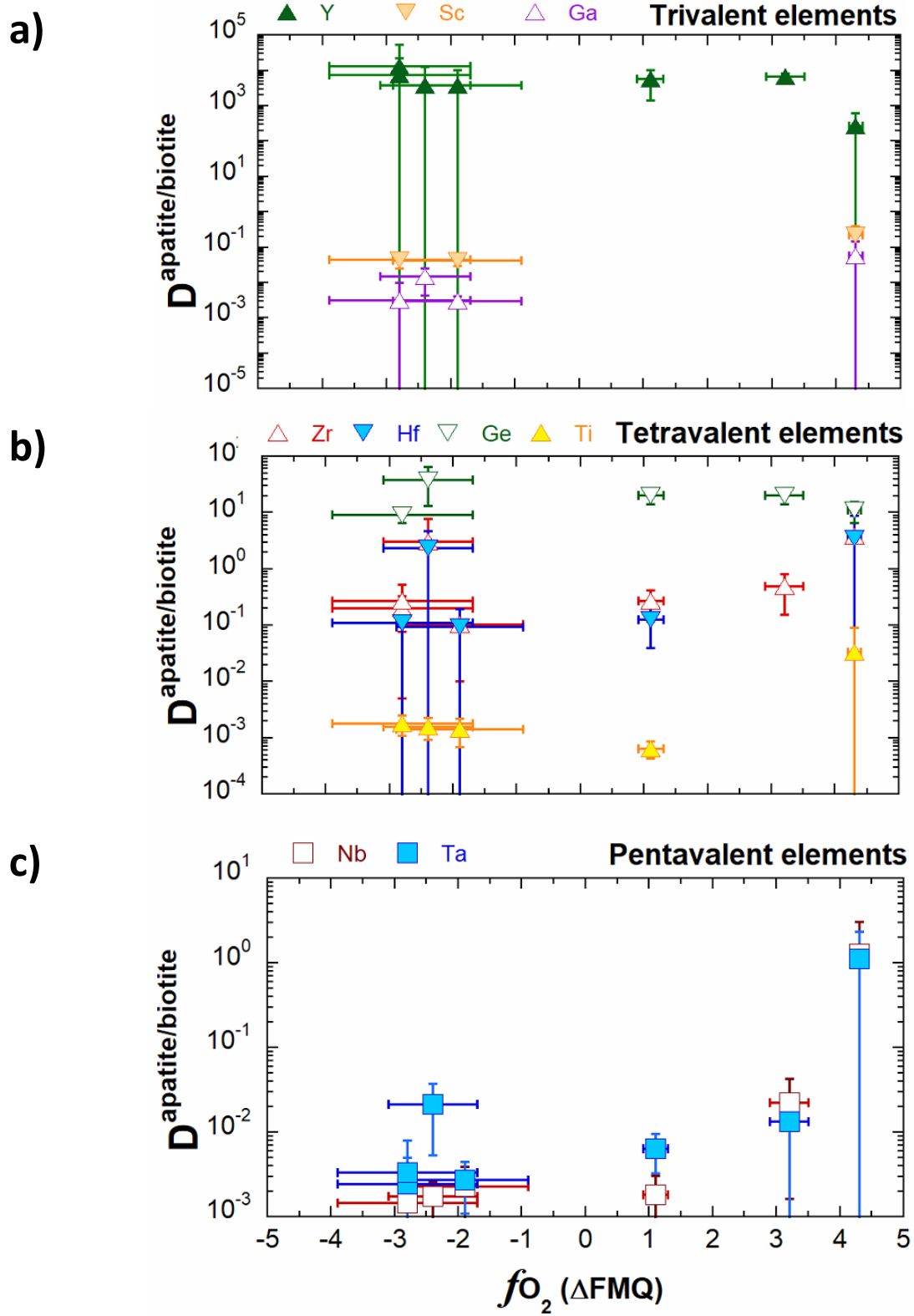
1529

1530

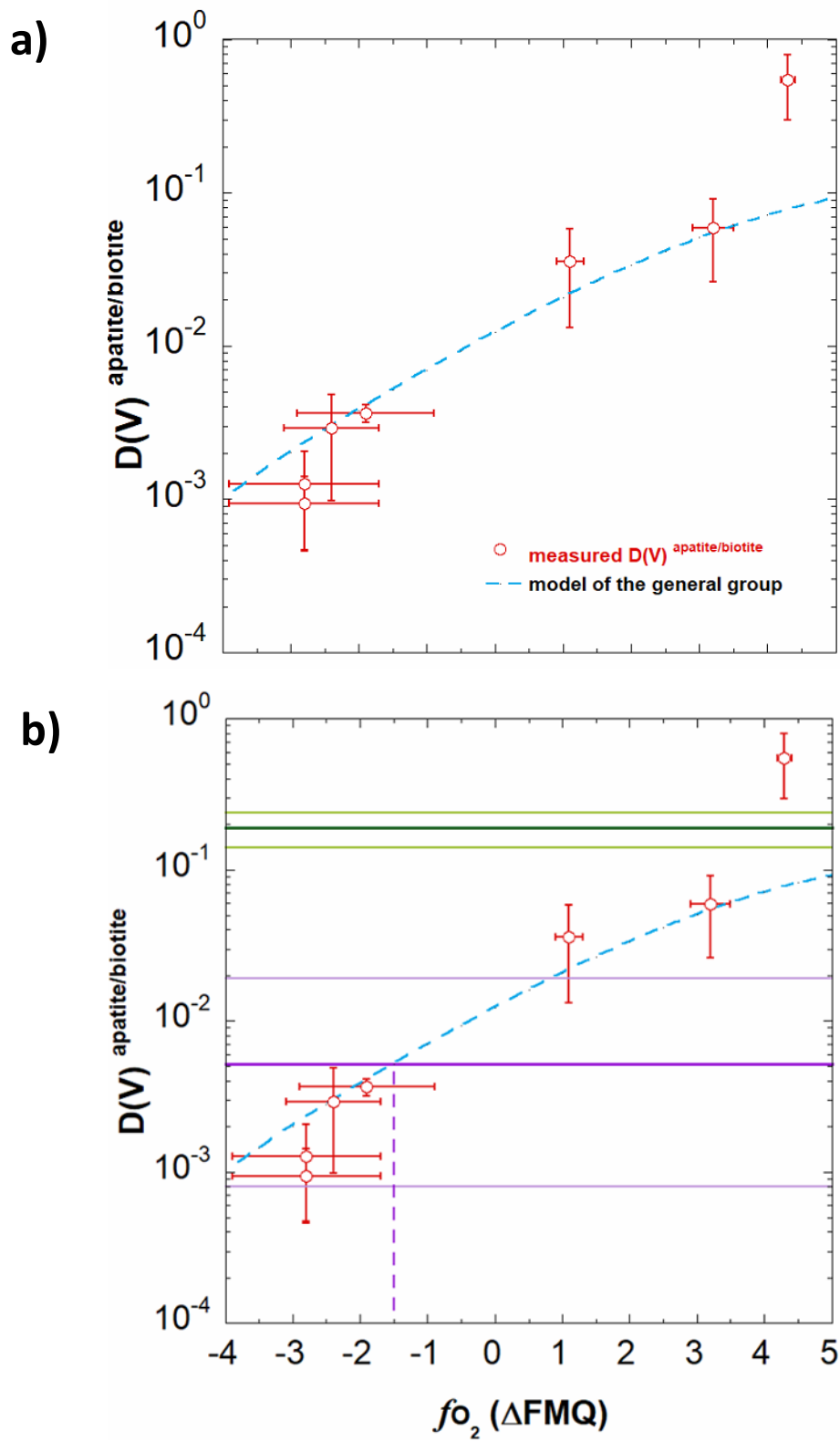


1531

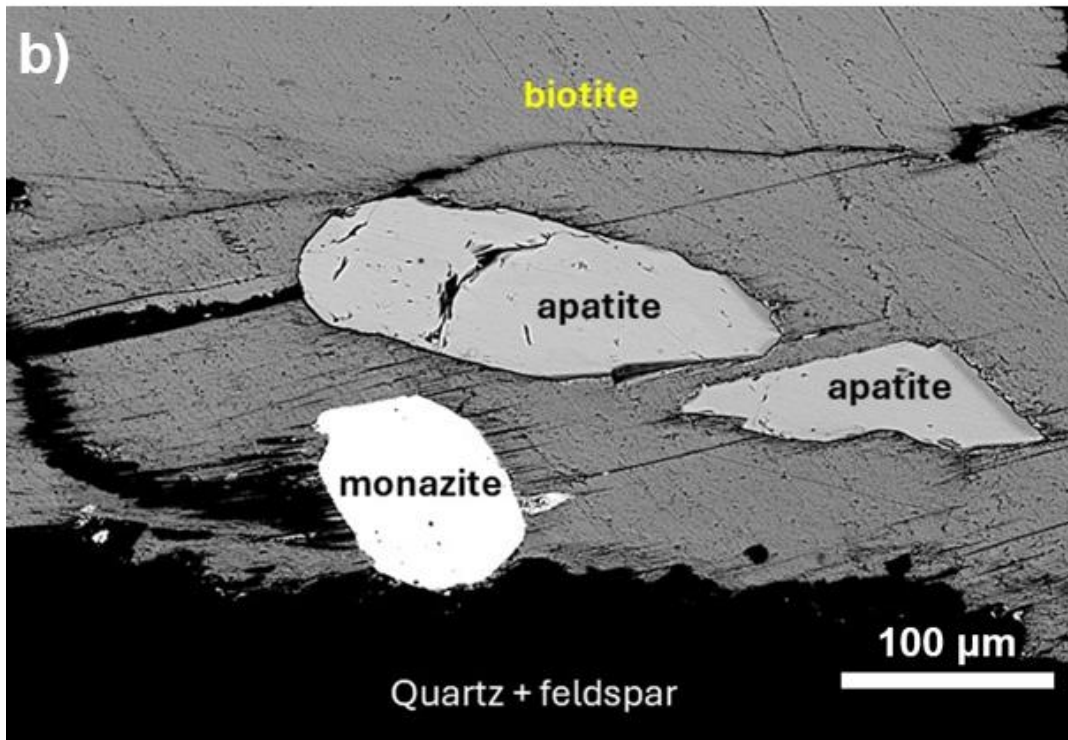
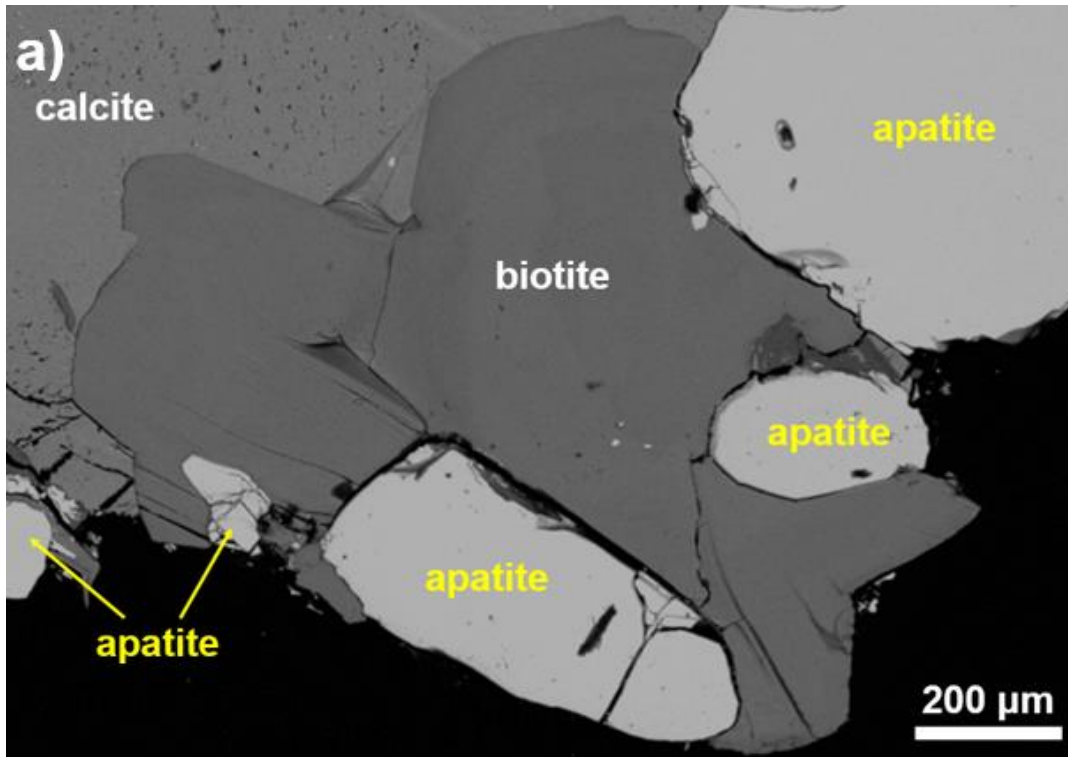
1532 **Figure 12.**



1533 Figure 13.



1534 **Figure 14.**



1535

1536

1537

1538 **Figure 15.**

1539 **Tables**

1540 **Table 1.** Summary of the analysed samples. Oxybarometry methods: cerium-in-zircon (Smythe &
 1541 Brenan, 2016) for MAC (this study), UP (Smythe & Brenan, 2016); whole-rock iron oxidation state
 1542 (Ghiorso & Sack, 1995) for MM (Carmichael et al., 1996), Fe-Ti oxide oxybarometry (Ghiorso & Sack,
 1543 1991) for FCT (Whitney & Stormer, 1985) and TT (Chesner, 1998).

Sample	Petrology (phase assemblage)	SiO ₂ (wt%)	A/CNK	fO ₂ (ΔFMQ)	T (°C)
Fish Canyon tuff, FCT	Dacitic ignimbrite (Pl + Gl + Afs + Qz + Hbl + Bt + Ttn + Mag + Ilm + Ap + Zrn)	62.4-65.2	1.03	+2.8 ±0.3	700–760 (Johnson & Rutherford, 1989)
Revancha dyke, MAC2, MAC137	Cordierite-biotite rhyodacite (Gl + Pl + Bt + Crd + Qz + Afs + Ap + Ilm + Mnz + Zrn)	67.7-67.8	1.18-1.22	-2.8 ±1.1	634-693 (Sandeman & Clark, 2003)
Cerro Esquinani stock, MAC160	Biotite rhyodacite (Gl + Pl + Bi + Qz + Sil + Ap + Ilm + Mnz + Zrn)	66.8-71.7	1.13-1.28	-1.9 ±1.0	-
Mascota minette, MM	Augite minette (Aug + Bt + Ap + Mag)	48.7	0.47	+4.2 ±0.1	1080-1100 (Carmichael et al., 1996)
Tuk Tuk tuff, TT	Rhyolite (Gl + Pl + Qz + Bt + Afs + Hbl + Zr + Aln + Mag + Ilm + Mnz ± Ap)	69.8-72.7	1.00-1.07	+1.2 ±0.2	701-780 (Chesner, 2012)
Umiakovik granite, UP	Biotite-hornblende granite (Afs + Qz + Pl + Bt + Hbl + Ilm + Ap + Zrn + Fl)	73.2	1.00	-2.4 ±0.7	725-825 (Emslie & Stirling, 1993)

1544

1545

1546 **Table 2.** Microanalytical conditions of EPMA and LA-ICP-MS used in this study.

Phase	Zircon (n=25)	Apatite (n=319)	Biotite (n=374)	Glass (n=289)
EPMA conditions	15 kV accelerating voltage, 10 nA beam current, 10 µm spot size			15 kV accelerating voltage, 10 nA beam current, 10 µm spot
Primary standards	Standards for zircon analysis were zircon (Zr), (Hf), (Y), (P)	synthetic fluorapatite (Ca, P, F); tugtupite (Cl); garnet (Fe, Si, Al); pyrolusite (Mn); albite (Na); biotite (K, Mg); K kaersutite (Ti)	Biotite (Fe, Al, Si, K, Mg), pyrolusite (Mn), kaersutite (Ca, Ti), albite (Na), tugtupite (Cl) and apatite (F)	BHVO-1 (Ca, Na, Mg, Al, Fe, Si); sanidine (K); rutile (Ti); chromite (Cr); pyrolusite (Mn); synthetic fluorapatite (P, F); tugtupite (Cl); barite (Ba); celestite (Sr); pyrrhotite (S)
Count time	20 s for all analytes, except F (90 s) and Cl (40 s) in apatite, biotite, and glass			
Secondary standards	Synthetic zircon	Durango apatite	San Carlos biotite, DJ biotite	BIR-1 and CAM66
LA-ICP-MS conditions	10 Hz repetition rate, ~5 J/cm ² , 15-100 µm spot size depending on the crystal size and availability of crystal-free domains in glass. 15-25 µm spot size for zircon.			
Analytes	²³ Na, ²⁷ Al, ²⁹ Si, ³¹ P, ⁴³ Ca, ⁴⁴ Ca, ⁴⁹ Ti, ⁵⁵ Mn, ⁵⁶ Fe, ⁸⁹ Y, ⁹⁰ Zr, ¹³⁹ La, ¹⁴⁰ Ce, ¹⁴¹ Pr, ¹⁴⁶ Nd, ¹⁴⁷ Sm, ¹⁵³ Eu, ¹⁵⁷ Gd, ¹⁵⁹ Tb, ¹⁶³ Dy, ¹⁶⁵ Ho, ¹⁶⁶ Er, ¹⁶⁹ Tm, ¹⁷² Yb, ¹⁷⁵ Lu, ¹⁷⁸ Hf, ²³² Th, ²³⁸ U	⁷ Li, ²⁷ Al, ²⁹ Si, ³¹ P, ⁴³ Ca, ⁴⁵ Sc, ⁴⁷ Ti (glass, biotite), ⁴⁹ Ti (apatite), ⁵¹ V, ⁵² Cr, ⁵⁵ Mn, ⁵⁷ Fe, ⁵⁹ Co, ⁶¹ Ni, ⁶³ Cu, ⁶⁵ Cu, ⁶⁶ Zn, ⁶⁹ Zn, ⁷³ Ge, ⁷⁵ As, ⁸⁵ Rb, ⁸⁸ Sr, ⁸⁹ Y, ⁹⁰ Zr, ⁹³ Nb, ⁹⁵ Mo, ¹¹¹ Cd, ¹¹³ In, ¹¹⁵ In, ¹¹⁸ Sn, ¹²¹ Sb, ¹³³ Cs, ¹³⁷ Ba, ¹³⁹ La, ¹⁴⁰ Ce, ¹⁴¹ Pr, ¹⁴⁶ Nd, ¹⁴⁷ Sm, ¹⁵³ Eu, ¹⁵⁷ Gd, ¹⁵⁹ Tb, ¹⁶³ Dy, ¹⁶⁵ Ho, ¹⁶⁶ Er, ¹⁶⁹ Tm, ¹⁷² Yb, ¹⁷⁵ Lu, ¹⁷⁸ Hf, ¹⁸¹ Ta, ¹⁸² W, ²⁰⁶ Pb, ²⁰⁸ Pb, ²⁰⁹ Bi, ²³² Th, ²³⁸ U		
Dwell time	10 ms (most analytes), 30 ms (¹³⁹ La, ¹⁴¹ Pr)	10 ms (most analytes), 30 ms (⁵¹ V), 5 ms (²⁷ Al, ²⁹ Si, ³¹ P, ⁵⁷ Fe)		
Primary standard	NIST 610 glass			
Secondary standard, internal standard isotope	Zircon 91500, ⁹⁰ Zr	Durango apatite, apatite nano-powder pellet (myStandards GmbH), ⁴³ Ca	DJ biotite, ²⁷ Al	BIR-1, BHVO-1, ⁴³ Ca

1547

1548

1549

1550 **Table 3. Trace element partitioning between apatite and glass.**

1551

Element	FCT	SD	MAC2	SD	MAC137	SD	MAC160	SD	TT7	SD
Li	0.07	0.05	0.06	0.01	0.07	0.01	0.14	0.03	-	-
Rb	0.0028	0.0017	0.0006	0.0005	0.0004	0.0002	0.0013	0.0009	0.0110	0.0034
Cs	0.014	0.013	0.003	0.002	0.024	0.006	0.058	0.063	0.014	0.011
Sr	7.0	1.3	6.7	0.6	11.2	1.4	5.2	1.2	4.8	0.3
Ba	0.006	0.004	0.011	0.003	0.199	0.041	0.009	0.004	0.009	0.006
Y	69	22	137	43	77	11	109	39	60	25
La	63	23	55	8	32	5	38	13	38	6
Ce	73	28	76	12	35	6	53	16	45	8
Pr	92	35	94	15	51	9	69	23	63	12
Nd	111	40	119	18	67	13	84	31	83	19
Sm	110	43	140	26	84	17	105	35	95	31
Eu	93	32	19	4	22	4	24	7	45	11
Gd	118	49	191	52	107	21	133	38	106	42
Tb	98	35	172	46	96	17	127	35	89	36
Dy	82	30	163	49	92	16	126	39	75	31
Ho	72	29	149	52	85	15	122	42	65	28
Er	63	22	126	45	71	12	113	44	53	23
Tm	48	19	83	34	50	9	86	38	39	16
Yb	36	14	80	35	37	6	68	33	29	12
Lu	29	12	66	35	31	7	64	33	24	10
Sc	0.08	0.06	0.20	0.07	0.14	0.08	0.26	0.12	-	-
Ti	0.05	0.03	-	-	0.09	0.03	0.05	0.02	0.03	0.01
V	3.2	2.0	0.3	0.2	0.5	0.2	2.1	0.3	6.8	4.4
Mn	4.4	1.4	9.1	1.4	2.5	0.4	6.7	0.8	3.3	0.2
Cu	0.83	0.64	0.39	0.16	-	-	1.47	1.29	0.19	0.09
Zn	0.12	0.10	0.14	0.05	0.07	0.05	0.16	0.05	0.04	0.01
Ga	0.026	0.008	0.010	0.006	0.067	0.017	0.022	0.013	0.039	0.016
Ge	15	7	10	4	8	2	20	8	15	6
As	1.31	0.56	0.06	0.02	0.04	0.01	0.20	0.09	1.58	0.29
In	-	-	0.13	0.03	-	-	-	-	-	-
Sn	0.34	0.24	0.04	0.02	0.04	0.01	0.12	0.03	0.14	0.02
Pb	0.13	0.04	0.22	0.05	0.15	0.03	0.68	0.54	0.11	0.01
Bi	0.38	0.19	0.28	0.30	0.08	0.05	1.07	1.00	0.39	0.22
Zr	0.020	0.015	0.014	0.007	0.024	0.006	0.012	0.011	0.021	0.012
Nb	0.052	0.049	0.009	0.011	-	-	0.010	0.006	0.010	0.007
Hf	0.022	0.024	0.020	0.014	0.013	0.013	0.013	0.013	0.010	0.007
Ta	0.0090	0.0097	0.0056	0.0057	0.0076	0.0095	0.0037	0.0012	0.0092	0.0042
W	0.021	0.046	0.004	0.004	0.012	0.006	0.018	0.011	0.024	0.009
Th	2.6	1.3	1.2	0.7	1.1	0.3	1.1	1.0	1.6	0.9
U	1.7	1.1	6.9	4.9	1.7	0.5	7.1	5.9	1.5	0.8

1552

1553

1554 **Table 4.** Trace element partitioning between biotite and glass.

1555

Element	FCT	1 σ	MAC2	1 σ	MAC137	1 σ	MAC160	1 σ	TT	1 σ	TT7	1 σ
Li	0.72	0.38	0.15	0.05	0.12	0.05	0.57	0.18	0.23	0.21	0.14	0.13
Rb	1.1	0.3	1.6	0.2	1.8	0.6	1.6	0.2	1.5	0.2	1.7	0.3
Cs	0.31	0.09	0.40	0.12	0.40	0.20	0.89	0.77	0.72	1.06	0.48	0.21
Sr	-	-	0.14	0.07	0.42	0.57	0.22	0.03	0.09	0.01	0.11	0.01
Ba	2.5	0.9	2.4	1.8	8.4	10.0	7.9	2.1	5.8	2.6	6.5	1.8
Y	0.011	0.003	0.022	0.009	0.050	0.100	0.054	0.044	0.017	0.014	0.010	0.006
La	0.001	0.000	0.006	0.004	0.023	0.048	0.016	0.026	0.008	0.014	0.003	0.006
Eu	0.235	0.076	0.379	0.173	1.020	1.073	0.743	0.179	0.310	0.116	0.310	0.077
Gd	0.045	0.030	0.050	0.031	0.081	0.205	0.082	0.113	0.082	0.036	0.013	0.017
Sc	1.2	0.4	3.5	0.7	6.7	2.5	5.9	1.7	1.9	0.2	2.4	0.3
V	54	14	253	109	515	255	586	85	146	39	190	25
Mn	7.1	2.1	2.7	0.6	3.3	1.1	3.2	0.3	5.3	0.4	4.9	0.6
Co	177	66	93	35	73	28	77	19	92	34	106	19
Ni	-	-	77	31	130	96	68	7	-	-	-	-
Cu	1.8	1.7	4.1	4.4	6.7	6.9	9.3	6.2	0.3	0.1	1.1	0.6
Zn	14.7	4.0	8.8	1.9	11.1	3.9	8.8	1.1	9.0	0.8	9.6	1.4
Mo	0.09	0.03	-	-	1.66	1.21	2.03	-	0.35	0.10	0.42	0.09
Ga	3.8	1.3	2.1	0.5	4.0	2.3	4.2	1.6	4.8	2.1	3.9	0.9
Ge	0.7	0.3	-	-	0.9	0.3	-	-	0.7	0.2	0.7	0.3
Cd	-	-	-	-	-	-	-	-	-	-	-	-
In	2.7	1.6	0.9	0.4	1.3	0.6	2.1	0.7	2.5	0.8	2.7	0.9
Sn	0.93	0.61	0.10	0.05	0.15	0.07	0.24	0.07	0.80	0.10	0.81	0.20
Pb	0.06	0.02	0.14	0.04	0.11	0.03	0.20	0.04	0.07	0.01	0.08	0.01
Bi	0.06	0.03	0.26	0.08	0.24	0.09	0.29	0.11	0.30	-	-	-
Zr	0.04	0.01	0.07	0.03	0.09	0.09	0.12	0.02	0.07	0.01	0.08	0.01
Nb	2.3	0.6	6.4	1.8	7.4	3.8	4.4	1.6	5.0	0.7	5.4	0.7
Hf	-	-	-	-	0.12	0.08	0.13	0.05	-	-	0.08	0.01
Ta	0.7	0.2	2.3	0.9	2.3	1.3	1.4	0.7	1.5	0.3	1.4	0.3
W	0.02	0.01	0.13	0.03	0.12	0.07	0.06	0.04	0.02	0.01	0.03	0.01

1556

1557

1558 **Table 5.** Trace element partitioning between apatite and biotite.

	FCT		MAC2		MAC137		MAC160		MM		PAL		TT7	
	Mean	SD	Mean	SD	Mean	SD	Mean	SD	Mean	SD	Mean	SD	Mean	SD
Li	0.091	0.057	0.410	0.135	0.541	0.226	0.242	0.084	0.405	0.370	0.021	0.009	-	-
Rb	0.00249	0.00135	0.00038	0.00031	0.00023	0.00012	0.00077	0.00054	0.13001	0.14160	0.00003	0.00001	-	-
Cs	0.04472	0.04127	0.00650	0.00487	0.06030	0.03014	0.06569	0.06254	0.32989	0.23581	0.00002	0.00002	0.02844	0.02525
Sr	-	-	48	25	27	36	24	6	35	11	384	423	43	4
Ba	0.0026	0.0017	0.0047	0.0036	0.0238	0.0287	0.0012	0.0006	0.0462	0.0681	0.0003	0.0001	0.0013	0.0009
Co	0.009	0.009	0.019	0.004	0.010	0.005	0.008	0.003	0.037	0.036	0.034	0.011	0.009	0.007
Ni	0.037	0.020	0.007	0.007	0.015	0.010	0.011	0.008	0.004	0.004	0.032	0.018	-	-
Zn	0.008	0.006	0.016	0.005	0.006	0.005	0.018	0.006	0.279	0.252	0.002	0.002	0.004	0.001
Pb	2.4	0.3	1.6	0.5	1.3	0.3	3.5	2.8	-	-	15.8	7.4	1.4	0.1
Y	6455	1978	6221	3010	1542	3089	2030	1817	273	302	675	1423	5863	4002
La	125374	74029	9432	6550	1370	2813	2318	3813	247	501	1159	3180	11555	21539
Gd	2613	1634	3840	2401	1322	3328	1621	2269	515	726	425	513	8272	11560
Sc	0.06	0.05	0.06	0.02	0.02	0.01	0.04	0.02	0.26	0.18	0.02	0.01	-	-
Ga	0.007	0.001	0.0048	0.003	0.017	0.010	0.0051	0.003	0.073	0.085	0.00170	0.001	0.010	0.005
In	-	-	0.16	0.05	-	-	-	-	-	-	0.45	0.41	-	-
Bi	6.3	3.8	1.1	1.2	0.3	0.2	3.6	3.6	7.4	13.2	77.1	41.0	-	-
Ge	20.6	6.2	-	-	9.1	2.6	-	-	11.2	4.5	18.8	7.0	20.4	6.3
Zr	0.49	0.34	0.20	0.13	0.27	0.26	0.11	0.10	3.83	6.31	0.33	1.43	0.27	0.15
Hf	-	-	-	-	0.11	0.14	0.09	0.10	3.44	5.37	0.12	0.29	0.13	0.09
Th	2337	2370	180	219	99	252	94	184	50	102	469	942	3487	4715
Si	-	-	-	-	0.005	0.001	0.008	0.002	0.093	0.131	0.003	0.001	0.021	0.015
Ti	-	-	-	-	0.0018	0.0007	0.0014	0.0007	0.0338	0.0577	-	-	0.0007	0.0002
Nb	0.022	0.021	0.001	0.002	-	-	0.002	0.002	1.288	1.772	0.009	0.006	0.002	0.001
Ta	0.013	0.014	0.002	0.003	0.003	0.005	0.003	0.002	1.118	1.249	0.002	0.003	0.006	0.003
P	-	-	-	-	2513	1986	2344	2586	2804	2521	975	2419	-	-
Eu	396	126	51	22	21	22	33	12	123	43	101	49	144	48
V	0.0589	0.0326	0.0013	0.0008	0.0009	0.0005	0.0037	0.0005	0.5468	0.2493	0.1858	0.0530	0.0358	0.0227
Mn	0.62	0.08	3.32	0.62	0.78	0.26	2.08	0.26	1.08	0.36	0.44	0.11	0.68	0.07
Cu	0.46	0.38	0.09	0.10	-	-	0.16	0.12	0.36	0.31	0.21	0.32	0.18	0.12
Sn	0.37	0.10	0.34	0.22	0.24	0.14	0.52	0.17	0.80	0.41	0.46	0.17	0.17	0.04
W	1.41	3.17	0.03	0.03	0.10	0.08	0.32	0.29	4.13	6.84	47.54	59.22	0.72	0.35

1559

1560

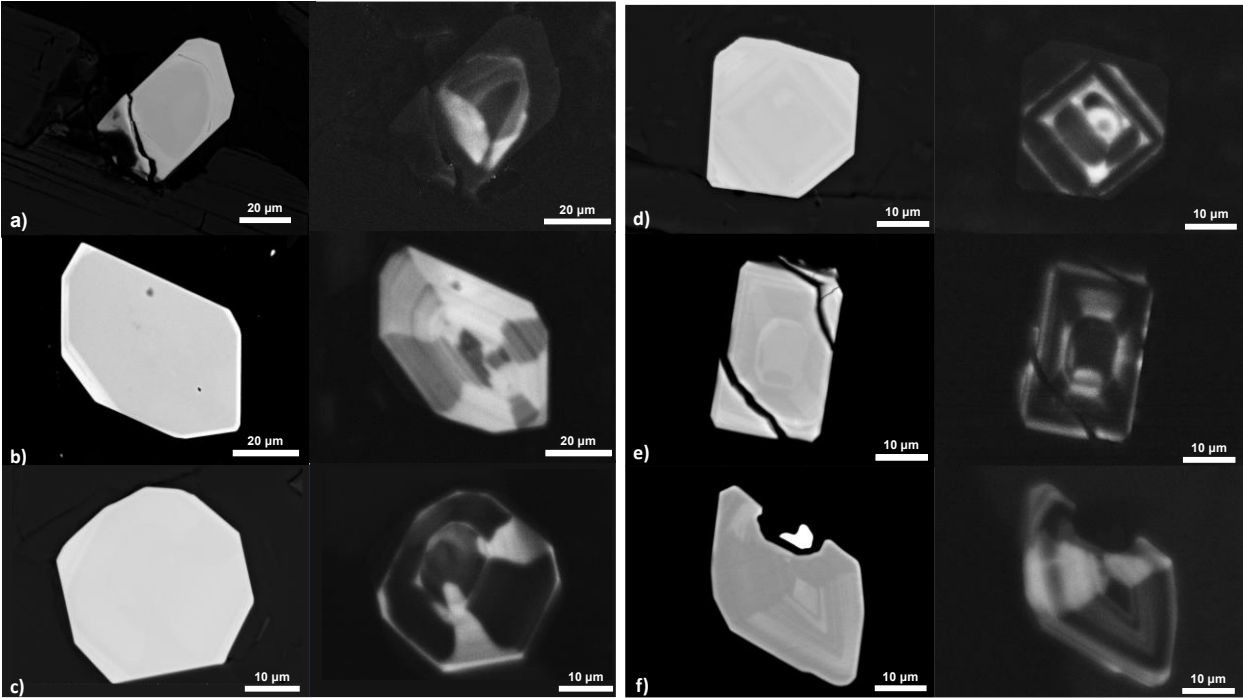
Table 6. $D(V)^{ap/bt}$ values used for the vanadium species in the partitioning model.

V species	D surrogate	D value
V^{3+}	Minimal $D(Ga^{3+})$	0.0048
V^{4+}	Mean $D(Ti^{4+})$	0.0004
V^{5+}	Least squares fitting	0.1651

1561

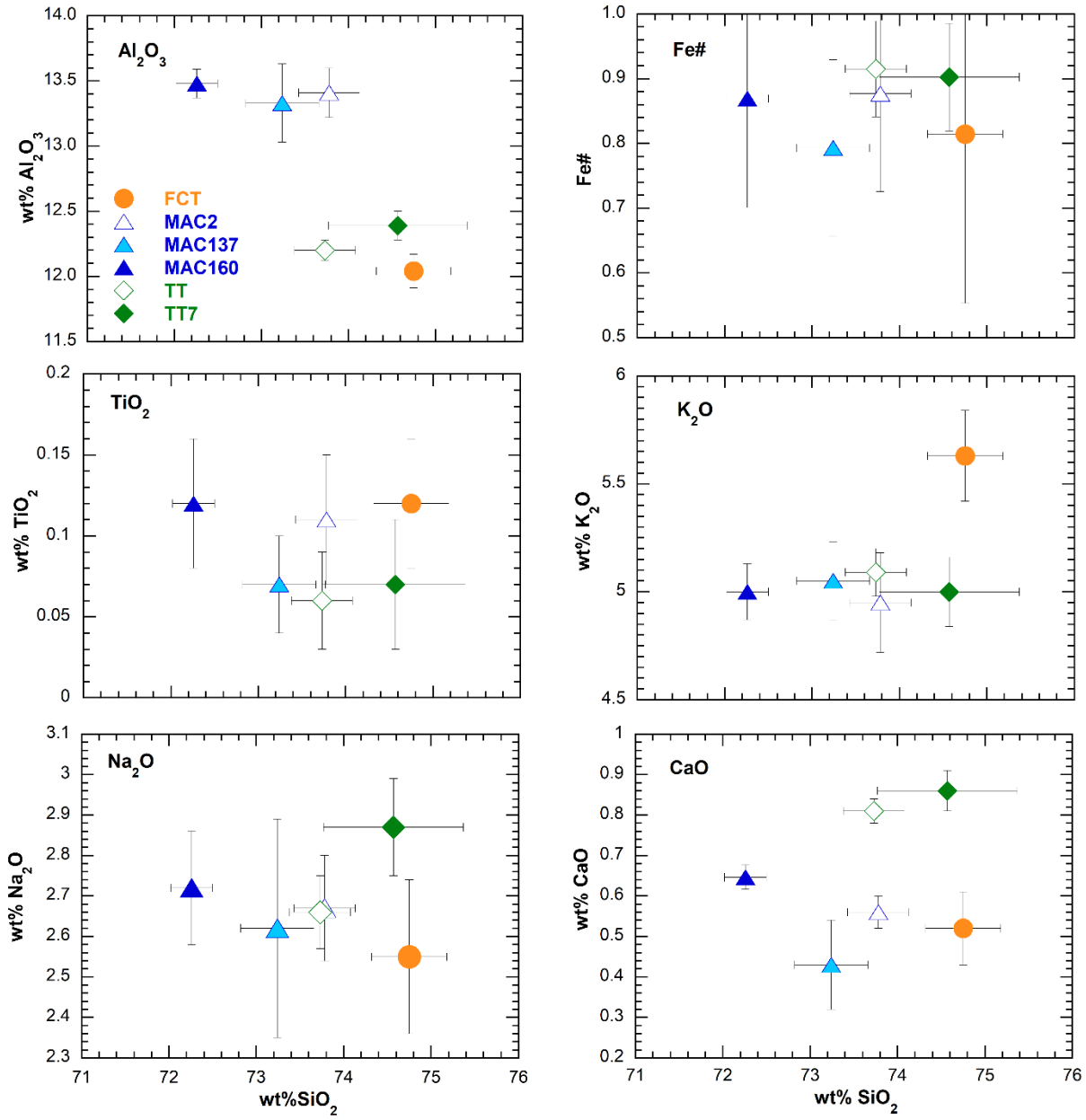
1562

Supplementary figures



1564

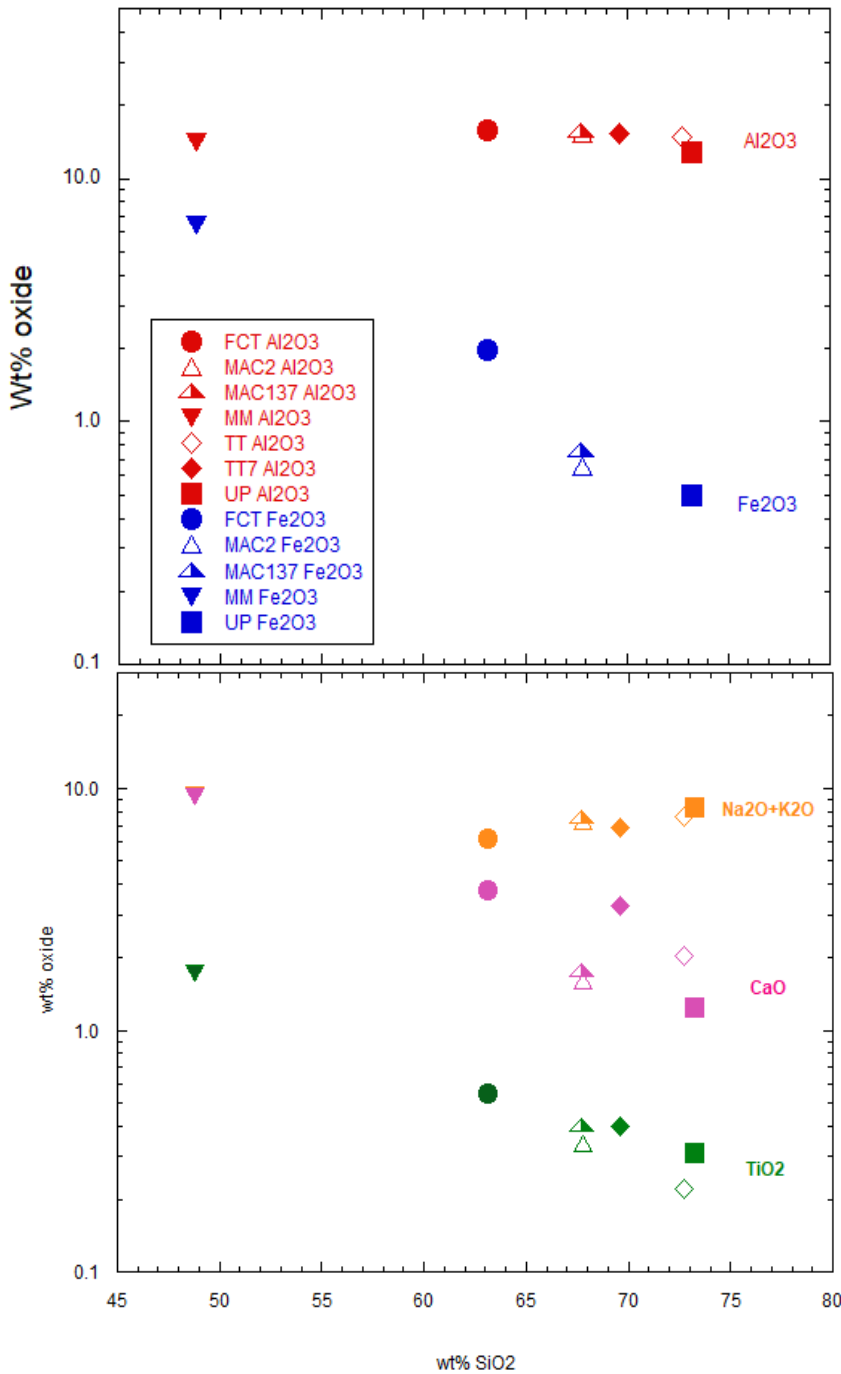
1565 **Supplementary Figure S1.** Examples of Macusani zircon textures in BSE (left) and
 1566 cathodoluminescence (CL) images: a) MAC137.1_zr03, b) MAC137.1_zr04, c) MAC137.3_zr03, d)
 1567 MAC137.3_zr04, e) MAC160.1_zr01, f) MAC160.1_zr03. The zircons are typically small (<50 μm),
 1568 euhedral, and exhibit well-developed, concentric growth zoning, typical to igneous zircon (Corfu et
 1569 al., 2003). Few crystals, e.g. S1a, contain an inherited core.



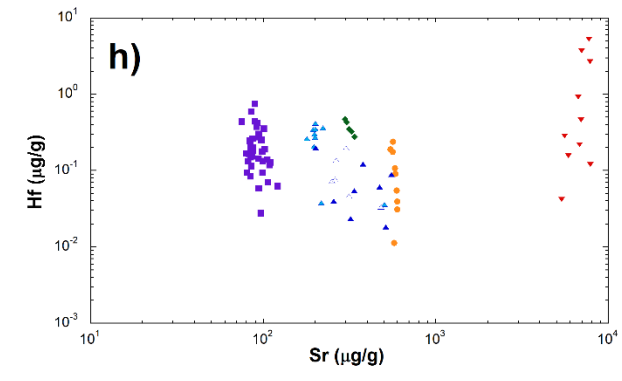
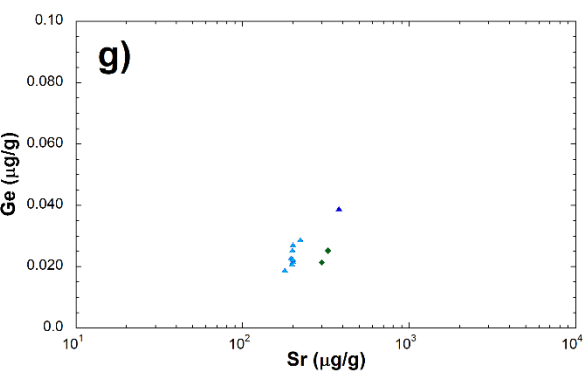
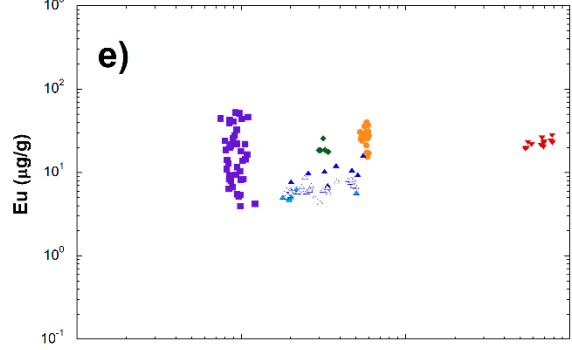
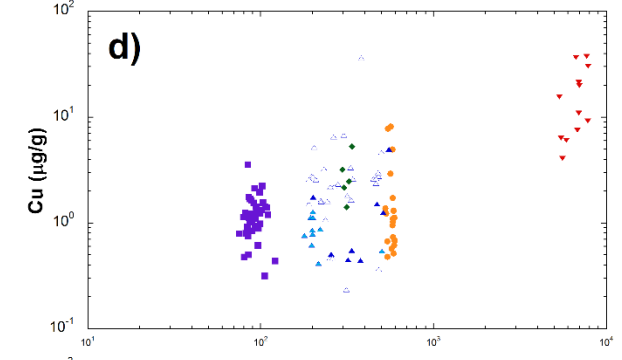
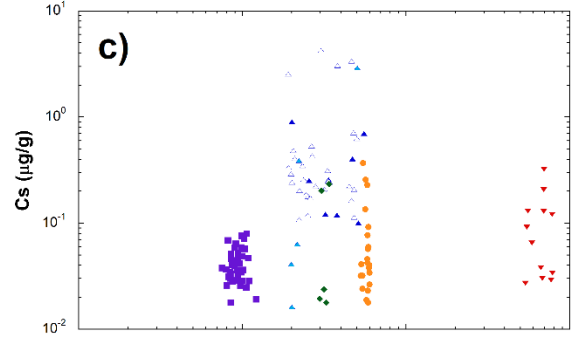
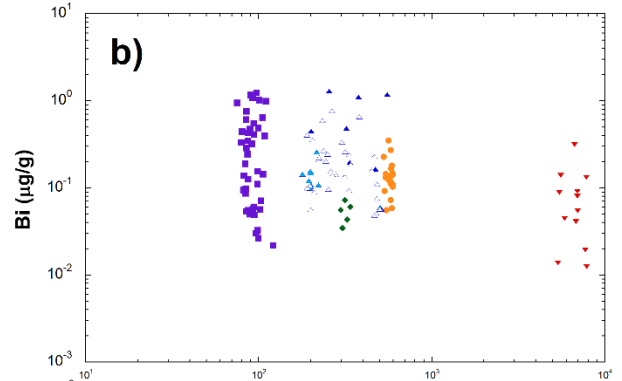
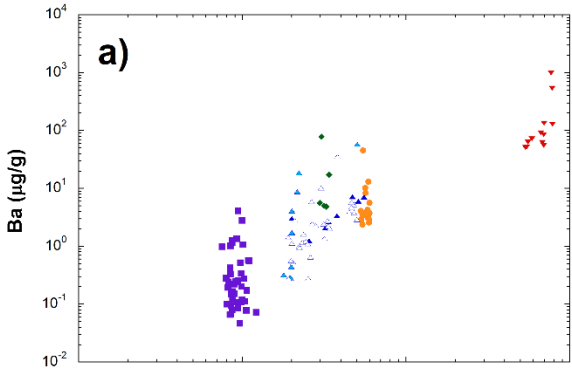
1570

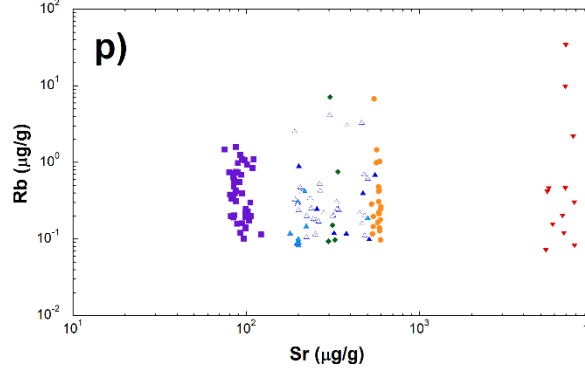
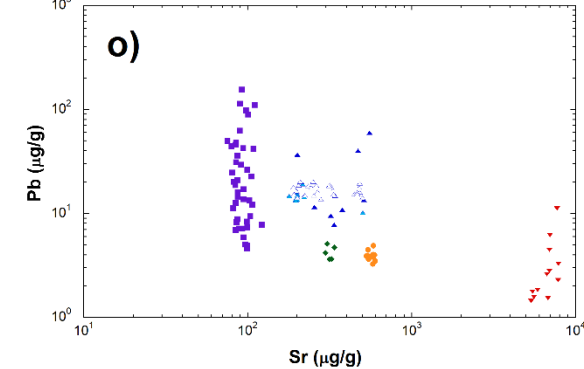
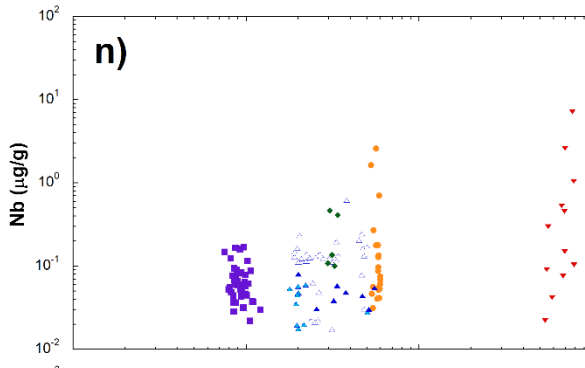
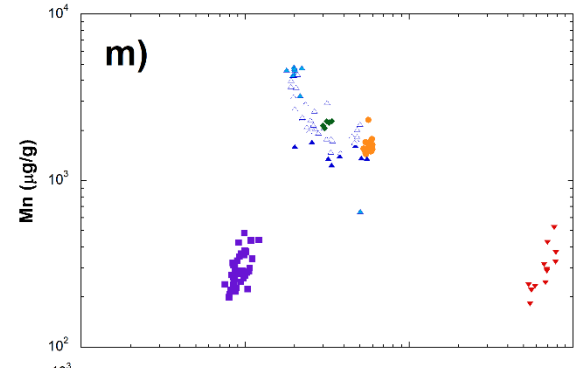
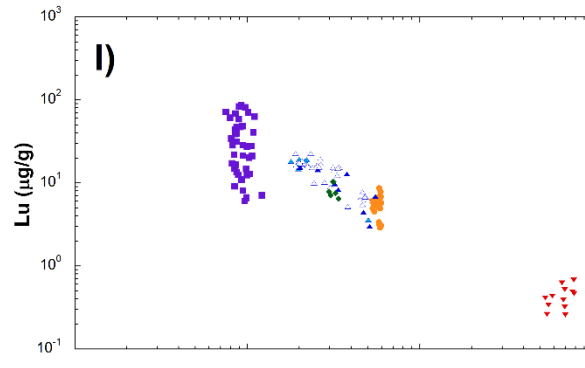
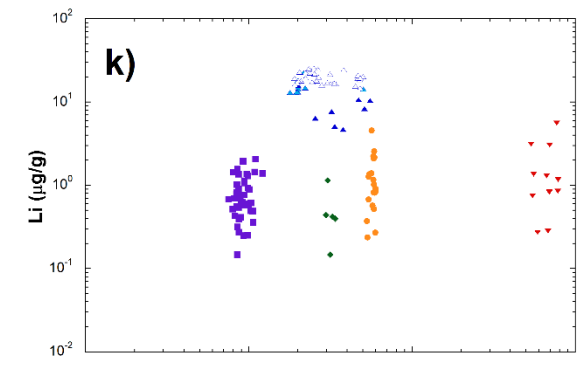
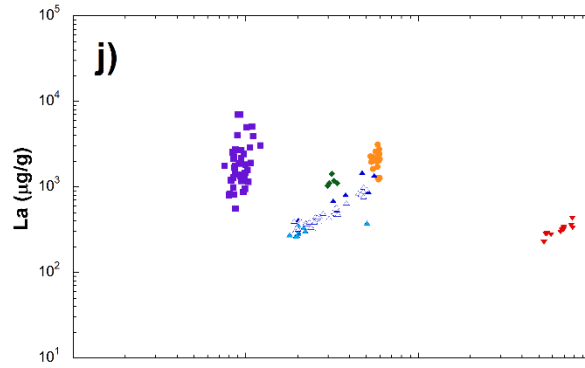
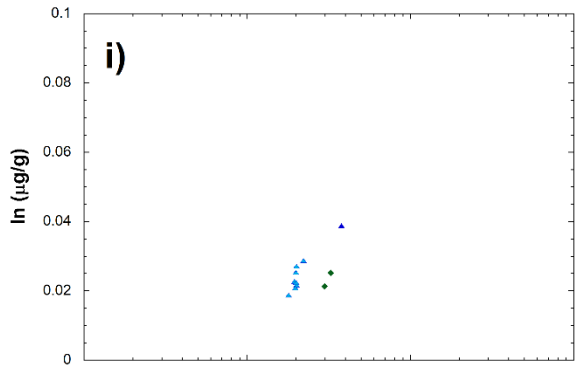
1571 **Supplementary Figure S2.** Major element composition of the glass suite.

1572



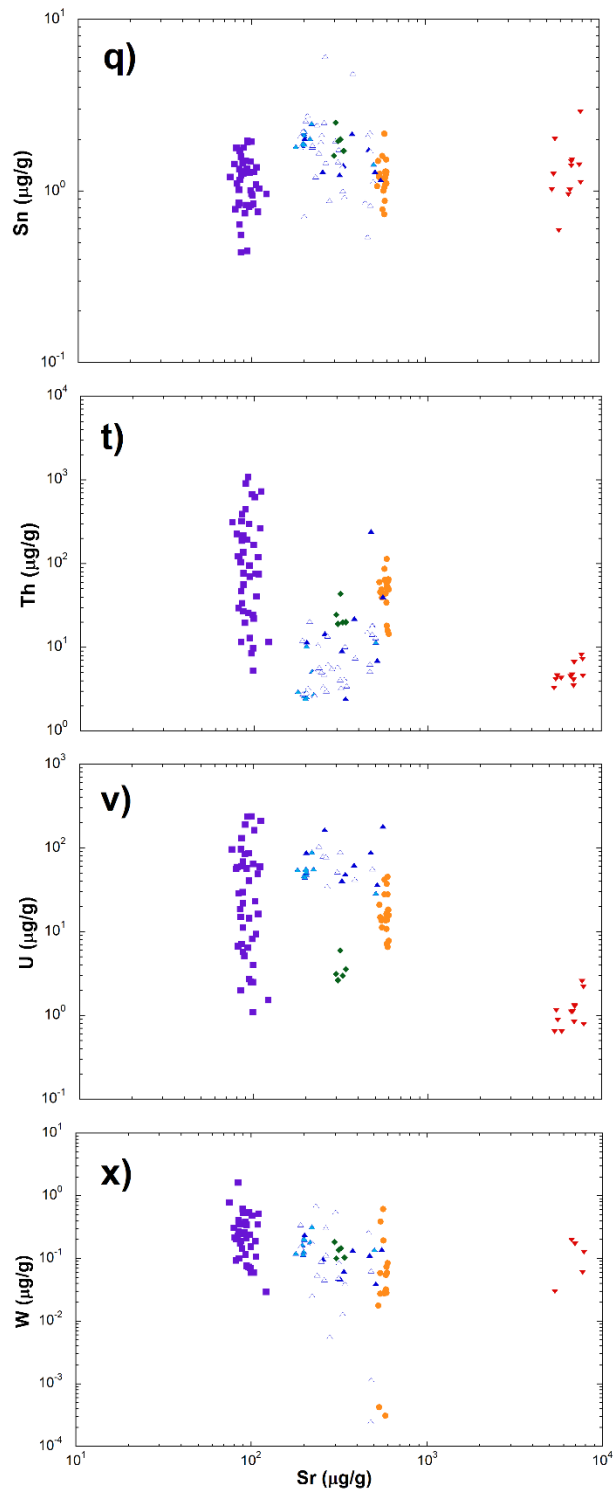
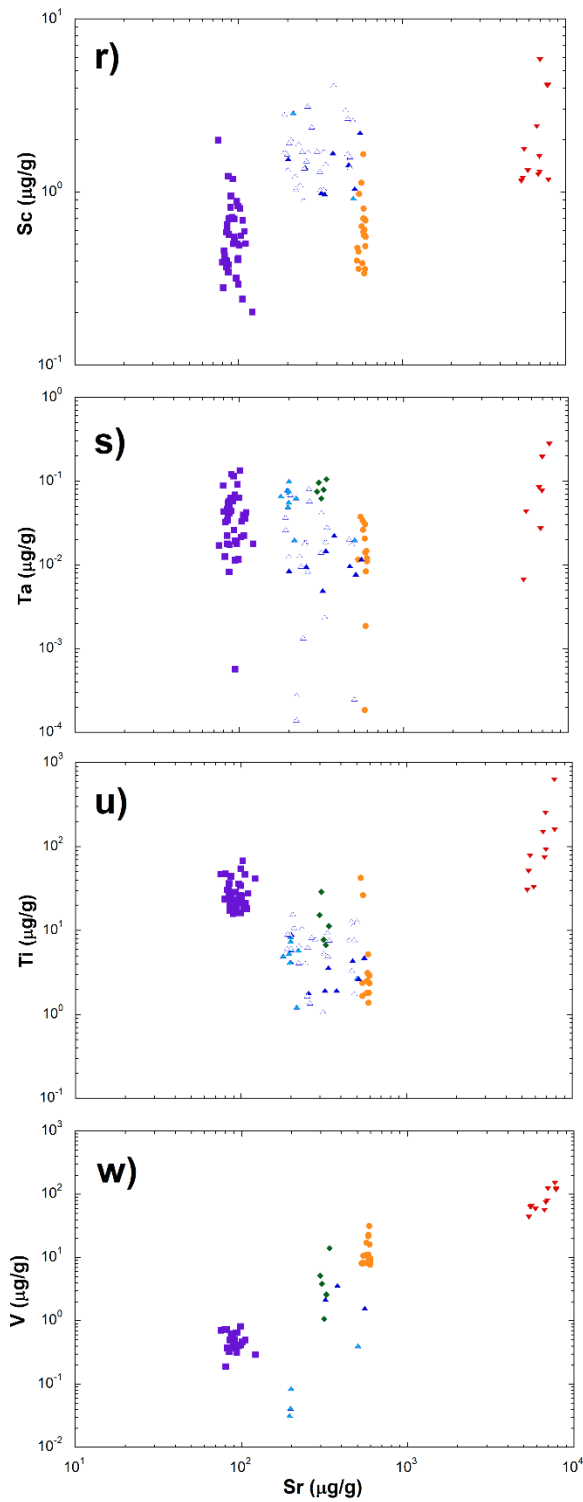
Supplementary Figure S3. Whole rock reported major element composition: FCT from Whitney & Stormer (1985), MAC2 and M137 from Sandeman & Clark (2003), MM from Carmichael et al. (1996), TT7 from Chesner et al. (2020), UP from Emslie & Stirling (1993). Composition of the sample TT is assumed to be the same as TT5 of Chesner et al. (2020), due to the proximity of the locations of the two sampling sites.





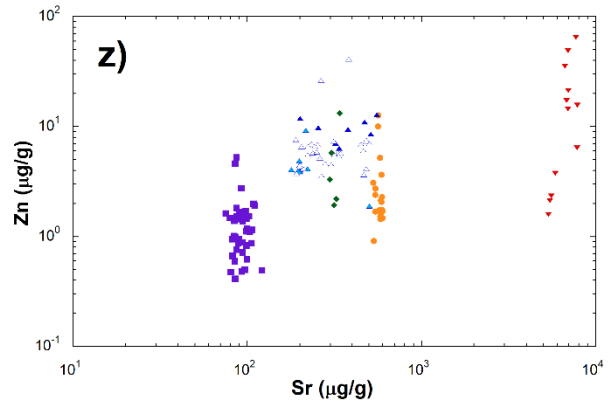
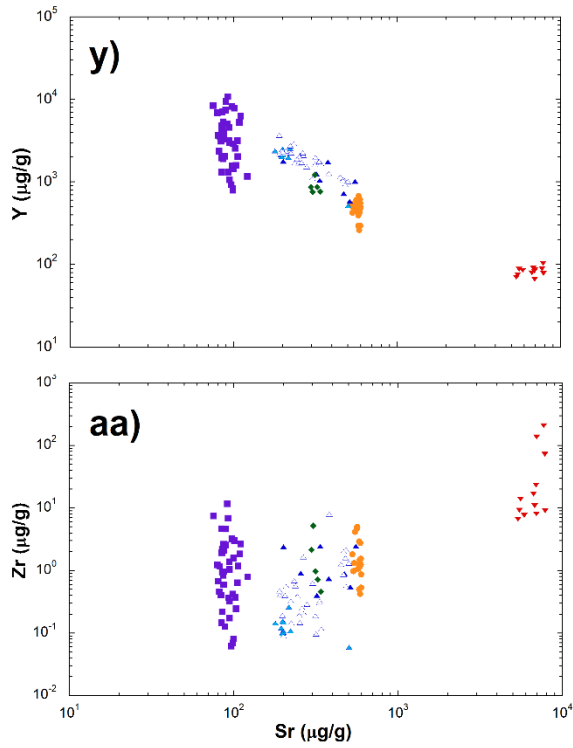
1604

1605



1606

1607



1608

1609 **Supplementary Figure S4.** Apatite trace element composition. Symbols from Fig. 8.

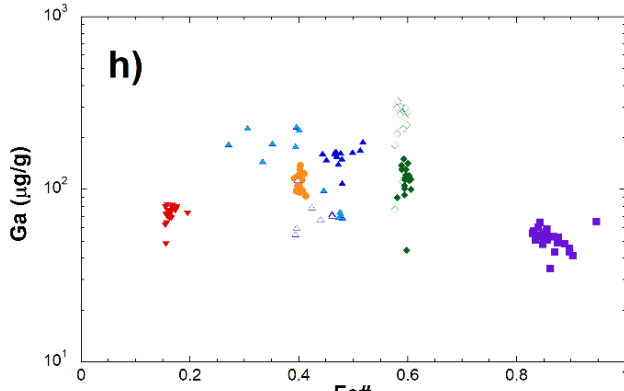
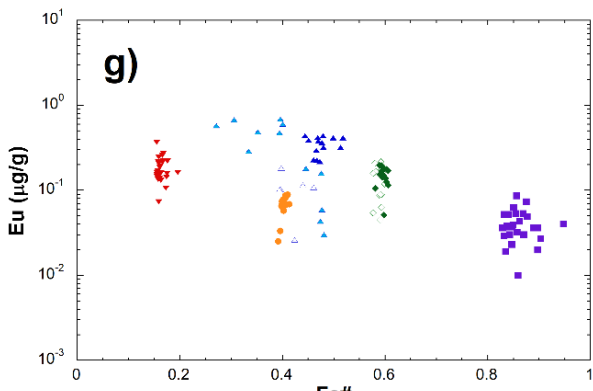
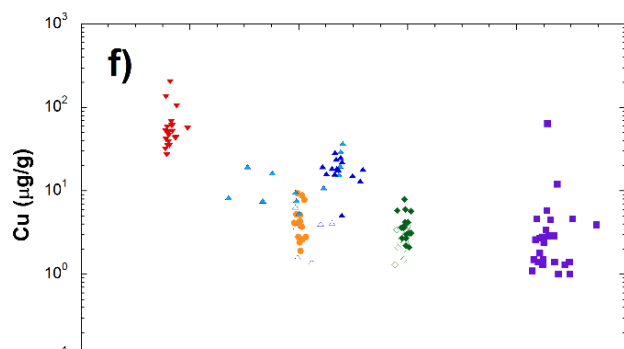
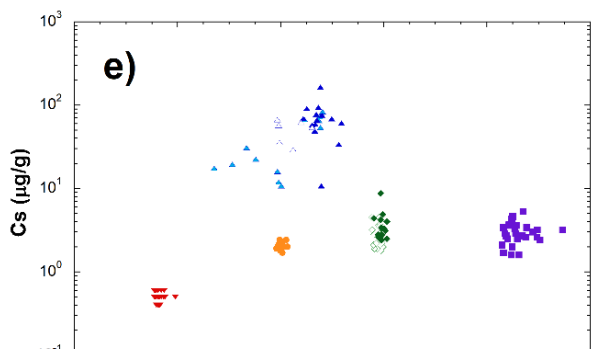
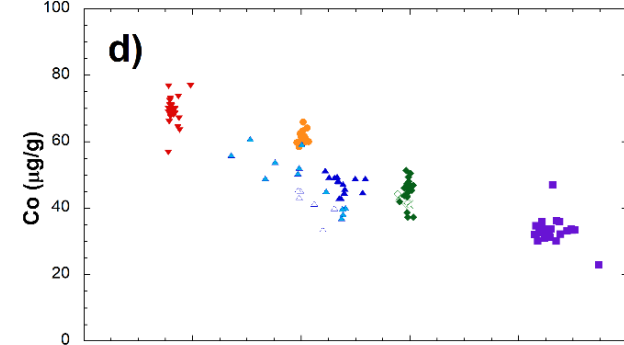
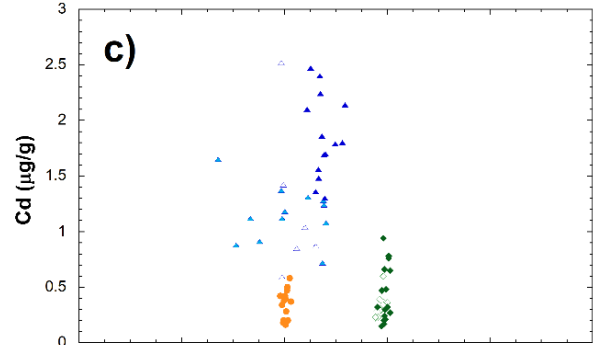
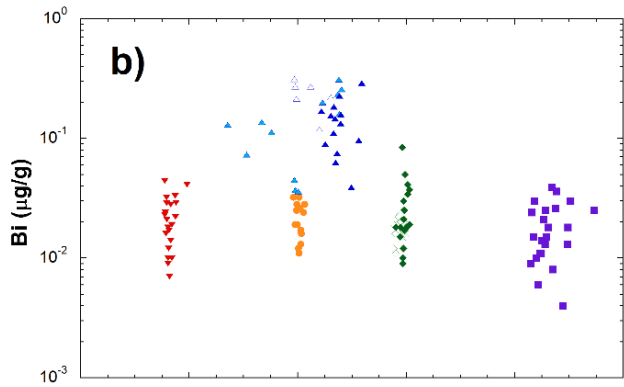
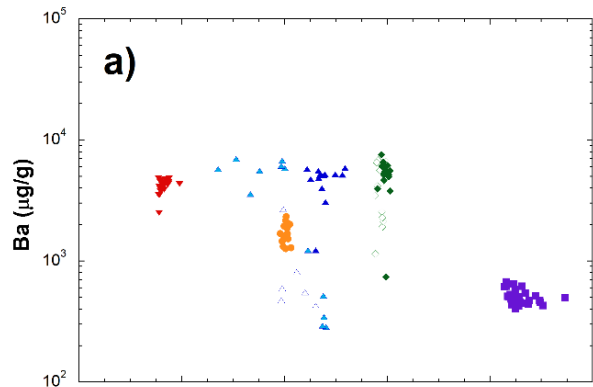
1610

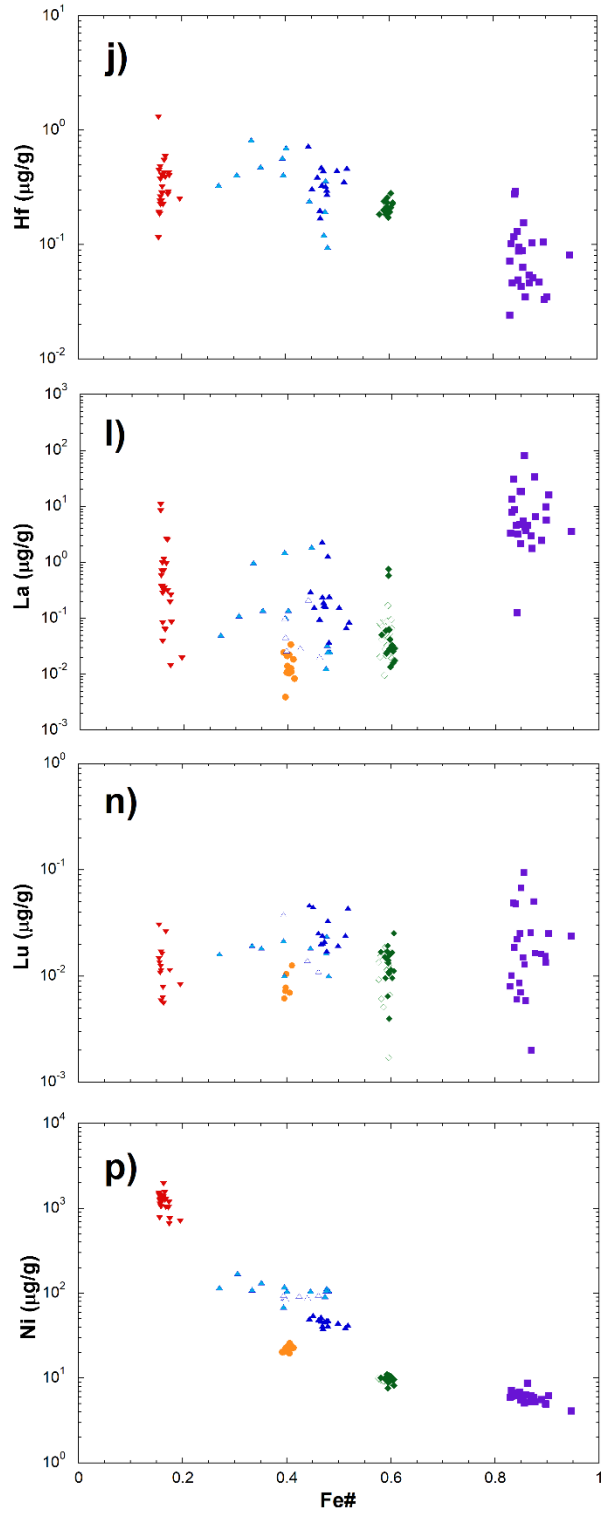
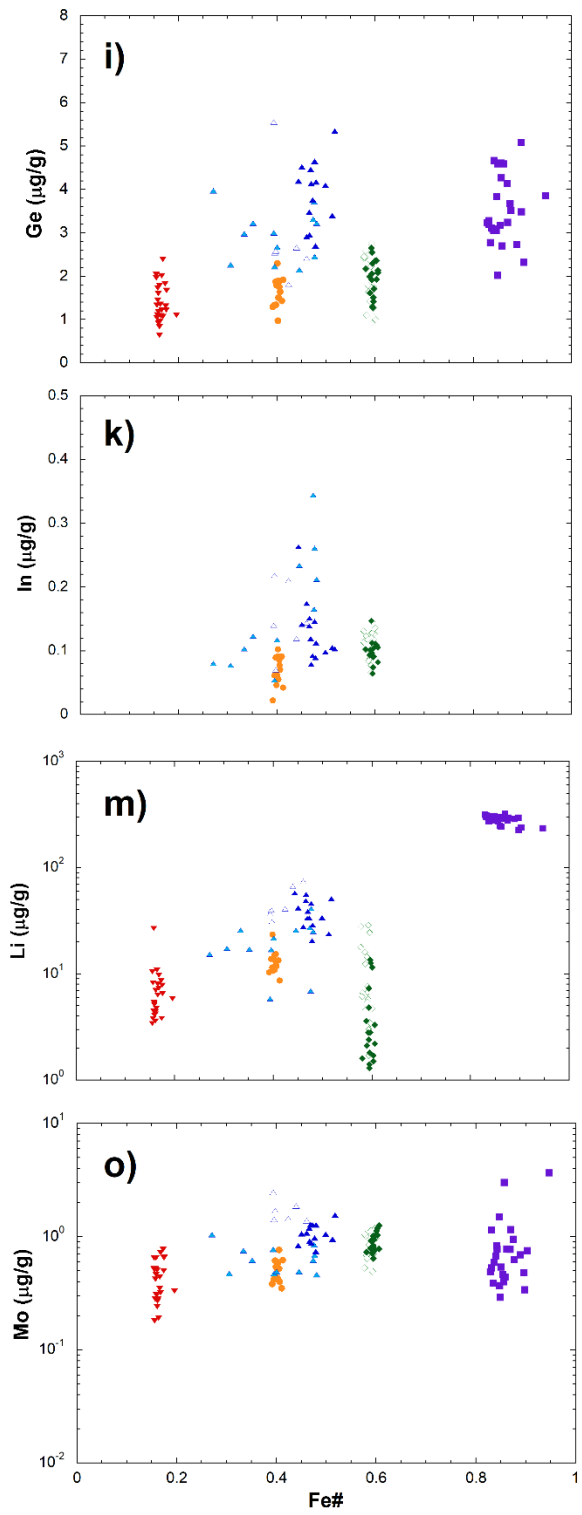
1611

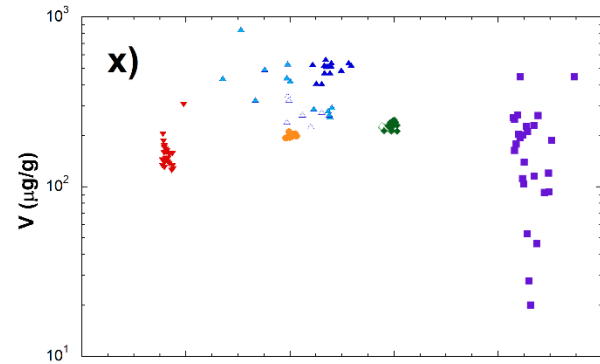
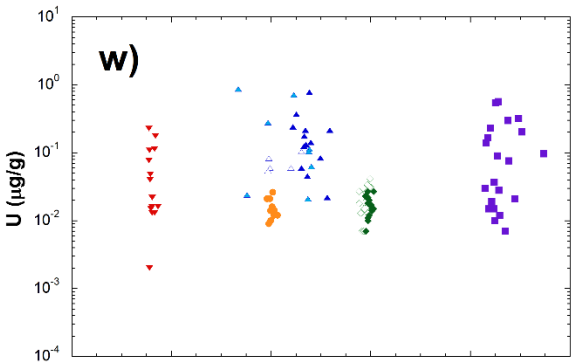
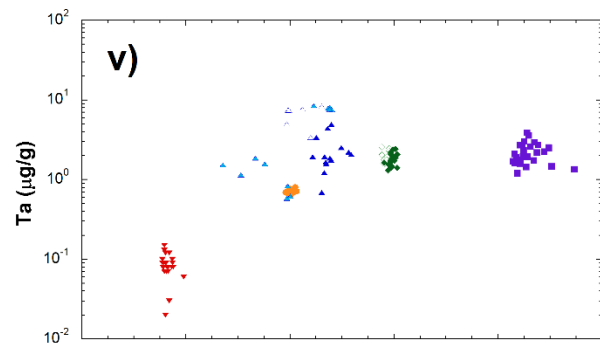
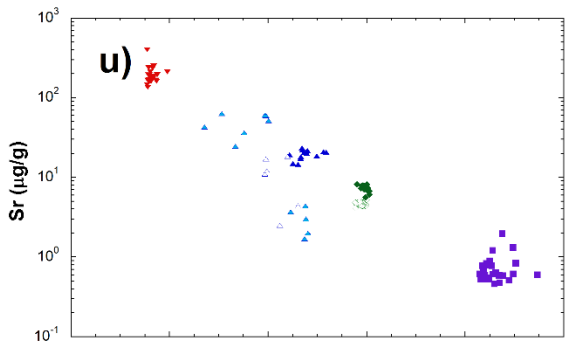
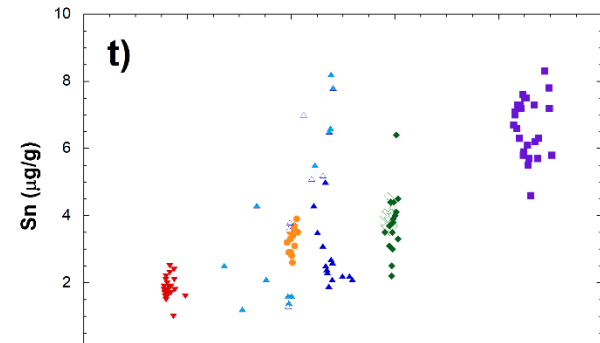
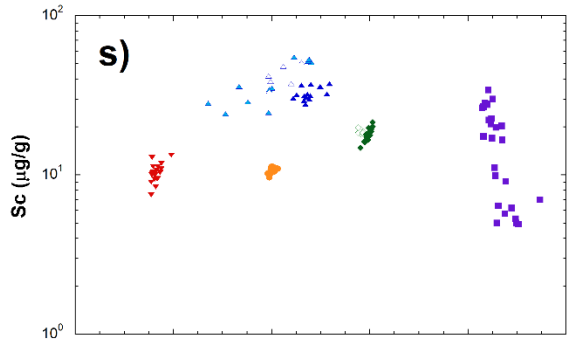
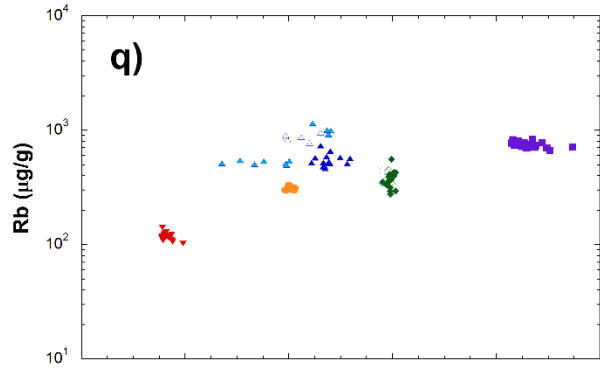
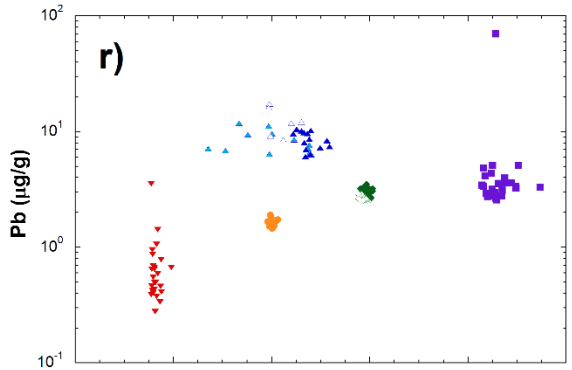
1612

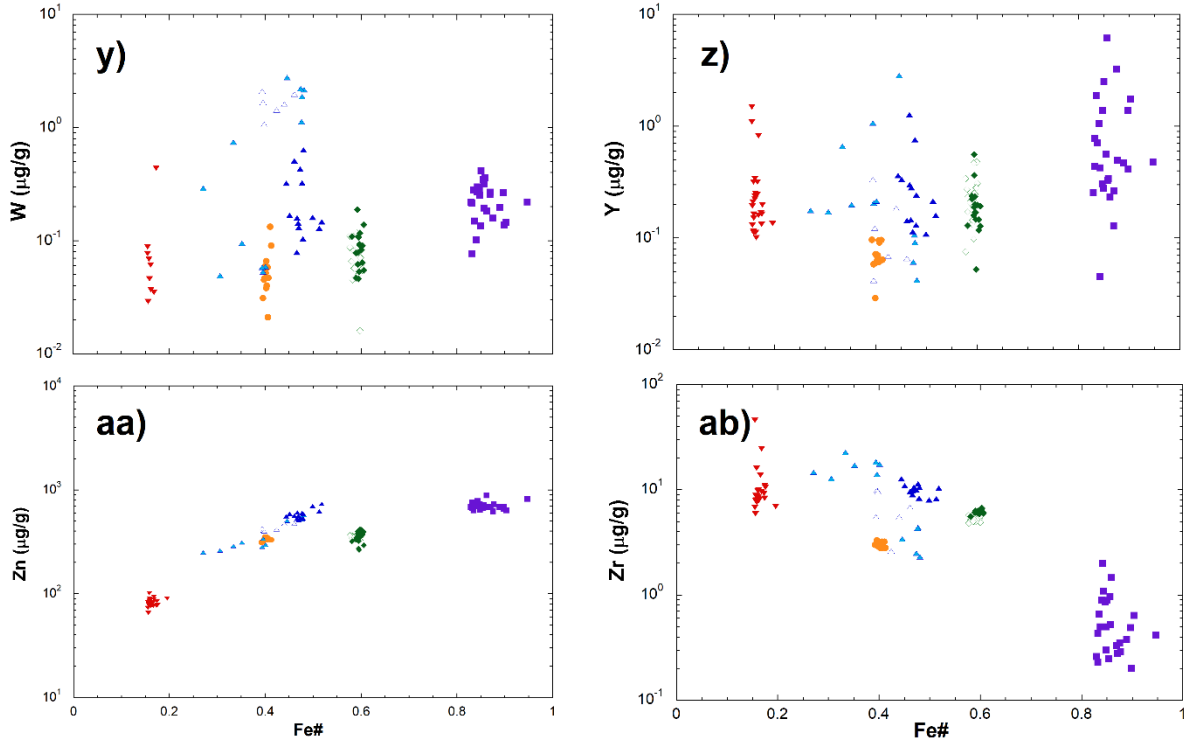
1613

1614







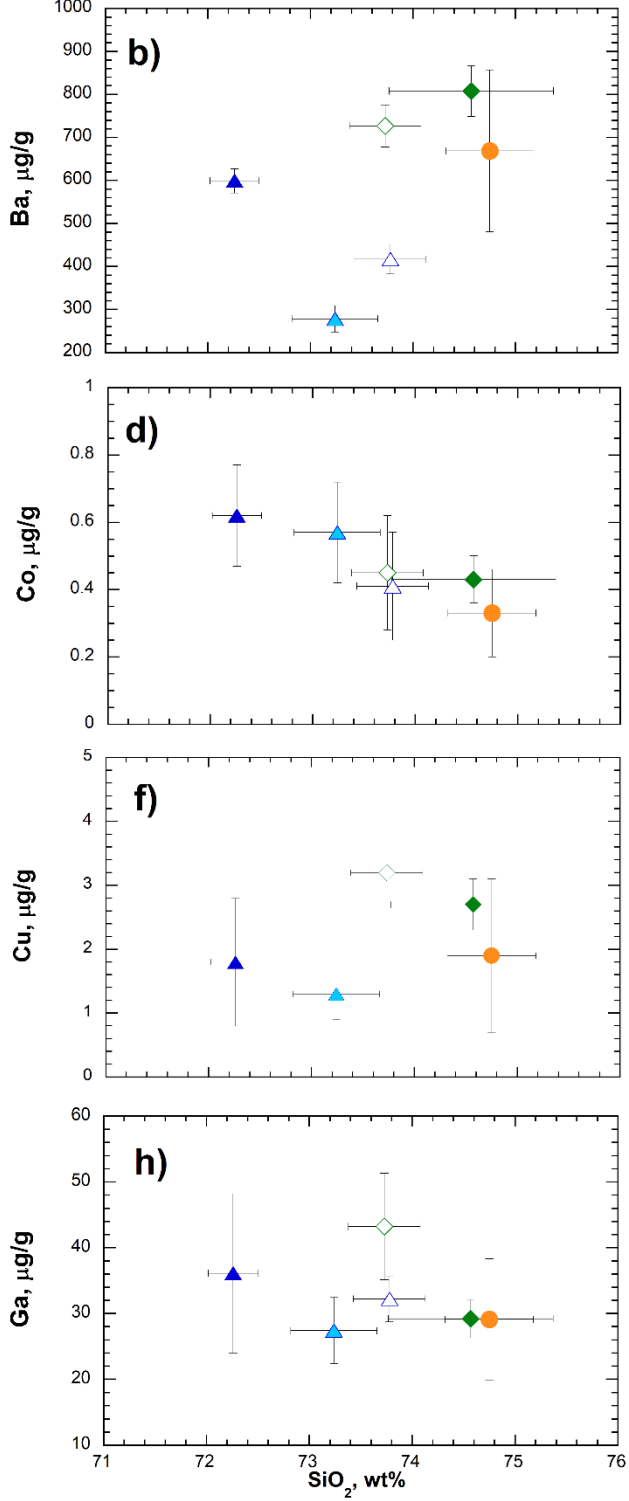
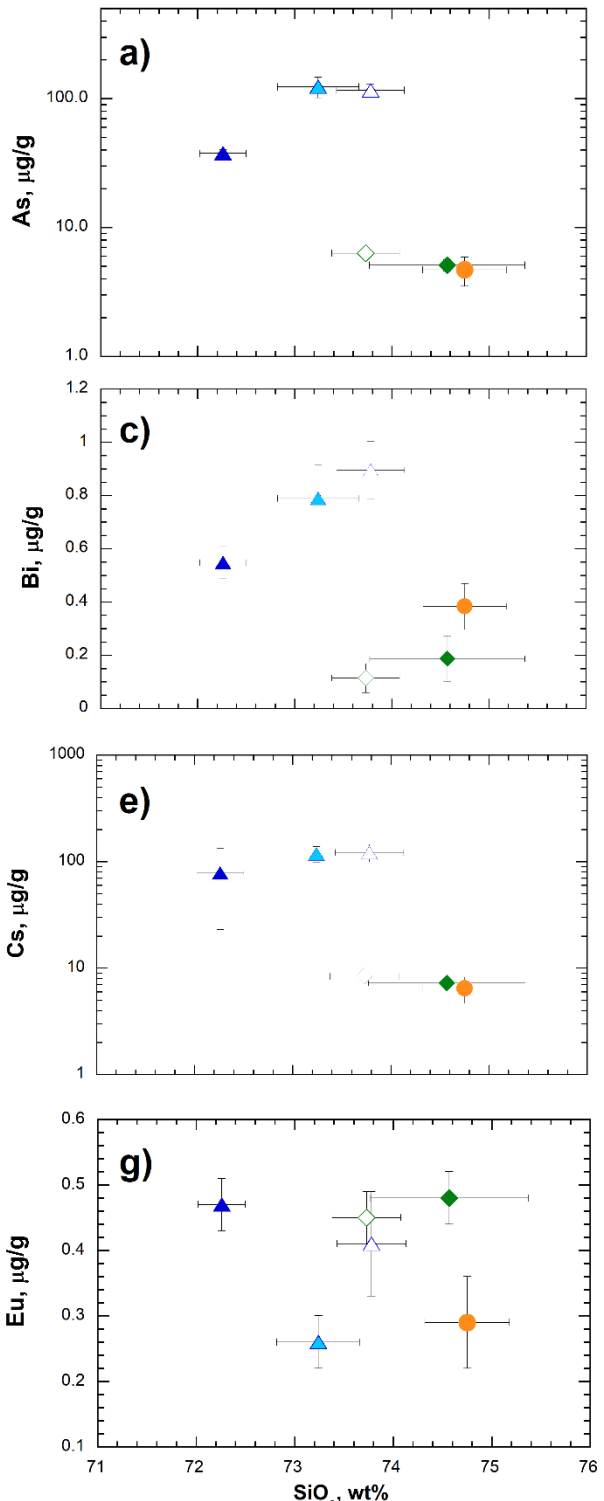


1620

1621 **Supplementary Figure S5.** Biotite trace element composition. Symbols from Fig. 8.

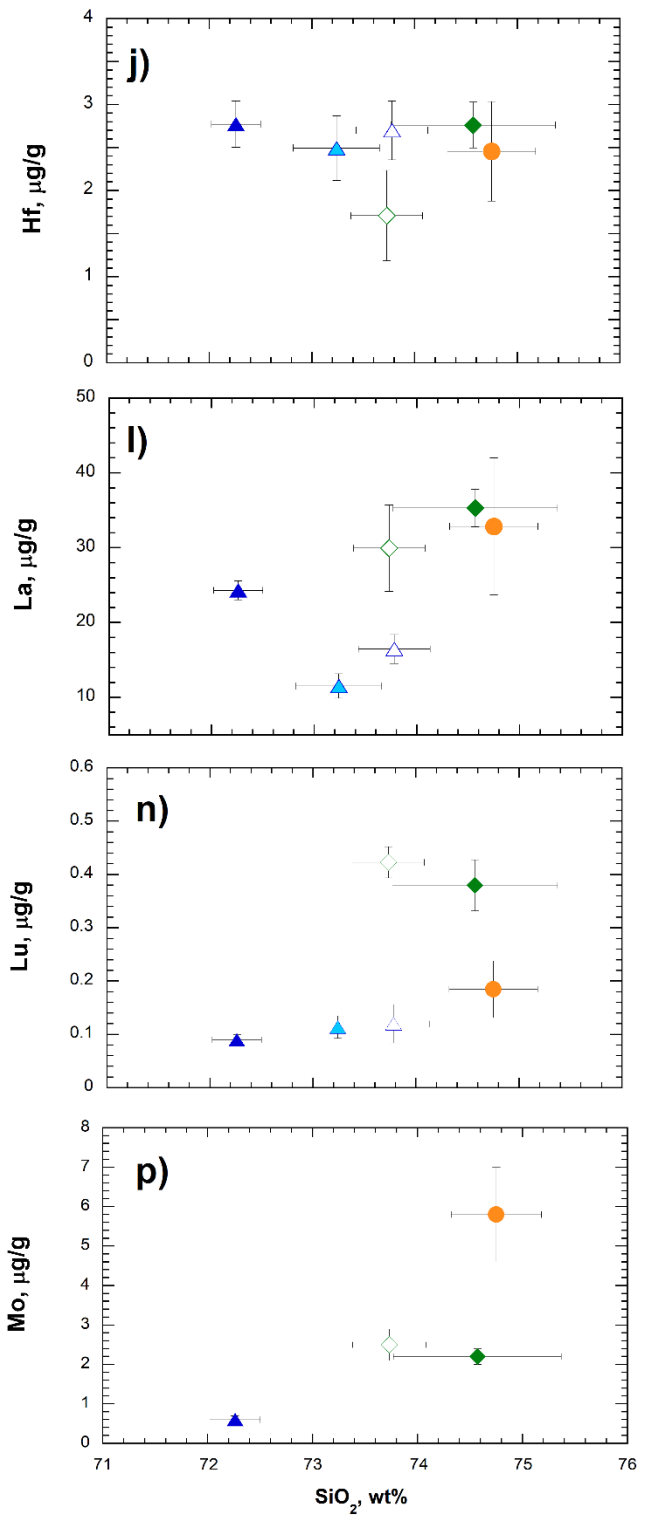
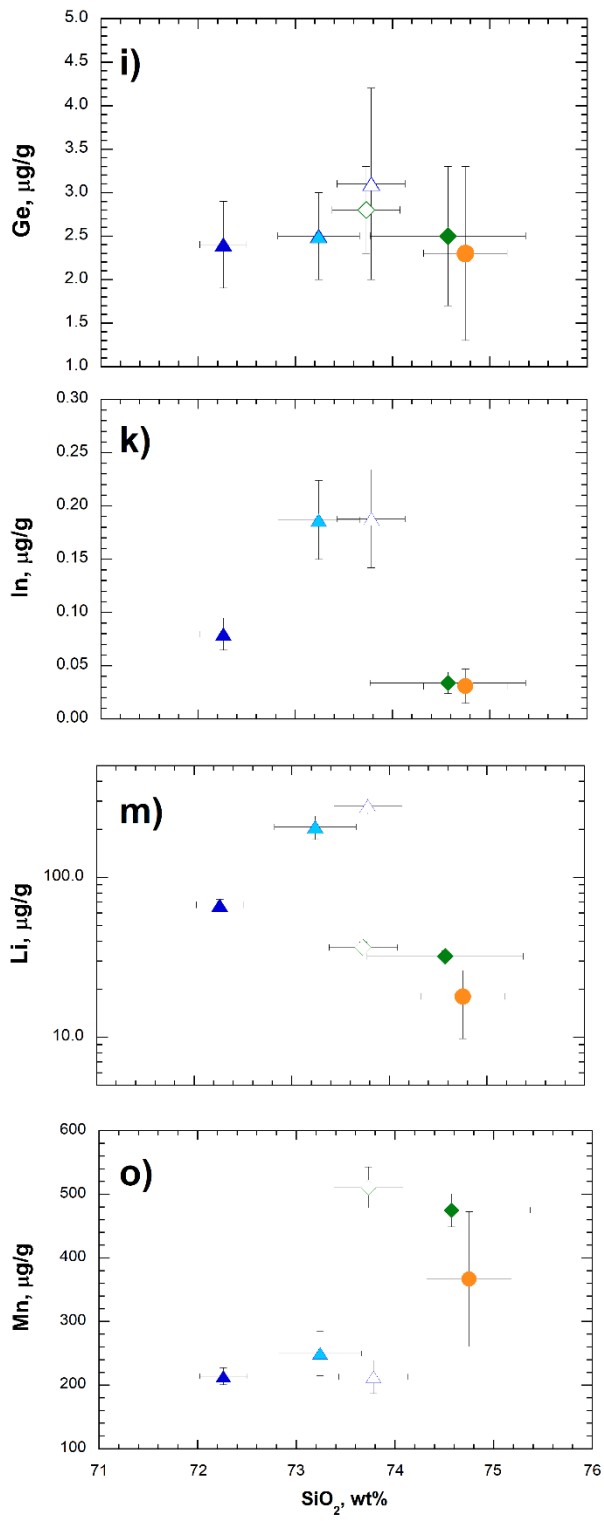
1622

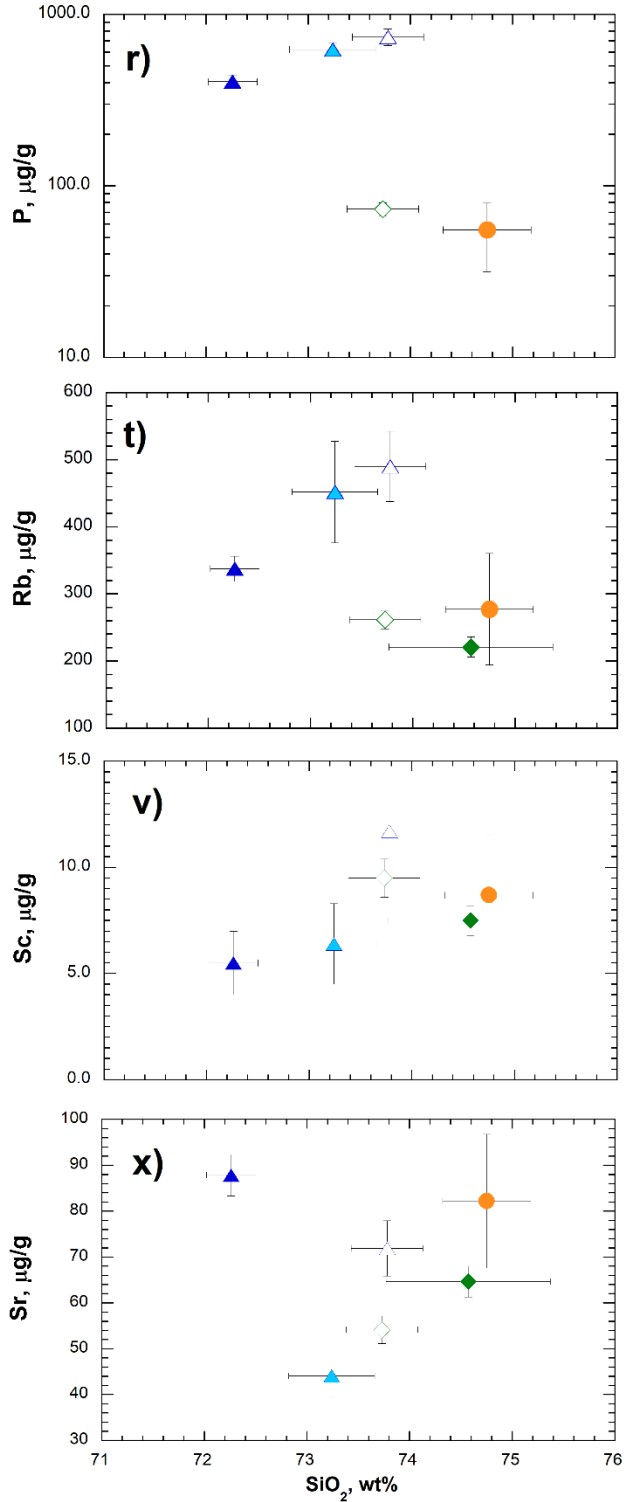
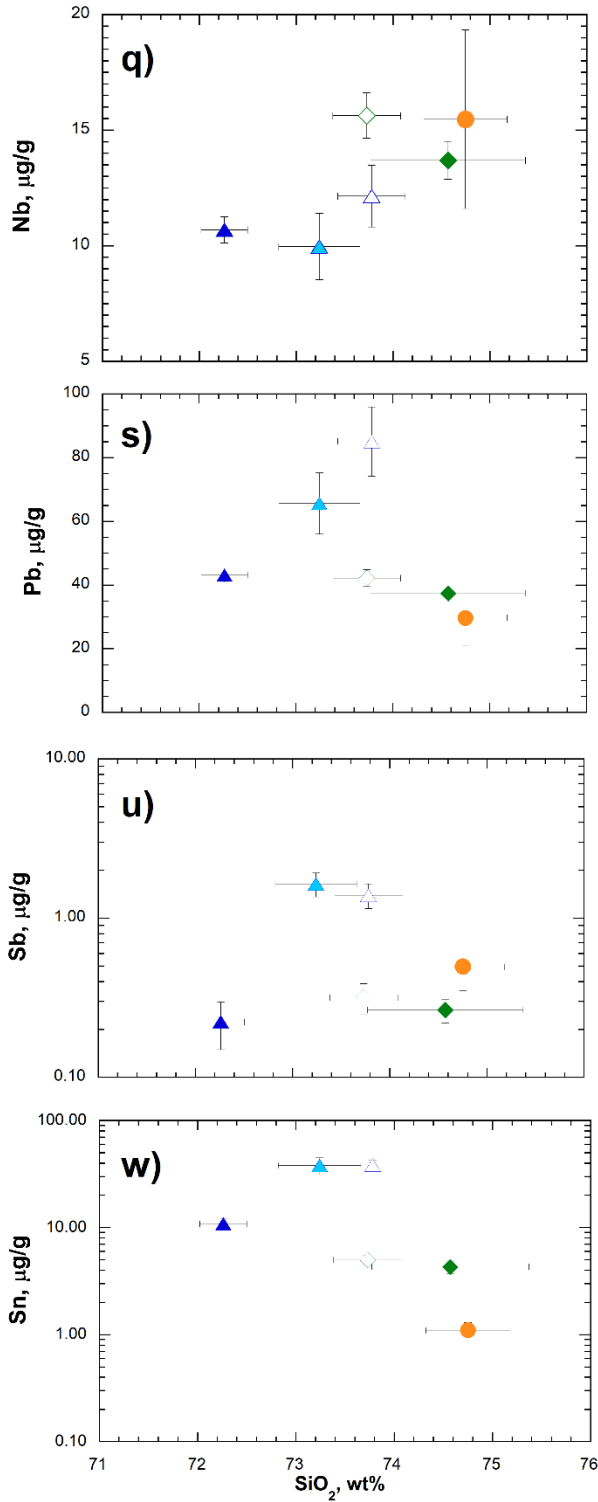
1623

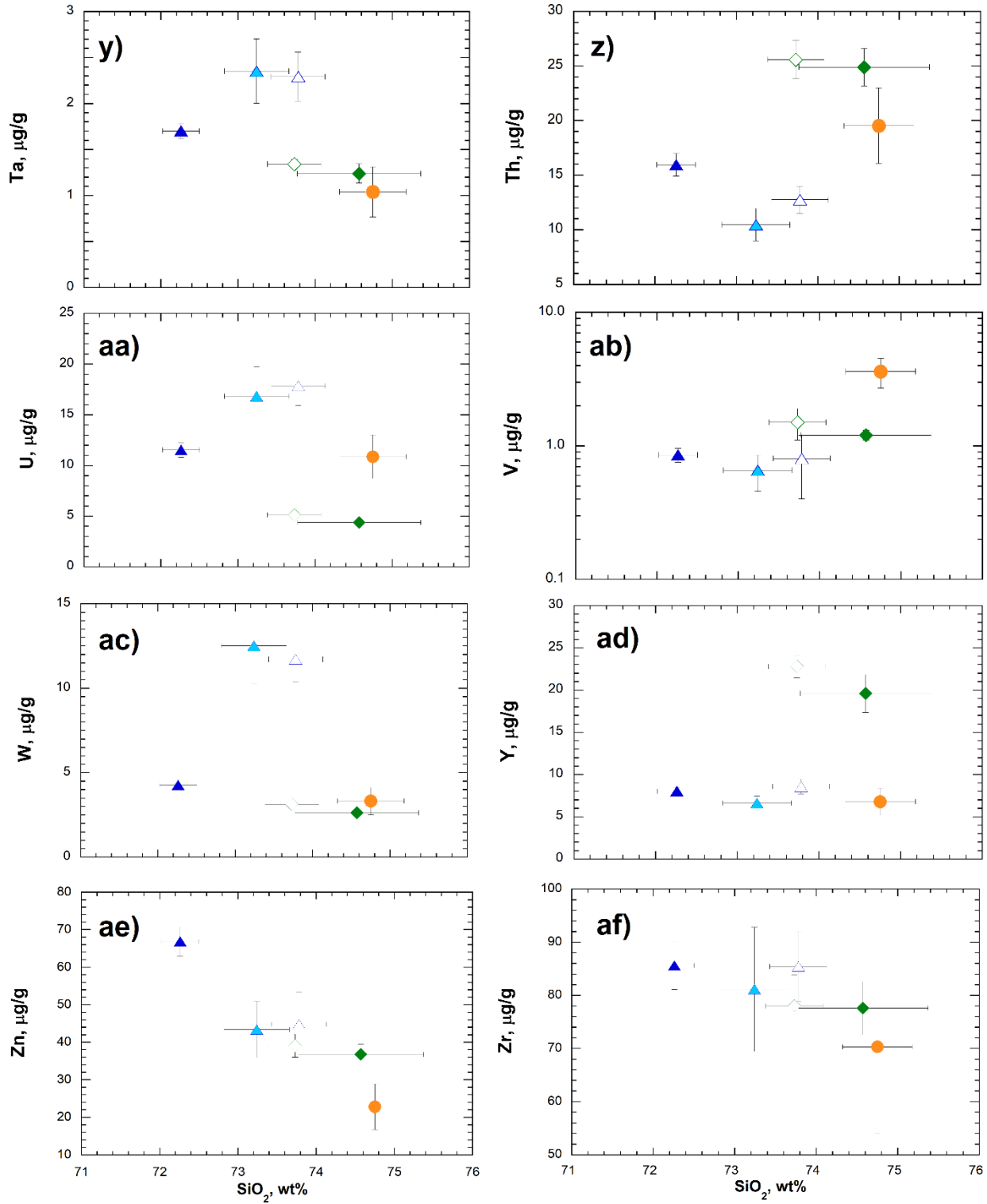


1625

1626





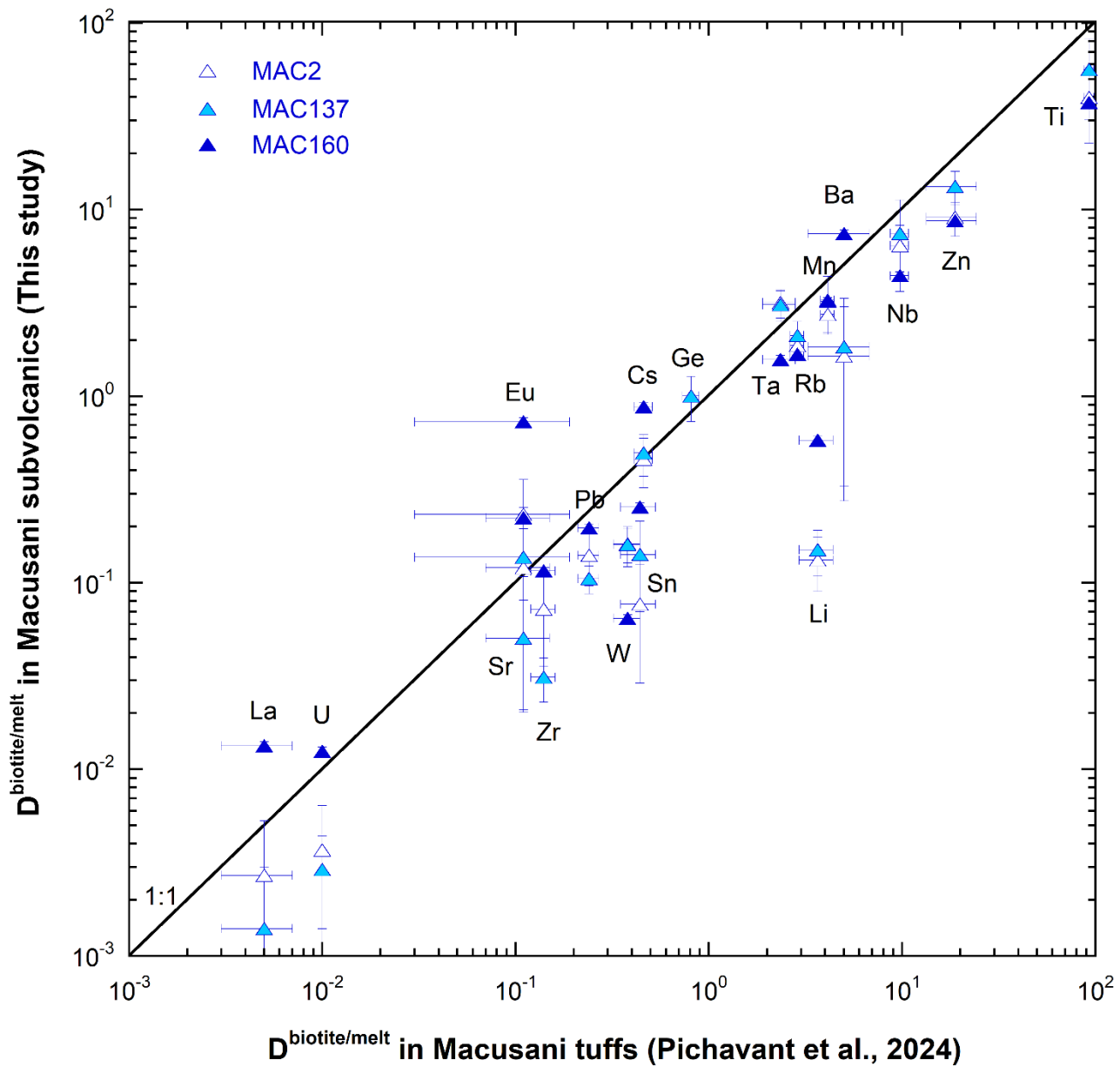


1629

1630

Supplementary Figure S6. Glass trace element composition. Symbols from Fig. 8.

1631



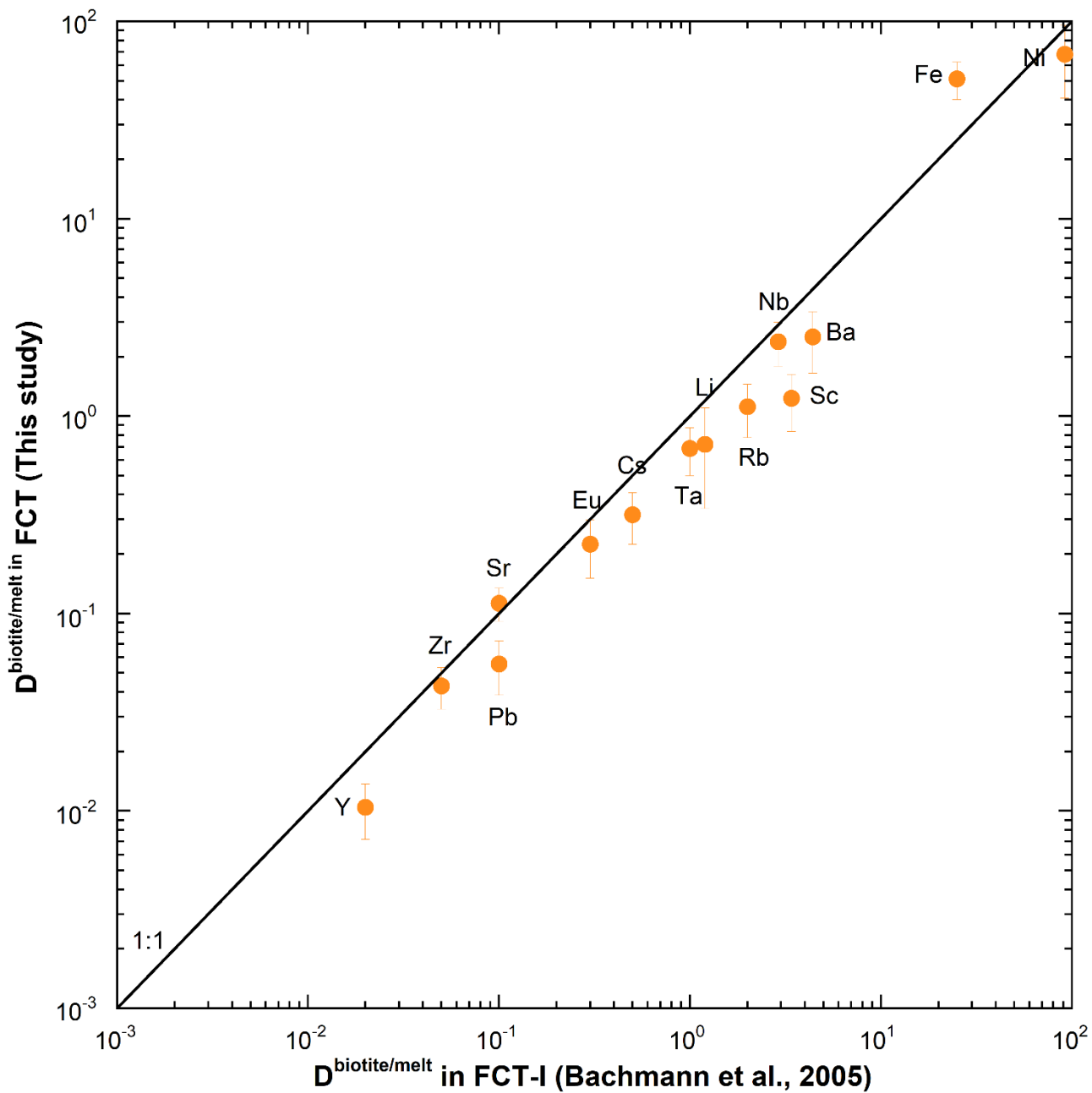
1632

1633 **Supplementary Figure S7.** Comparison of trace element D values obtained from Macusani tuffs
 1634 (Pichavant et al., 2024) and subvolcanics (MAC2, MAC137, MAC160) from this study.

1635

1636

1637

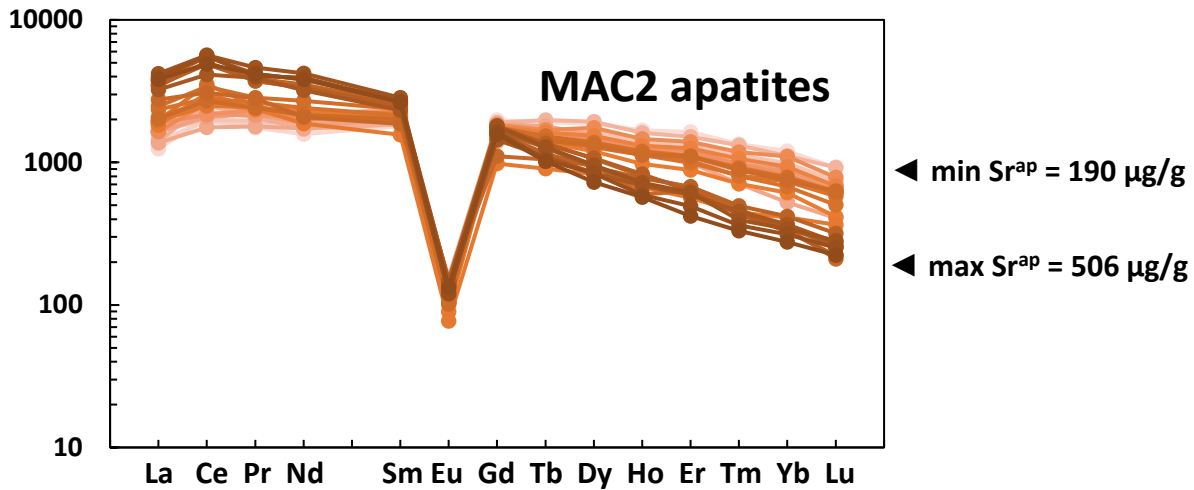


1638

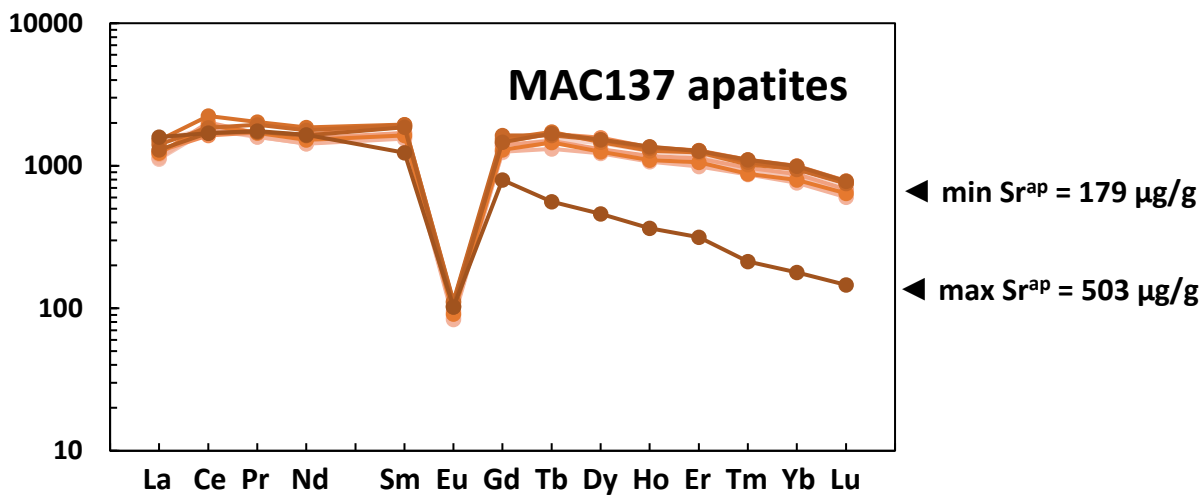
1639 **Supplementary Figure S8.** Comparison of trace element D values in the Fish Canyon tuff by
 1640 Bachmann et al. (2005) and this study.

1641

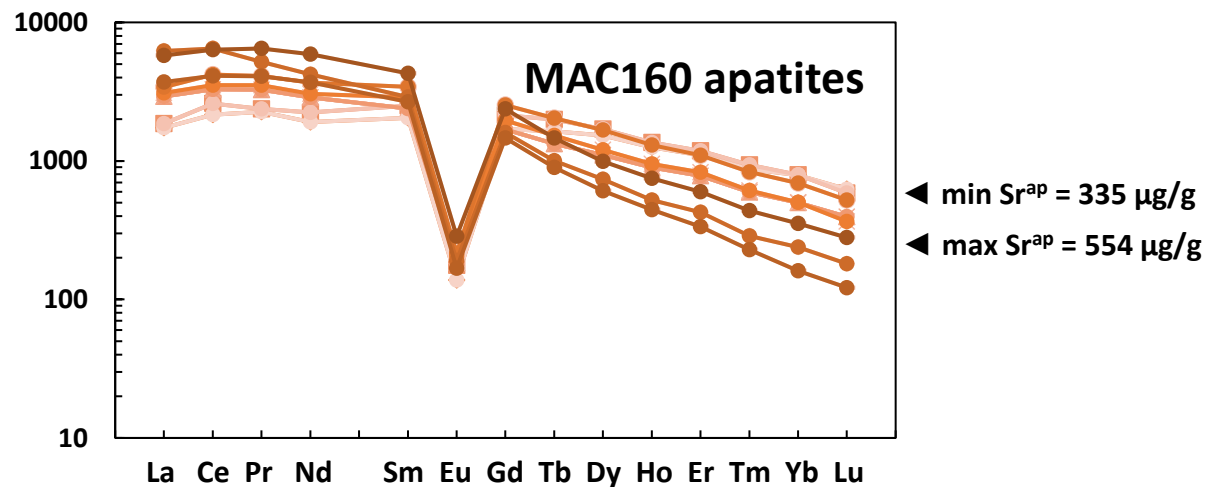
1642



1643



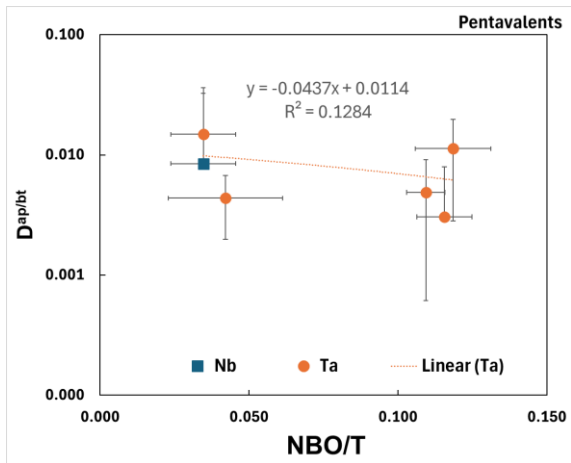
1644



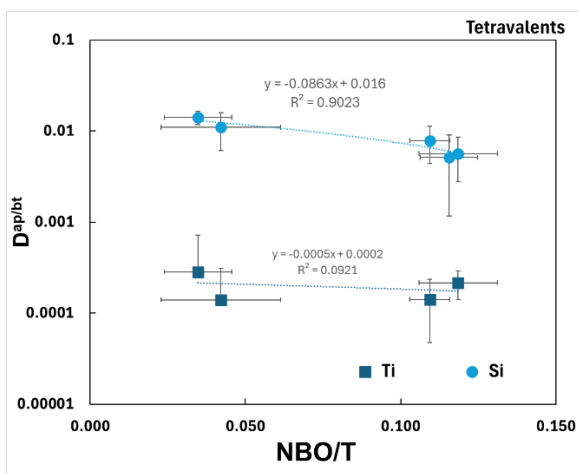
1645 **Supplementary Figure S9.** Chondrite-normalized REE abundance in Macusani apatites. Tone of the
 1646 graph corresponds with the apatite Sr (Sr^{ap}) content, darker colour denoting higher Sr abundance. In
 1647 all samples, the La/Lu and La/Sm ratios are observed in the Sr-richer apatites.

1648

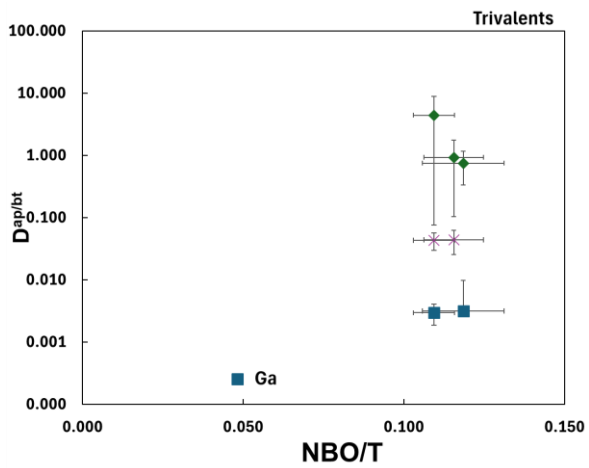
1649



1650



1651



1652 **Supplementary Figure S10.** Homovalent element $D^{ap/bt}$ as a function of melt polymerization
1653 (NBO/T).

1654

1655

1656 **Supplementary Table S1.**

1657

1658

1659 **Supplementary Table S2.** Results of the least square fits.
 1660

Mineral	Valence	Coord.	Sample	D ₀	1 σ	r ₀ , nm	1 σ	E, MPa	1 σ	R ²	χ ²
Apatite	+1	VIII-	MAC2	0.050	-	0.115	-	22	-	0.988	0.0000
			MAC160	0.044	-	0.120	-	30	-	1.000	0.0000
			TT7	0.024	-	0.120	-	30	-	0.999	0.0000
	+2	VIII-	FCT	102.7	0.859	0.112	0.000	289	11	1.000	3.5
			MAC2	95.6	2.832	0.111	0.001	250	22	0.996	32.6
			MAC137	128.8	3.291	0.113	0.001	303	26	0.999	8.8
			MAC160	82.7	1.174	0.111	0.000	251	12	0.999	6.2
			TT7	63.5	0.562	0.112	0.000	253	9	1.000	1.6
	+3	VIII-	FCT	121.7	5.660	0.108	0.000	270	34	0.912	881.6
			MAC2	158.9	7.266	0.106	0.000	311	39	0.904	1517.0
			MAC137	107.0	5.839	0.106	0.000	349	49	0.886	945.9
			MAC160	176.5	6.901	0.106	0.000	282	31	0.920	1416.5
			TT7	103.0	5.261	0.107	0.000	318	40	0.910	706.9
	+4	VIII-	FCT	2.726	-	0.107	-	225	-	1.000	0.0001
			MAC2	1.001	-	0.106	-	213	-	1.000	0.0000
MAC137			1.199	-	0.109	-	162	-	0.999	0.0010	
MAC160			6.551	-	0.108	-	276	-	1.000	0.0001	
TT7			1.624	-	0.108	-	185	-	1.000	0.0007	
Biotite	+1	XII-	FCT	1.607	0.220	0.164	0.003	55	21	0.967	0.0506
			MAC2	1.931	0.042	0.168	0.001	48	4	0.999	0.0029
			MAC137	2.117	0.092	0.170	0.001	55	9	0.996	0.0116
			MAC160	1.827	0.154	0.170	0.002	31	8	0.977	0.0396
			TT7	1.581	-	0.167	-	44	-	1.000	0.0000
			TT7	1.838	0.049	0.168	0.001	41	4	0.998	0.0040
	+2	VI-	FCT	447.3	61.900	0.068	0.001	738	162	1.000	21.5
			MAC2	441.0	342.170	0.068	0.005	1017	879	0.998	78.8
			MAC137	211.0	166.090	0.065	0.007	479	370	0.998	15.7
			MAC160	298.1	236.350	0.066	0.006	694	557	0.998	32.7
			TT7	165.3	19.948	0.070	0.001	1008	349	0.998	21.8
			TT	192.7	18.529	0.070	0.001	1151	329	0.999	19.5
	+3	IV-	FCT	5.384	-	0.053	-	463	-	1.000	0.0000
			TT7	5.753	-	0.054	-	421	-	1.000	0.0000
	+3	VI-	FCT	2.752	32.080	0.066	0.090	378	2369	1.000	0.0001
			MAC2	5.337	0.136	0.070	0.000	599	21	0.999	0.0067
			MAC137	10.425	0.081	0.071	0.000	675	7	1.000	0.0020
			MAC160	12.962	0.099	0.072	0.000	489	8	1.000	0.0034
			TT	4.122	23.120	0.067	0.043	397	1238	1.000	0.0001
			TT7	4.635	23.256	0.067	0.039	421	1239	1.000	0.0001
	+4	IV-	FCT	0.757	-	0.037	-	256	-	1.000	0.0000
			MAC137	1.003	0.006	0.038	0.000	336	7	1.000	0.0000
			MAC160	0.755	-	0.039	-	196	-	0.998	0.0001
			TT	0.688	-	0.037	-	209	-	1.000	0.0000
TT7			0.771	0.016	0.038	0.000	244	13	0.999	0.0003	

1661

1662 **Supplementary Material 1 - Sample descriptions**

1663 **Macusani subvolcanic suite, Puno, SE Peru**

1664 *General geology*

1665 The strongly peraluminous (ACNK>1.1) Macusani subvolcanics, stratigraphically assigned to
1666 the Crucero intrusive supersuite, are exposed in the Picotani, Quenamari, and Cayconi mesetas
1667 (plateaus) of the Central Andean Inner Arc of southeastern Peru. Crucero supersuite is comprised of
1668 two temporally and geochemically distinct assemblages – Picotani and Quenamari groups. Picotani
1669 intrusive suite (24.5-23.2 Ma) consists of monzogranitic hypabyssal rock bodies, temporally
1670 associated with a bimodal volcanic sequence of the Picotani group (Sandeman et al., 1997). Two
1671 bodies containing vitreous matrix – Revancha dyke and Cerro Esquinani stock – are analyzed in this
1672 study.

1673 Revancha dike is a ≤ 5 m wide and >400 m long cordierite-, biotite-bearing monzogranite
1674 body, located in the south of the Quenamari plateau, in the vicinity of the significantly larger (>20
1675 km^2) Ninahuisa stock. The bulk composition of the Revancha dike is rhyodacitic (67-68 wt.% SiO_2 , 4-5
1676 wt.% K_2O , 3 wt.% Na_2O) and peraluminous ($A/\text{CNK} = 1.1-1.2$). It intrudes a country rock of similar
1677 mineral and chemical composition (Sandeman et al., 1997). The dike is interpreted as a pristine,
1678 hypabyssal analogue of the S-type monzogranites found in the Lachlan Fold belt of SE Australia
1679 (Sandeman & Clark, 2003). Dike emplacement temperatures are in the range of 634-693°C estimated
1680 from two-feldspar thermometry (Fuhrman & Lindsley, 1988). The oxidation state of the Revancha
1681 magma is considered to be low due to the occurrence of near-stoichiometric FeTiO_3 compositions of
1682 unaltered ilmenite (Sandeman & Clark, 2003). This is supported by Ce-in-zircon oxybarometry (Smythe
1683 & Brenan, 2016) measured for the samples from this study which yielded a ΔFMQ of $-2.9 (\pm 1)$.

1684 The age of the Revancha dike has been determined using biotite $^{40}\text{Ar}/^{39}\text{Ar}$ spectra, yielding
1685 integrated ages of 24.07 ± 0.09 Ma (Sandeman et al., 1997) and 24.18 ± 0.72 Ma (Clark et al., 1990).

1686 The samples of the Revancha dyke (MAC2 and MAC137) were obtained from the collection
1687 of Dr. Hamish Sandeman (Newfoundland Geological Survey) and have been previously analyzed by
1688 Sandeman et al. (1997) and Sandeman & Clark (2003).

1689 Cerro Esquinani stock is exposed in ca. 1.2 km² area near the southern edge of the Picotani
1690 Meseta. It consists of vitreous biotite monzogranite, which intruded biotite-bearing rhyodacitic tuff
1691 of the Cerro Huancahuancane formation. Compared to the Revancha dyke, the stock is similarly
1692 peraluminous (A/CNK=1.1-1.3), more potassic (5-8 wt.%) and less sodic (1.6-2.9 wt.%) (Sandeman et
1693 al., 1997). Biotite of the stock yield a total fusion date of 24.84±0.06 Ma, which overlaps with the
1694 recorded dates of the Cerro Huancahuancane rhyodacite flow, which suggests a genetic link
1695 between the two formations (Sandeman et al., 1997). Temperature, pressure, and fO_2 for this
1696 intrusive body have not been previously established.

1697 The sample of Cerro Esquinani stock (MAC160) was received from Dr. John Hanchar
1698 ((Memorial University of Newfoundland). It has been previously analyzed by Sandeman et al. (1997).

1699 *Sample descriptions*

1700 *Revancha dyke (MAC2 and MAC137)*

1701 Revancha monzogranite contains phenocrysts of plagioclase, sanidine, biotite, and cordierite
1702 with accessory sillimanite, apatite, zircon, monazite, and ilmenite set in a holohyaline matrix. The
1703 dike exhibits a glass rich (up to 74 vol%) margin and a crystal-rich (up to 50 vol%) porphyritic
1704 interior, separated by a flow-banded facies with an intermediate glass content (63-68 vol%). The
1705 dike does not contain any macroscopic evidence of weathering or hydrothermal alteration
1706 (Sandeman & Clark, 2003). Sample MAC137 (Figure X) is a biotite microphenocryst-rich sample of the
1707 glassy, flow-banded Revancha dike facies. Older, larger biotite phenocrysts exhibit both resorption
1708 features and sieved textures. Darker rims of the larger phenocrysts represent reverse zoning with
1709 progressive enrichment in Mg towards the crystal edges. Iron numbers (Fe#) of the analyses bt02
1710 (rim) and bt03 (interior, Figure 4a) are 0.48 and 0.51 respectively. In contrast, microphenocrysts are
1711 euhedral with no observable zoning. MAC2 (Figure X) is a sample of the crystal-poor facies of the
1712 Revancha dike glassy chill margin. Similarly to MAC137, the larger biotite phenocrysts exhibit
1713 reverse and oscillatory zoning and sieve texture. Biotite microphenocrysts are euhedral with no
1714 observable zoning.

1715 *Cerro Esquinani stock (MAC160)*

1716 Cerro Esquinani monzogranite contains predominantly plagioclase and biotite together with
1717 rare sanidine and quartz phenocrysts and trace amounts of sillimanite, zircon, apatite, monazite,
1718 ilmenite in a vitreous matrix (Sandeman et al., 1997). In the MAC160 handsample, compared to the
1719 Revancha dyke samples, flow banding and bent biotite flakes are rare. Large and medium-sized
1720 biotite crystals (>200 μm) exhibit resorption features, which are more present than in Revancha
1721 dyke, apart from the resorption features, the crystals are euhedral. MAC160 contains very few fine
1722 biotite flakes (<100 μm) are significantly less abundant. Biotite zoning is present only in the largest
1723 crystals, which are normally zoned. Apatite in MAC160 is less abundant and smaller in size than in
1724 Revancha samples. Most of apatite crystals are euhedral, few crystals are rounded presumably by
1725 dissolution. The matrix glass is scattered with <5 μm Fe-Ti oxide microlites, which are not present in
1726 Revancha samples.

1727

1728 **Tuk-Tuk lava dome, Toba, Sumatra, Indonesia**

1729 *General geology*

1730 The Toba samples (TT and TT7) are sourced from the Tuk-Tuk lava domes, located along the
1731 NE shore of Samosir Island, at the centre of the Toba caldera (Sumatra; Chesner et al., 2020). The
1732 samples were obtained from the personal collection of Dr. Craig Chesner (Eastern Illinois University).
1733 The lava domes represent the youngest volcanic activity associated with the Toba caldera, having
1734 extruded following the climactic eruption that produced the underlying youngest Toba tuff (YTT).
1735 Chesner et al. (2020) report weighted mean $^{39}\text{Ar}/^{40}\text{Ar}$ ages from Tuk-Tuk dome sanidine phenocrysts
1736 of 74.1 to 75.8 Ka, in agreement with the range of 74.5 to 75.2 Ka for sanidine from the YTT. The
1737 Tuk-Tuk dome samples are considered to be virtually identical to the YTT in terms of phenocryst
1738 mineralogy, textures and geochemistry (Chesner et al., 2020). For the associated upper YTT
1739 members, Chesner (1998) reported crystallization temperatures of 713-761°C and oxygen fugacity
1740 values of FMQ +1.0 to +1.4 based on Fe-Ti oxide oxybarometry.

1741 *Sample description*

1742 The Tuk-Tuk lave dome samples are light gray-to-white, vesicular (6-7 vol%), comprised of
1743 glass (47-72 vol%), quartz (6-12 vol%), sanidine (1-12 vol%), plagioclase (9-34 vol%), biotite (1-4
1744 vol%), and hornblende (≤ 2 vol%) with trace amounts of zircon, allanite, magnetite, ilmenite,
1745 orthopyroxene, and apatite (Chesner et al., 2020). Biotite in both samples is euhedral and kinked
1746 crystals are common. Unlike hornblende crystals, biotite does not exhibit observable compositional
1747 zoning and resorption features in biotite are rare. Biotite-hosted inclusions of zircon, monazite,
1748 magnetite, and feldspar are common in both samples, melt inclusions are rare. Biotite in TT7
1749 contains ubiquitous inclusions of acicular apatite. Sample TT, however, is completely devoid of
1750 apatite.

1751

1752 **Fish Canyon tuff, Colorado, US**

1753 *General geology*

1754 The Fish Canyon Tuff (FCT) is one of the 17 major (>100 km³) ash-flow sheets of the San Juan
1755 volcanic field located in the southern part of Colorado (USA; Lipman et al., 1970). Despite its
1756 enormous volume (~ 5000 km³), the FCT is remarkably uniform in composition (e.g., $\sim 68.0 \pm 0.5$ wt%
1757 SiO₂). The entire tuff sheet forms a single cooling unit with a common, <10 m thick basal vitrophyre
1758 layer. The sample analysed in this study was provided by Dr. Ray Donelick collected at the classic site
1759 (Gleadow et al., 2015) of the Fun Valley Ranch on Highway 160, Colorado (USA). Recent age
1760 determinations on FCT phenocrysts yield values of $28.37 (\pm 0.05)$ Ma by the ²³⁸U/²⁰⁶Pb method on
1761 zircon and $28.04 (\pm 0.18)$ by the ⁴⁰Ar/³⁹Ar method on sanidine, with coexisting biotite, hornblende
1762 and plagioclase yielding 0.2 to 0.3 Ma older ages (Bachmann et al., 2007). Johnson & Rutherford
1763 (1989) used the composition of coexisting Fe-Ti oxides to determine a magma crystallization
1764 temperature of $760 (\pm 30)$ °C and oxygen fugacity of FMQ+3.0. These workers also determined the
1765 pressure in the Fish Canyon magma chamber to be $240 (\pm 50)$ MPa (equivalent to depth of 7.9 km)
1766 using Al-in-hornblende geobarometry. Melt inclusions trapped in quartz and hornblende
1767 phenocrysts from the FCT record compositions identical to matrix glass (Johnson & Rutherford, 1989),
1768 suggesting little compositional evolution of the FCT magma between phenocryst growth and
1769 eruption.

1770

Sample description

1771

1772

1773

1774

1775

1776

1777

1778

1779

1780

Mascota minette, Jalisco, W Mexico

1781

General geology

1782

1783

1784

1785

1786

1787

1788

1789

1790

1791

1792

1793

1794

Sample description

1795

1796

Samples contain phenocrysts of plagioclase, sanidine, biotite, hornblende, quartz, magnetite, titanite, and ilmenite in a matrix of microcrysts, phenocryst fragments, and glass. The relative proportions within the phenocryst assemblage are close to constant (~55% plagioclase, ~15% alkali feldspar, 5% quartz, 10% biotite, 10% hornblende, 5% trace minerals) and their modal abundance in the tuff depends on the crystallinity of the rock (35-50%; Whitney and Stormer, 1985). Matrix glass commonly features fiamme textures, but in numerous pockets the glass is massive and fresh. Biotite is typically fresh, euhedral, often kinked, and compositionally uniform (Figure 4e), often contains inclusions of apatite, feldspars and hornblende.

Mascota volcanic field is located in the Jalisco Block of western Mexico, where the Rivera Plate (a separated fragment of the Farallon plate) subducts beneath the North American Plate along the Middle America trench. The field spans an area of ~2000 km² and contains ~87 small cones and lava flows of minette, absarokite, basic hornblende lamprophyre, basaltic andesite, and andesite (R. A. Lange & Carmichael, 1990). Mascota minettes represent the youngest volcanism in the region, their ⁴⁰K-⁴⁰Ar ages on biotite are between 0.489±0.08 and 0.061±0.192 Ma (Carmichael et al., 1996). Phenocryst assemblage of augite minettes (sampled in this study) record a crystallization temperature of 1080-1100°C, determined by experiments of phlogopite and augite saturation in a related augite minette. Equilibration pressure of augite and olivine minettes of Mascota volcanic field is estimated to be between 5 and 15±4kbar, based on TiO₂ and BaO partitioning between phlogopite and matrix (Righter & Carmichael, 1996). Oxidation state of augite minettes (FMQ+4.3; Carmichael et al., 1996) was resolved using Fe₂O₃/FeO ratio in matrix (Kress & Carmichael, 1991).

Sample has been provided by Smithsonian Institution (number NMNH 117626-21) and has been previously analysed by (Carmichael et al., 1996) as M.18.

1797 The sample consists of phlogopite (~5 vol%), augite (~13 vol%) phenocrysts and
1798 microphenocrysts in a very fine-grained groundmass (~79 vol%) of phlogopite and sanidine. Apatite,
1799 zircon, magnetite, and ilmenite are present in trace amounts both in the phenocryst assemblage
1800 and groundmass. Phlogopite phenocrysts occur as reddish brown tabular, <1 mm large flakes.
1801 Inclusions in biotite are rare, usually ilmenite and zircon. Apatites are euhedral, colourless, up to 60
1802 microns large prismatic to acicular crystals.

1803

1804 **Umiakovik pluton, Labrador, Canada**

1805 *General geology*

1806 Umiakovik pluton is represented by sample EC 87-119, previously analyzed by (Emslie & Stirling,
1807 1993).

1808 Umiakovik pluton, located in northern Labrador (Canada) belongs to the Nain Plutonic suite, an
1809 example of anorthosite-charnokite-mangerite-granite (ACMG) suites of Mesoproterozoic. The Nain
1810 plutonic suite intrudes the Torngat orogen region between the Nain and Rae cratons of the
1811 Canadian Shield. Within the suite, two spatially and temporarily distinct intrusive sequences (1363-
1812 1319 Ma in NW and 1319-1289 Ma in SE) are recognized. Emplacement of the Umiakovik pluton is
1813 the final intrusive episode of the first sequence.

1814 Umiakovik composite pluton consists of biotite and biotite-hornblende granite, fayalite-pyroxene
1815 quartz monzonite and granite facies, and rare monzodiorite occurrences adjacent to the contact
1816 with anorthosite. The boundaries between the fayalite-, pyroxene-, and hornblende-bearing facies
1817 are gradational, however the hornblende-biotite and biotite granites (sampled in this study) intrude
1818 the fa- and py-bearing facies as dykes and sheets. EC 87-119 sample, which represents the latter bt-
1819 hbl-granite, produced zircon $^{207}\text{Pb}/^{206}\text{Pb}$ age of $1316 \pm 2/-3$ Ma in agreement with K-Ar ages for biotite
1820 (1302 ± 19 Ma) and hornblende (1322 ± 18 Ma). Corresponding to the field relationships, these ages
1821 are marginally younger than the 1319 ± 2 Ma zircon $^{207}\text{Pb}/^{206}\text{Pb}$ age of the of the fayalite quartz
1822 monzodiorite (Emslie & Loveridge, 1992). Emplacement pressure estimate, based on Al-in-hornblende
1823 geobarometer (Johnson & Rutherford, 1989), is 3.7 ± 0.5 kbar. This corresponds within error to the

1824 garnet-cordierite and hypersthene-olivine-quartz equilibria (Hensen & Green, 1972; 1973) in the
1825 mineral assemblage in the metamorphic aureole of Nain plutonic suite, which suggests 3.5 ± 1 kbar
1826 (Berg, 1977; 1979).

1827 Late-stage crystallization temperature $750-800^{\circ}$ C is based on equilibration of pyroxene- and olivine-
1828 bearing facies and presence of inverted pigeonite in the monzodiorite facies (Emslie & Stirling, 1993).
1829 Given that the sampled facies does not contain olivine and pyroxene, a more accurate and
1830 representative temperature estimate (e.g., Henry et al., 2005) is necessary. The oxidation state of
1831 Umiakovik pluton has been initially estimated by the intersection of isopleths defined by the
1832 hematite content in ilmenite and the Fe^{3+}/Fe^{2+} ratio of biotite, ranging between FMQ-1 and FMQ-4
1833 (Emslie & Stirling, 1993). Subsequent Ce-in-zircon oxybarometry narrowed the fO_2 range to FMQ-
1834 2.4 ± 0.7 (Smythe & Brenan, 2016).

1835 *Sample description*

1836 Sample EC 87-119 is a representative sample of biotite-hornblende granite. It consists of alkali
1837 feldspar (43 vol.%), quartz (25 vol.%), plagioclase (20 vol.%), biotite (7 vol.%), hornblende (5 vol.%)
1838 and trace amounts of apatite, zircon, ilmenite, and fluorite (Emslie & Loveridge, 1992). Biotite is dark
1839 brown, often bent, subhedral, up to 1-2 mm large crystals without noticeable zoning in reflected
1840 light or SEM. Biotite occasionally contains up to 20 microns large apatite and zircon inclusions.
1841 Apatite crystals are typically up to 400 microns large prismatic, euhedral, pale green, transparent
1842 crystals. In SEM, approximately 30% of apatite crystals exhibit a distinct darker, rounded core with
1843 >20 micron thick, bright rim. Inclusions in apatite are rare, usually few microns large zircons.